Millimetre-waves Antenna Arrays for 5G and Wireless Power Transfer

BILAL TARIQ MALIK

Submitted in accordance with the requirements for the degree

of

Doctor of Philosophy

The University of Leeds

School of Electronic and Electrical Engineering

September, 2019

Declaration

The candidate confirms that the work submitted is his own, except where work which has formed part of jointly-authored publications has been included. The contribution of the candidate and the other authors to this work has been explicitly indicated below. The candidate confirms that appropriate credit has been given within the thesis where reference has been made to the work of others.

The work in **Chapter 2** has appeared in the following publication.

1. Bilal T Malik, Viktor Doychinov, Syed Ali R Zaidi, Nutapong Somjit, Ian D Robertson and Charles W Turner. *“Higher-order mode substrate integrated waveguide cavity excitation for microstrip patch antenna arrays at 30-GHz”,* Journal of Physics; Communications, 2018.

The work in **Chapter 3** has appeared in the following publication.

2. Bilal T Malik, Viktor Doychinov, Syed Ali R Zaidi, Ian D Robertson and Nutapong Somjit, “*Antenna gain enhancement by using low-Infill 3D-printed dielectric lens antennas”,* IEEE Access, 2019.

The work in **Chapter 4** has appeared in the following publications.

3. Bilal Malik, Viktor Doychinov and Ian Robertson, *"Compact broadband electronically controllable SIW phase shifter for 5G phased array antennas"*, European Conference on Antennas & Propagation (EuCAP), 2018.

4. Bilal T Malik, Nuttapong Duangrit, Viktor Doychinov, Nuttapong Somjit and Ian D. Robertson*, “24-40 GHz low-cost & low-loss 3D printed hollow integrated waveguide”*, to be submitted in IEEE Access.

The work in **Chapter 5** has appeared in the following publications.

5. Bilal T Malik, Viktor Doychinov, Ali Hayajneh Syed Ali R Zaidi, Ian D Robertson and Nutapong Somjit, "*24 GHz wireless power transfer system for Internet of Things sensor nodes",* submitted in IEEE Access, 2019.

6. Bilal T Malik, Viktor Doychinov, Syed Ali R Zaidi, Ian D Robertson, Nutapong Somjit and Robert Richardson, "*Flexible rectennas for wireless power transfer to wearable sensors at 24 GHz",* Research, Invention, and Innovation Congress (RI2C), 2019.

7. Viktor Doychinov, B. Kaddouh, G. Mills, Bilal Malik, N. Somjit, Ian Robertson, *"Wireless power transfer for gas pipe inspection robots"*, The UK-RAS Network Conference on Robotics and Autonomous Systems, 2017.

This is to assert that the candidate has contributed solely to the technical part and writing of the papers (1)-(6) under the guidance of his co-authors.

In (7) jointly-authored publication, the contribution of Bilal Malik was the design, simulation, fabrication and measurements of tapered slot antenna used for wireless power transfer to pipe robot prototype.

Acknowledgements

First and foremost, I would like to thank Almighty Allah for his countless blessings upon me.

I would like to express my sincere thanks to University of Leeds for their financial support during my PhD studies. I am extremely thankful and grateful to my supervisor Prof. Ian Robertson for his kind guidance and support throughout my PhD. I wish to extend my thanks to Dr. Ali Zaidi and Dr. Nutapong Somjit for their support, guidance and fruitful discussions.

I am also thankful to Dr. Doychinov for his support and encouragement. He always spared his busy time generously for me whenever I needed him for discussion and his kind advice.

I would like to express my love and gratefulness to my loving parents, my wife Anum and my children Ariz & Hiba for their love, unconditional support and patience during my PhD.

At last but not least, I am thankful to the Engineering and Physical Sciences Research Council, UK for the financial support and the technical staff at the University of Leeds Electronics Workshop for fabricating the hardware presented in this thesis.

Abstract

Millimetre-wave (mmW) technology is one of the promising candidate for the deployment of next generation wireless communications. Key benefits of mmW is the availability of large continuous bandwidth and miniaturization of microwave components due to short wavelength. Despite of aforementioned benefits of mmW technology there are also some challenges such as the high path loss, severe attenuation due to atmospheric absorption and signal blockage. One solution to mitigate the path loss and signal blockage at mmW frequencies is by using high gain directional antenna arrays with beam steering capabilities for point-to-point communication. The goal of this thesis is to develop new modelling techniques and fabrication methods for the design and implementation of efficient, cost-effective, high gain, easy to design and manufacture mmW antenna arrays and other microwave components (integrated waveguides, phase shifters and rectifiers) for 5G wireless communications and far field wireless power transfer (WPT) applications.

A simple yet efficient excitation technique for microstrip patch antenna (MPA) arrays is presented based on higher order mode substrate integrated waveguide (SIW). The proposed approach also enhances the gain of antenna array due to less radiation and transmission losses. In addition to the above, a low cost and easy to manufacture integrated lens antenna (ILA) based on low infill density 3D printing technology is presented for applications where higher gain is required while retaining the small foot

print. Proposed antenna arrays are well suited for millimetre-waves 5G communications and far field wireless power transfer applications in Internet-of-things (IoT) sensor nodes.

With the gain enhancement of antennas the beam-width of antenna reduce as well as the coverage will also limited. Therefore, to serve the multi-users we need phased antenna arrays for point-to-point communications. The phase shifter is the key component to enable beam steering capabilities. A novel approach to design a compact broadband reconfigurable SIW phase-shifter for phased array antennas in 5G wireless communications is presented and verified by experimental analogue. In addition to SIW phase shifter, to improve the insertion loss in SIW structure due to substrate material a novel design and fabrication technique for low loss hollow integrated waveguide (HIW) based on low cost 3D printing technology is also presented. The proposed components are compact, broadband, low cost and easy to fabricate and integrate with other planar circuits.

In regard to mmW wireless power transfer applications, several compact and efficient rectennas has been designed specifically for WPT to IoT sensor nodes for structural health monitoring and inspection applications. Conformal antenna arrays and flexible rectifiers for wearable applications have also been presented. To address the issue of finite battery life of IoT sensor nodes a complete mmW far-field wireless power transfer system for WPT to IoT sensor nodes for backscattering communications is proposed and demonstrated.

Table of Contents

List of Tables

List of Figures

List of Abbreviations

3D	Three Dimensional
5G	Fifth Generation
ADS	Advance Design System
DC	Direct Current
EM	Electromagnetic
FDM	Fused Deposition Modelling
HFSS	High Frequency Structure Simulator
HIW	Hollow Integrated Waveguide
ILA	Integrated Lens Antenna
IoT	Internet of Things
ISM	Industrial Scientific and Medical
mmW	Millimetre-Waves
MPA	Microstrip Patch Antenna
PLA	Polylactic Acid
RF	Radio Frequency
SIW	Substrate Integrated Waveguide
SWIPT	Simultaneous Wireless Information & Power Transfer
WPT	Wireless Power Transfer

Chapter 1. Introduction

1.1. Motivation

Fifth generation (5G) communications is the future reality of reliable wireless communication systems with high data rate transmission and huge network capacity to support millions of users and Internet-of-Things (IoT) devices [1, 2]. Millimetre-wave (mmW) technology has been considered one of the most attractive candidates for the implementation and deployment of 5G mobile communications [3]. However, there are also some issues and challenges involved in the design, implementation and utilisation of mmW technology such as signal blockage, severe path loss and signal attenuation due to atmospheric absorption [2]. Furthermore, cost and complexity of hardware deployment is another limiting factor for implementation of mmW for 5G communications [4].

Despite all these, there are also some encouraging factors that make mmW communications one of the most promising solutions for 5G communications, such as wide continuous bandwidth available for high data rate transmission, security due to low spatial co-channel interference and reduced size of antenna arrays due to the decreased wavelength [2, 3]. The last feature of mmW can also be beneficial for mmW wireless power transmission due to a reduction in the physical space occupied by the rectennas, i.e. a combination of an antenna and a rectifier, while retaining the same output power density. Furthermore, the beam directivity can also be enhanced by using mmW which improves the performance of far-field

WPT [5]. This has the potential to power the vast number of low-power wireless devices connected to the future 5G networks such as IoT smart nodes. Path loss and signal blockage at mmW frequencies can be compensated by using high gain and directional antenna arrays with beam steering capabilities for point-to-point communication [2, 3, 6].

Many solutions have been proposed in the literature to enhance the antenna gain [7-14]. Most common is the use of large arrays of microstrip patch antennas (MPAs) gain enhancement to mitigate the effects of increased propagation loss at mmW. Gain increases with larger number of radiating elements but the complexity as well as radiation and transmission losses in the array also increase, especially at mmW frequencies [2]. Therefore, a simple yet efficient excitation technique for MPA arrays is desirable.

Another often used method for gain enhancement is the use of dielectric lens, placed on top of an MPA or a SIW slot antenna [10]. One of the benefits of lens antennas is retaining a small footprint while providing gain enhancement. Most of the dielectric lens antennas reported in the literature have high manufacturing cost and excessive weight due to the use of expensive and dense dielectric materials, in addition to costly fabrication techniques [15, 16]. The impact of the infill pattern and infill density of 3D-printed dielectric lens on the performance of integrated lens antennas is also needs to be investigated.

Antenna gain enhancement leads to a reduction of the beam-width, thereby limiting coverage as well [9]. Therefore, to serve the multiple users we would need phased antenna arrays for point-to-point communications [6, 17].

Phased array antenna are used to steer the beam in different direction by changing the phase and amplitude of input signal [6]. In order to implement a phased array antenna, the phase shifter is the key component to enable beam steering capabilities. Design and implementation of efficient and low cost phase shifters for mmW is another important area of research. Substrate integrated Waveguide (SIW) phase shifters are easy to fabricate and integrate with antenna arrays due to the simple single-layer layout of the SIW structure and this was explored through both simulations and experimental analogue.

One of the drawbacks of SIW is the dielectric loss due to the substrate material. In order to improve the insertion loss in SIW structures multiple design and fabrication techniques for low-loss hollow integrated waveguide (HIW) have been presented. Most of the proposed fabrication techniques such as Low-temperature co-fired ceramic (LTCC), lithographic technique etc. are complex and expensive to manufacture [18, 19]. Hence a compact, low-cost, low-loss, and easy to fabricate and integrate hollow SIW is required for mmW communications.

Millimetre-wave far-field wireless power transfer (WPT) is another important topic to research in the 5G domain due to the finite battery life of IoT sensor nodes [20, 21]. There are still many challenges involved in mmW WPT that need to be addressed and investigated [22, 23]. High gain and low cost mmW antenna arrays as well as compact and efficient rectennas for mmW WPT to IoT sensor nodes for structural health monitoring and inspection applications is the main focus in this research work.

1.2. 5G Communications

Fifth generation (5G) wireless communications is the future of reliable wireless communications, with high data rate >10 GB/s (compared to 1 GB/s for 4G) and low latency <1ms (compared to 70 ms of 4G) to accommodate the ever increasing telecommunication traffic [2, 4]. Key technologies that will play an important role in 5G communications are Millimetre-waves, massive MIMO, small base stations (SBSs) and beamforming [2, 4]. Small Cell Base Stations (SBSs) with multiple and distributed antennas having high gain and directional radiation patterns, together with efficient beamforming techniques will play a fundamental role in high data rate transmission [24]. Currently allocated frequency spectrum is reaching its capacity limit, so cellular systems will have to move to higher frequency bands beyond 3 GHz and up to 100 GHz to access wider continuous channel bandwidth, increased network capacity, and to meet expected growth [3]. Therefore, the bands at millimetre-wave frequencies have been proposed for next generation wireless communications such as 24.25-29.5 GHz, 37-40 GHz [25]. Implementation of mmW 5G communication systems will be made possible with the development of new design and modelling techniques as well as fabrication methods.

1.3. Millimetre-wave (mmW) frequency spectrum

Electromagnetic (EM) waves with frequencies between 30 GHz and 300 GHz have free space wavelengths between 1 and 10 millimetres [3], giving them the name millimetre-waves. This part of the EM spectrum is underused and can be utilised for 5G applications [2, 3, 6]. Due to the rapid increase in

wireless data traffic, mmW technology is expected to become one of the most attractive candidates for 5G mobile communication to provide high data rate communication services [3].

1.3.1. Advantages and disadvantages of millimetre-wave communications

- One of the major benefits of mmW communication is the availability of large bandwidth to support extremely high data rate transmission, which is a key requirement in future 5G communications [2, 3].
- At mmW frequencies the size of a single antenna element will be very small, hence the small size of individual antennas will lead to less space occupied by the arrays in comparison to a lower frequency.
- Co-channel interference to and from other systems would be mitigated due to Line-of-Sight (LOS) propagation by using highly directional and steerable antenna arrays [2, 24].
- Large capacity of users would be possible in 5G network due to large frequency reuse factor [24].
- According to the Friis equation [26], signals in mmW band experience higher free space path loss, as well as large attenuation due to atmospheric absorption when compared to lower frequencies. Therefore, reliable communication with low Bit-Error Rate (BER) mmW communication can only be possible at short distances < 100 meter [3].
- Transmission quality of mmW communication can be negatively affected by ground obstacles, buildings, and trees. In addition, heavy

rainfall and fog conditions can also degrade the performance of millimetre wave communication [2, 3].

1.4. Future challenges in 5G communications

Many issues and challenges need to be addressed for the successful deployment of mmW 5G communications [4]. First, the free space path losses increase with the square of the frequency, so a move from sub-6GHz to around 30 GHz will lead to at least a 25-fold increase in path loss. Due to their very short wavelengths mmW signals will be adversely affected by ground obstacles, tress and buildings, necessitating line of sight (LOS) links by using beam forming and beam steering techniques for effective mobile communications [2, 3, 24]. A number of solutions have been proposed in the published literature to overcome the issue of range limitation due to high path loss and severe attenuation due to atmospheric absorption. One way to get extra range is to use high gain directional antenna arrays [2]. Phased arrays can also be used to steer the beam in a desired direction, thereby avoiding large obstacles [6, 14].

1.4.1. Beamforming for 5G

Beamforming is a technique used in phased arrays for directional signal transmission and reception. Adjustments in the phase and relative amplitude of individual array elements changes the shape and direction of radiation pattern of an array [6] as shown in Figure 1-1. The phase of input signal controls the beam direction and the amplitude excitation changes the shape and side lobe levels of radiation pattern. In some phased array

systems, switches are used to select a number of pre-defined radiation patterns [1, 14]. Beamforming is a key enabling technology for 5G communications to achieve high data transmission with low latency and LOS propagation to overcome the unfavourable propagation conditions encountered in mmW communication. The use of large antenna arrays with beamforming network at both the transmitter and receiver make this an attractive technique for 5G networks [7, 8].

A phase shifter is the most crucial part of phased array antenna for beamforming. Phase shifters are the circuits that change the phase of an input signal with minimum insertion loss, are fundamental to the operation of electronically steerable phased array antennas at microwave and millimetre-wave frequencies [27]. Phase shifters will be an integral part of 5G communication systems due to use of phased array antenna for beam steering [6, 17].

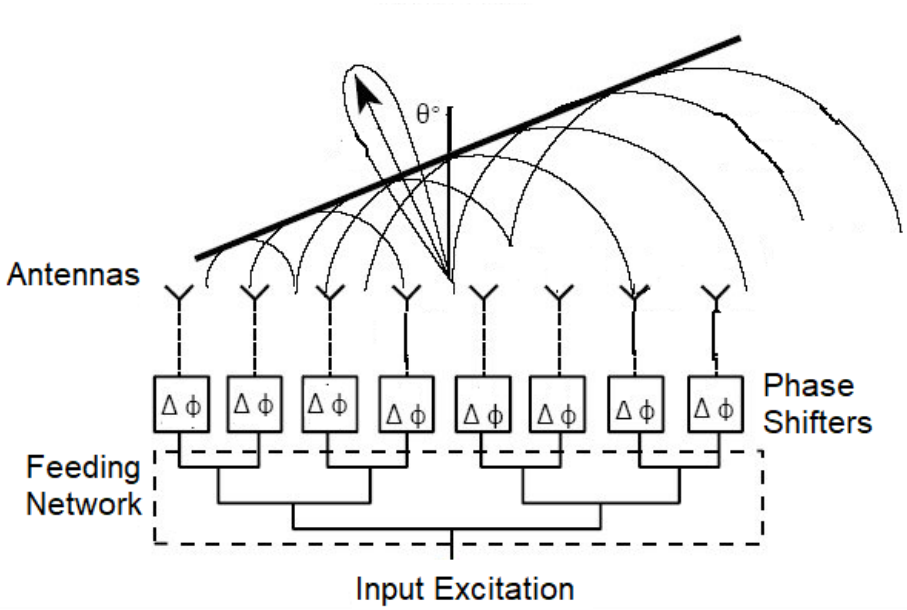

Figure 1-1 Beamforming using phased array antenna

1.5. Role of 5G communications

The concept of “smart cities” has gained a lot of attention in the last years due to possible solutions with the implementation of 5G network [28, 29]. 5G network together with the IoT sensor nodes, robotics and drones will play an important role in realization of “smart cities” [30]. Traffic, water and waste management as well as structural heath monitoring and energy harvesting are the major requirements of “smart cities” [22].

1.5.1. Robotics

5G will play a key role in the field of Robotics in the future [31]. Robots and drones can be used for many purposes in the fields of farming, health care, construction, and structural health care monitoring as summarised in Figure 1-2.

5G communication will allow robots to function more efficiently in terms of power requirements and real time data transmission [31]. One of the major issues in drones and robotics is their battery life. Battery performance can be improved by using high gain directional antenna arrays with beam steering capability, which is expected to be a fundamental element in 5G communications [2]. Due to the low latency and high data rate transmission, the robots would be able to communicate with each other in real time to complete their tasks [31].

Figure 1-2 Future applications of drones & robots in “smart cities”

1.5.2. Internet-of-Things (IoT)

The Internet of Things (IoT) is defined as a system of interconnected physical devices, vehicles, animals or people embedded with distinctive identifiers (RFIDs), software, sensors and the capability to transfer the data over a network without requiring human-to-human or human-to-computer interaction [30]. IoT technology is expected to have a lot of practical applications in many industries today, including agriculture, construction, manufacturing, medical and healthcare technology, energy and transportation. Researchers are developing a range of IoT devices for 5G applications [28].

1.5.3. Energy harvesting

IoT modules are becoming smaller day by day and one of the biggest challenges is maximising the life of their small-capacity batteries [21, 29, 32]. However, batteries present in these IoT devices have many drawbacks in terms of size, weight, cost and they need to be replaced from time to time depending on the application and wireless technology used. Therefore it may not be possible to install the IoT smart nodes in a hard-to-reach places

where battery would not be replaced or it becomes a very difficult, time consuming and costly job to replace the battery such as IoT sensor nodes on large structure for health monitoring [21, 22]. A typical lifespan of a battery-powered IoT sensor node is 90 to 120 days [33]. Hence the battery life of an IoT device is one of the challenges that needs to be addressed. One way to overcome this problem is to completely remove battery from the IoT sensor and make it self-powered and the other proposed solution to this problem is to use a small rechargeable power source in IoT smart nodes that can be topped up through mmW wireless power charging.

1.5.4. Millimetre-wave wireless power transfer

For the work presented in this thesis, millimetre-wave frequencies were selected for wireless power transfer due to several potential advantages over microwave ones, particularly in applications such as powering IoT sensor nodes used for structural health monitoring, wearable devices, and pipe inspection robots. These can be summarised as:

- The gain of an antenna with a fixed aperture area increases linearly with frequency [34], this means that the path loss increase with frequency will be cancelled out up to some extent as shown in equations (1-1) and (1-2):

$$G = \frac{4\pi A_e}{\lambda^2} \qquad (1\text{-}1)$$

$$P_R = \frac{P_T G_T G_R \lambda^2}{(4\pi R)^2} \qquad (1\text{-}2)$$

  Where G is the gain of antenna, A_e is the effective aperture of the antenna, and λ is the free-space wavelength, P_T is the transmit

power, R is the distance between the transmitter and receiver, G_T and G_R are the gains of transmit and receive antenna respectively.

- Millimetre-wave WPT is safe for human skin up to a reasonable power levels because mmW are primarily absorbed by the skin and can't penetrate inside the body due to very small wavelength [35, 36]
- Wireless power transfer at 24 GHz are less likely to interfere with other frequency bands, which are used for communications because of directionality of antennas arrays which can be small in size but nevertheless highly directive.
- WPT at mmW is suitable for applications where there are constraints on the size of antennas, such as UAVs, pipe robots and IoT sensor nodes as shown in Figure 1-3 and high gain electronically steerable antennas are feasible with modest physical size.
- Wireless power transfer to robots inside a metal pipe for inspection is another application where lower frequencies cannot be used because the metal pipe acts as a waveguide, which has a cut-off frequency depending on its diameter. For example, the cut-off frequency for a 2.54 cm diameter pipe is 7 GHz.
- Due to the very narrow beam width and high directivity of mmW antennas a specific node can be interrogated further away without interfering with adjacent nodes, as shown in Figure 1-3(d).

Therefore mmW far-field WPT to IoT sensor nodes will be a good solution for the applications shown in Figure 1-3(a)(b)(c).

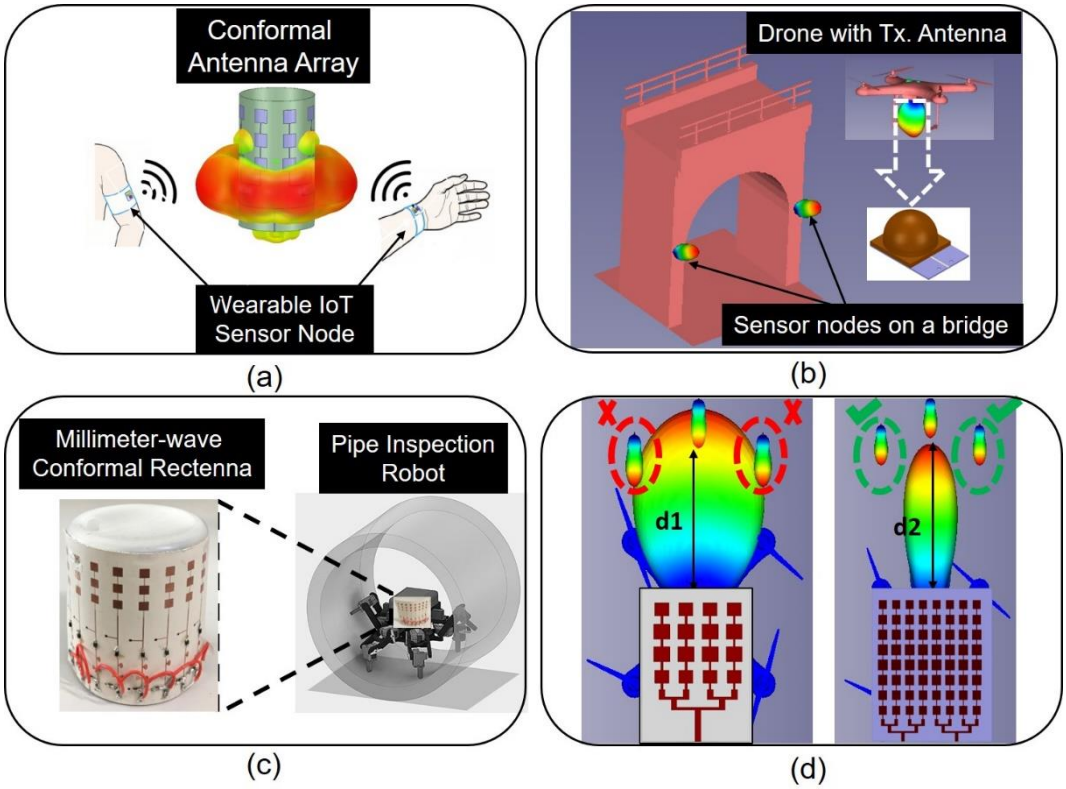

Figure 1-3 Millimetre-wave wireless power transfer (a) wearable IoT sensors, (b) structural health monitoring, (c) pipe robots (d) advantage of mmW over microwave

1.6. Research objective

The intent of this research work is to propose new modelling techniques and fabrication methods for the design and implementation of antenna arrays, phase shifters, waveguides, and rectifiers for mmW 5G communications and wireless power transfer applications. The proposed components are based on microstrip patch antenna arrays, substrate integrated waveguides and 3D printed structures. The major benefits of the proposed antenna arrays and components include high gain, low profile, low-cost, high efficiency, and ease of design and fabrication. Thus, they are promising

candidates for mmW next generation communications and WPT applications.

The major objectives and corresponding outcomes of this research work are:

1- Design and implementation of a new simplified approach for the excitation of microstrip patch antenna (MPA) arrays using higher order mode substrate integrated waveguide (SIW) cavity through aperture coupling. In this way the overall size and design complexity of MPA arrays have been reduced while their radiation pattern has been improved with low side lobe levels.
2- Design and implementation of low-cost 3D printed, low infill density dielectric lens antennas for gain enhancement.
3- A novel technique to design a compact and broadband reconfigurable SIW phase shifter for 5G phased array antennas.
4- Design and fabrication of low-cost and low-loss mmW hollow integrated waveguide using commercially available 3D printer.
5- Design and implementation of rectennas for wireless power transfer to IoT sensor nodes, wearable IoT devices, and pipe robots at mmW frequency bands.

1.7. Thesis organization and contributions

This thesis includes the analysis, design, implementation and measurements of mmW antenna arrays and several microwave components appropriate for 5G broadband wireless communication and

wireless power transfer applications. This thesis is organised into 6 chapters as follows:

Chapter 1 presents the motivation, objectives and corresponding outcomes of this research work as well as brief introduction of key techniques and applications of 5G communications such as millimetre-waves, beamforming, robotics and internet-of-things.

Chapter 2 includes a novel approach to the design and fabrication of low-cost and high-gain aperture-coupled microstrip patch antenna (AC-MPA) arrays with improved radiation pattern for mmW applications such as simultaneous wireless information and power transfer (SWIPT) and Internet-of-Things device connectivity. A higher-order mode SIW cavity is used to feed the MPA arrays through aperture coupling. The advantages of this method include low-cost, straightforward design and fabrication, as well as highly directional radiation pattern with lower side-lobe levels. Additionally, the overall size of the final antenna array is reduced as there is no need for large-area power dividers implemented in microstrip or SIW technology. The improved design approach is introduced and discussed in detail. Simulation and experimental results for 2x2 and 4x4 arrays are presented, demonstrating excellent agreement. This research work is already published by **Journal of Physics; Communications** [37].

Chapter 3 presents the design and implementation of low-cost, low-loss, easy to fabricate and integrate dielectric lens antennas at 28 GHz. The fabrication process features commercially available desktop 3D printer, CEL Robox RBX02-DM, using standard fused deposition modelling (FDM)

process. The integrated lens antennas (ILAs) were fabricated with a reduced infill percentage of 50%, which speeds up prototyping time, and simultaneously decreases dielectric loss, manufacturing cost and weight. A parametric analysis on infill density and infill pattern of dielectric lenses and free space dielectric characterization of Polylactic Acid (PLA) with reduced infill densities have also been experimentally verified and are presented in this chapter. This research work is already published by **IEEE Access** [38].

Chapter 4 presents a novel design technique of reconfigurable SIW phase shifters for phased array antennas in 5G wireless communications. The phase shifter consists of a simple single layer SIW structure, with different values of phase shift obtained through the use of a combination of reconfigurable conductive posts. The proposed phase shifter has an operational bandwidth of 6 GHz (26 GHz – 32 GHz), covering the main 5G candidate frequency bands. This chapter also presents a novel design and fabrication technique for low loss hollow integrated waveguides based on low cost 3D printing technology. The inner structure of HIW was fabricated using a desktop 3D printer. Copper rivets are used instead of electroplated via holes to make the side walls of HIW. The proposed design approach can easily be scalable to higher frequencies. Partial content of this chapter is based on the published paper in **EuCAP** [39].

Chapter 5 presents the design and implementation of complete mmW wireless power transfer system for IoT sensor nodes at 24 GHz. A comprehensive performance comparison of different rectifier topologies in simulations as well as experimentation is also discussed. All rectifier and

antenna array designs have been optimised using harmonic balance and full-wave electromagnetic simulations in order to maximise the RF-DC conversion efficiency and gain, respectively. Rectennas for three different practical applications including IoT sensor nodes, wearable devices, and pipe robots are presented and discussed in detail. Some results in this chapter are based on the published paper [40].

Chapter 6 concludes the thesis and also discusses some possible future work avenues.

Chapter 2. Higher-Order Mode SIW Cavity Excitation for MPA Array

2.1. Background

Substrate integrated waveguide technology has demonstrated certain advantages in its use in modern wireless communication systems [41-43]. SIW technology has been used extensively for the design of millimetre-wave antenna arrays, with SIW cavity-backed aperture-coupled microstrip patch antenna arrays having gained considerable attraction [44-47]. In this type of antenna array design, the benefits of MPAs are combined with the advantages of SIW technology [45, 46]. Additionally, aperture coupling has been demonstrated to offer higher radiation efficiency, lower return loss and less complexity as compared to other array feeding techniques such as microstrip and coplanar waveguide (CPW) transmission lines [48]. The drawbacks of a microstrip feed network include undesired back-lobe radiation and high insertion loss at mmW frequencies, which can significantly degrade the radiation pattern and efficiency of the antenna arrays [48].

Recent years have also seen an increase in research into methods to improve antenna performance using metamaterials, periodic structures and 2D materials. Metamaterials, being artificial composite materials, offer the

opportunity to make use of refraction properties not found in regular materials, including the well-known negative index. For antennas, metamaterials have been shown to offer the potential for miniaturization and control of radiation properties, including loading antenna arrays with meta-surfaces [49], while split-ring resonator arrays and other metamaterials have been demonstrated for antenna improvement [50]. Furthermore, tunable and reconfigurable metamaterials have been shown to offer exciting new opportunities for spatial electromagnetic wave processing in a range of photonic, terahertz and microwave applications [51]. These technologies have a wide range of applications in antennas, for gain and directivity enhancement, mutual coupling reduction and miniaturization [52-54]. In microstrip patch antenna arrays a key role of these techniques is to suppress the surface waves, which results in the gain enhancement and also reduction of side & back lobes, improving the radiation pattern. Near zero index materials can be used to make directive radiation towards the broadside to a planar interface [55]. In [56] the author presented the use of a metamaterial to concentrate the energy radiated by a source in a narrow cone. A high-directivity 5G antenna with near-zero refractive index metamaterial is presented in [54]. The gain of the antenna is improved by more than 6 dBi at 27 ~ 29 GHz based on the near-zero refractive index metamaterial. A graphene-based circular patch antenna was proposed for 6.8-7.2 THz. Polyimide, quartz, silicon dioxide and silicon nitride were used

as substrate materials and evaluated the performance of the patch antenna for individual substrate materials [53]. In a recent publication, microfluidics was used to reconfigure the polarization of antennas when a conductive liquid is injected into the substrate dielectric material [57]. Despite the many advantages of using the above mentioned technologies, the design and manufacture are complex and difficult as compared to the design approach proposed in this research work to enhance the radiation performance and directivity with very low side lobe levels by using a combination of dielectric materials to synchronize the aperture coupling from a higher order mode SIW cavity to the patch antenna array.

In [58], the design of a higher-order mode cavity-backed helical antenna array was proposed. The authors used a TE707 mode resonant cavity to couple power to a 16 element helical antenna array at a centre frequency of 11.8 GHz. In [47], a 2x4 patch antenna array was excited by aperture coupled longitudinal slots located in the SIW, at a centre frequency of 24 GHz. This antenna had a measured gain of 12.5dBi, a radiation efficiency of 62% and 3.35% bandwidth for a return loss level of 10 dB. In recent research papers [59-61], a similar design approach has been used to design SIW cavity-backed aperture-coupled antenna arrays using higher-order mode cavity excitation. In these antenna designs, a TE404 resonant mode was used for the excitation of 4x4 antenna arrays. Simulation results of similar design approach are given in Appendix B. Despite promising results

for the maximum realized gain, the reported antenna arrays have high SLLs of around -14 dB.

The main issues addressed in this research work are the distance between two adjacent peaks of the E-field in SIW cavity is equal to one-half guided wavelength ($\lambda_g/2$), which is always less than the one-half free space wavelength ($\lambda_0/2$) due to the relative permittivity ε_r of the dielectric substrate as $\lambda_g = \lambda_0/\sqrt{\varepsilon_r}$. However, according to the literature [62, 63], in order to minimize the side-lobe levels the spacing between array elements should be greater than or equal to one-half free space wavelength ($\lambda_0/2$), which would not be possible if the TE404 mode in SIW cavity was used for the excitation of 4x4 MPA array. The second issue is that the two adjacent peaks of electric field are 180^0 out of phase as shown in Appendix B, therefore the coupling slots have to be offset in order to make them radiate in phase. However, there might be additional issues in distributing power around every slot, which affects the radiation pattern [64].

To overcome these limitations related to higher-order mode SIW cavity excitation, TE303 and TE707 modes are proposed here for the excitation of 2x2 and 4x4 MPA arrays, respectively. Figure 2-2-1 presents the simulated E-field distribution inside the SIW cavities for the TE303 and TE707 resonant modes, where the '+' and '-' signs denote the positions of maxima and minima, respectively. There are 3x3 and 7x7 standing wave E-field peaks distributed for the TE303 and TE707 cavity modes, respectively. In

the antenna array design proposed here, only alternate maxima, having the same phase of the E-field, were used for the excitation of the MPA elements, through aperture coupling. This eliminates the need to offset the coupling slots and radiating patches to compensate for the 180º phase difference of adjacent maxima.

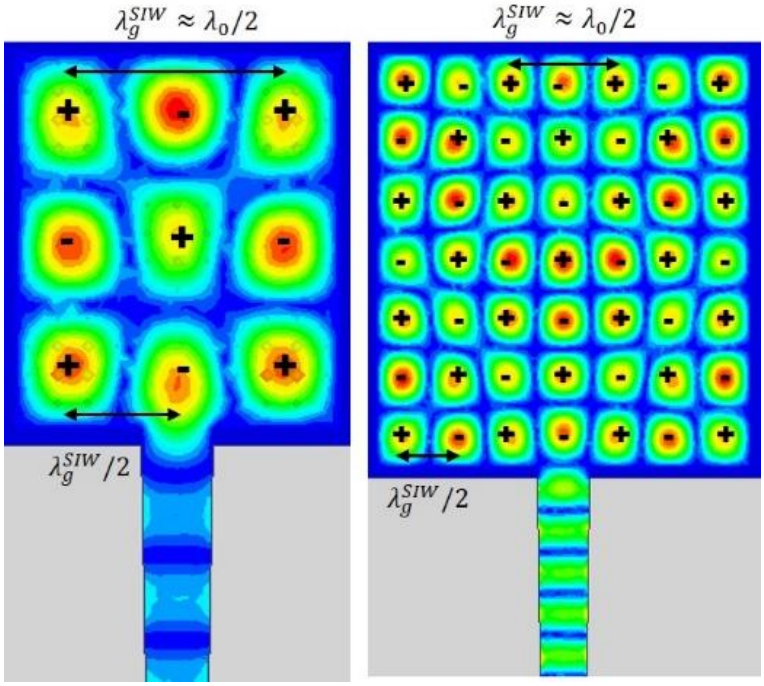

Figure 2-2-1 E-field distribution in the SIW cavities at resonance; a) TE303 mode, b) TE707 mode

This chapter presents a modified design approach for the excitation of aperture-coupled microstrip patch antenna arrays via higher-order mode SIW cavities. The proposed approach significantly improves the side-lobe levels of antenna arrays and is validated through the design and measurement of 2x2 and 4x4 millimetre-wave microstrip patch antenna

arrays fed by a higher-order mode SIW cavity, with a design frequency of 30 GHz. The advantages of this method include low-cost, straightforward design and fabrication, as well as highly directional radiation pattern with lower side-lobe levels due to the coupling slots are positioned over the appropriate *E*-field maxima to get optimal coupling and $\lambda_0/2$ distance between the array elements by using TE303 mode for the excitation of 2x2 MPA array. Additionally, the overall size of the final antenna array is reduced as there is no need for large-area power dividers implemented in microstrip or SIW technology. Proposed antenna arrays are well suited for millimetre-waves far field wireless power transfer applications in Internet-of-things (IoT) sensor nodes, sensing & diagnostics and automotive industry. WPT technologies use electromagnetic fields to transmit power through the air. One of the main requirements for an efficient WPT system is a highly directional antenna with low side-lobe levels and high radiation efficiency [65]. Using an antenna with such parameters maximizes the amount of RF power at the receiver, while at the same time minimizes the interference caused to other, non-WPT receivers [66]. Due to its inherently narrowband nature and low profile, this approach is particularly suitable for short-range simultaneous wireless information and power transfer to IoT devices and radar applications which do not require high data rates [66].

2.2. Analysis and design procedure

It is well known that there is a range of electromagnetic modelling techniques that can be applied to microwave, millimetre-wave and terahertz passive components and antennas. Effective medium theory gives a wide range of tools for the analysis of composite materials [67]. The Green's function approach is especially suited to multilayer structures and has been applied to many metamaterial problems, and the technique has recently been extended to analyse surface plasmon resonance at interfaces for metastructures [68]. The absorbing boundary condition method has also been used for metamaterial modelling, such as wideband absorbers using mushroom-type elements [69] and is important for substrate integrated waveguide modelling, which has been demonstrated using the finite-difference frequency domain method [70]. In this research work we used commercially available finite element method (FEM) full-wave electromagnetic solver Ansys HFSS™ to design and analyse the proposed antenna arrays and the proposed structures were fabricated and measured to validate the simulated results.

The general layout of a SIW cavity-backed aperture-coupled MPA array is shown in Figure 2-2. After an extensive literature review on SIW cavity higher-order mode excitation for MPA arrays and a series of simulations and optimization to improve the radiation pattern of antenna arrays using this excitation approach, we identified some drawbacks and limitations of using

the TE404 cavity mode for the excitation of a 4x4 MPA array as proposed by [59, 60]. Simulation model and results are presented in Appendix B.

2.2.1. Proposed antenna design

The proposed array configurations consist of a two- layer structure with a higher-order mode SIW resonant cavity in the lower substrate and the microstrip patch antenna array on the top metal surface of the upper substrate. The SIW cavity is fed by a microstrip line on the top surface of the lower substrate. Figure 2-3 and Figure 2-4 show the layer stack-up for the 2x2 and 4x4 arrays, respectively.

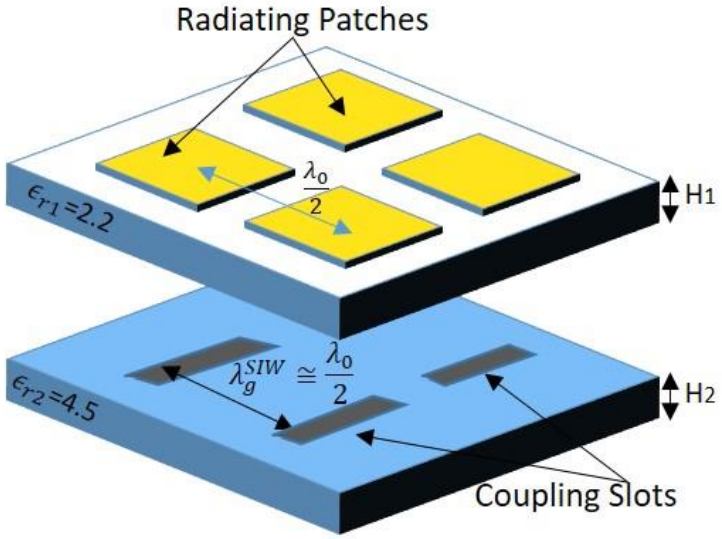

Figure 2-2 Geometry of proposed aperture coupled MPA array

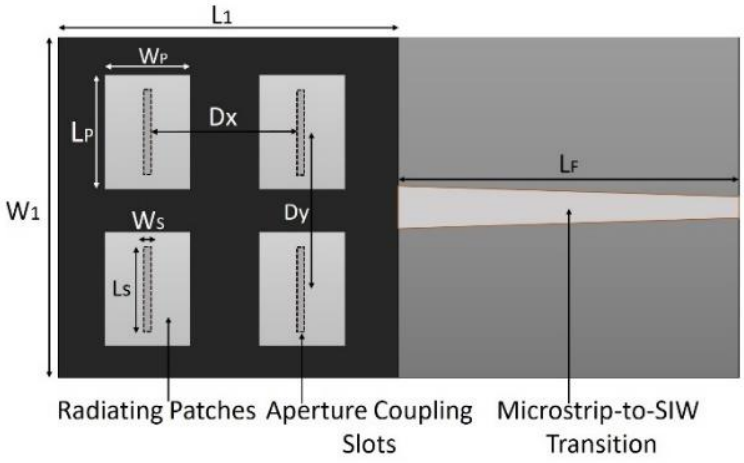

(a)

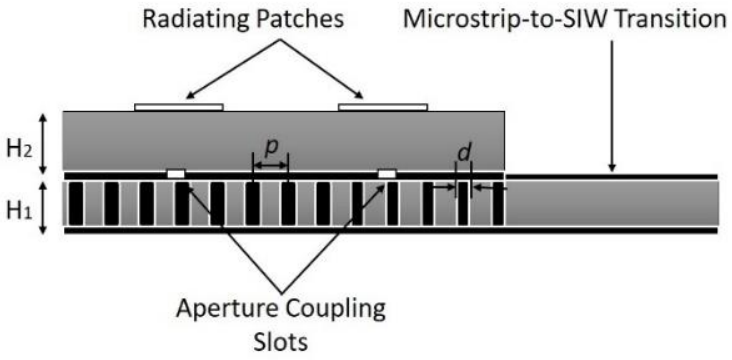

(b)

Figure 2-3 Layer stack-up illustration of the proposed 2x2 array; a) top view and b) side view

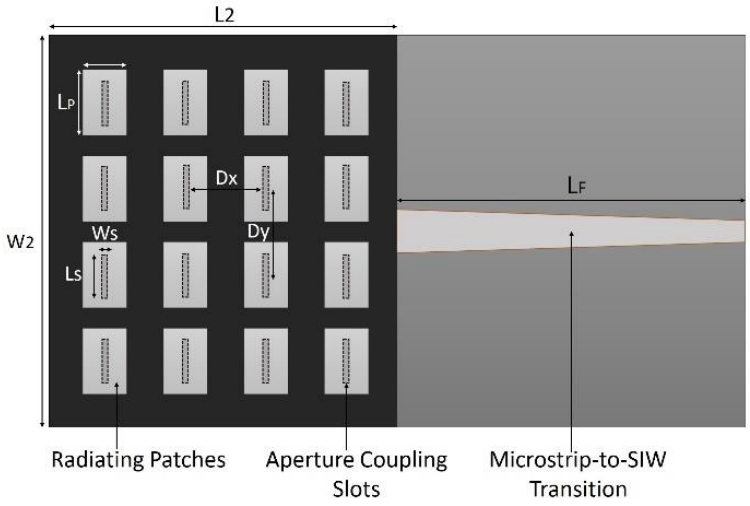

(a)

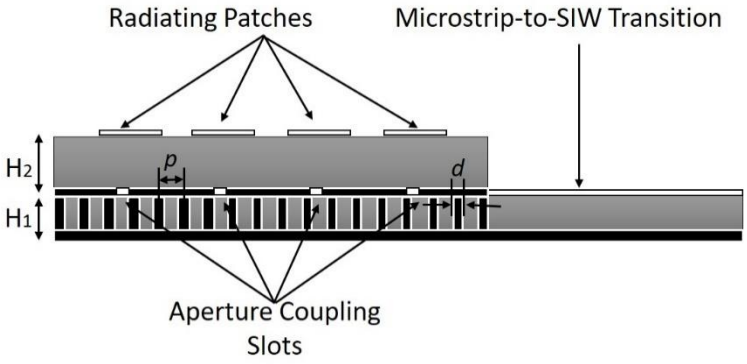

(b)

Figure 2-4 Layer stack-up illustration of the proposed 4x4 array; a) top view and b) side view

Transverse coupling slots located on the top metal layer of the SIW substrate allow the resonant cavity to excite the individual patch antenna array elements. The size and position of these slots determines the coupling between the SIW cavity and the antenna array, while the linear dimensions of the patches determine their operating frequency [48, 64]. It has been

shown that a transverse slot excitation provides efficient coupling and higher gain when compared to a longitudinal coupling slot due to the E-field distribution pattern of TEm0n modes inside the SIW cavity [44]. The proposed approach is straightforward in terms of feed network design, cost effective in terms of fabrication and is expected to give very low side-lobe levels compared to previous design approach as shown in Appendix B.

2.2.2. Design methodology

The array design methodology that we adopted is as follows:

Step 1) The dimensions of the individual SIW cavities are designed to support the TE303 and TE707 resonant modes at the design frequency of 30 GHz according to [71], which gives the resonant frequency of a TEm0n mode as:

$$f_{m0n} = \frac{c}{2\pi\sqrt{\mu_r \epsilon_r}} \sqrt{\left(\frac{m\pi}{w_{eff}}\right)^2 + \left(\frac{n\pi}{l_{eff}}\right)^2} \qquad (2\text{-}1)$$

The effective width and length of the SIW cavity can be calculated using the following equations [17]:

$$w_{eff} = w - \frac{d^2}{0.95p} \qquad (2\text{-}2)$$

$$l_{eff} = l - \frac{d^2}{0.95p} \qquad (2\text{-}3)$$

In the above, w_{eff} and l_{eff} are the effective width and length of the SIW cavity, c is the speed of light in vacuum, d is the via hole diameter, p is the distance between two adjacent via holes (centre-to-centre) and μ_r and ε_r are the relative permeability and permittivity of the substrate material, respectively. To simplify the design, w_{eff} was initially set equal to l_{eff}. The indices m and n had the values 3 and 7 for the TE303 and TE707 modes, respectively.

The diameter of the SIW via holes and the distance between two adjacent ones should be determined according to the following conditions:

$$d < \frac{\lambda_g^{SIW}}{5} \qquad (2\text{-}4)$$

$$p < 2d \qquad (2\text{-}5)$$

Step 2) The next step is to design the transverse coupling slots in the SIW cavity layer, as well as the 2x2 and 4x4 MPA arrays on the top metal surface of the upper substrate material, as illustrated in Figure 2-3 and Figure 2-4. In order to obtain coupling at the desired operating frequency, the physical size of coupling slots and radiating elements are calculated using equations (2-6 to 2-12) as reported in [41, 72]. The arrangement of the radiating elements is determined by keeping the distance from the centre of the first slot to the centre of the second slot as $\lambda_g^{SIW} = \frac{\lambda_0}{\sqrt{\epsilon_r}}$ and the distance from the centre of the last slot to SIW end wall as $\lambda_g/2$; As reported in [59, 60], the

TEm0n mode coupling level and return loss of the multilayer transition can be controlled by varying the physical slot width, and the physical slot length, while maintaining the slot position at the maximum E-field point. A parametric analysis and optimization results of the length and width of coupling slots are given in Appendix B. The initial dimensions of coupling slots were determined from equations 2-6 – 2-7 [72]:

$$l_s = \frac{\lambda_0}{\sqrt{2(\varepsilon_r+1)}} \tag{2-6}$$

$$w_s \leq \frac{l_s}{10} \tag{2-7}$$

In this proposed design, one coupling slot per patch element is used, with the slots positioned in the top metal wall of the SIW cavity in such a way as to coincide with a maximum of the $\boldsymbol{E}$-field. The radiation efficiency and bandwidth of AC-MPA array is better than SIW slot antenna array due to the aperture area of the radiating patches is larger than the radiating slots. Bandwidth enhancement is another reason of using radiating patches on top of coupling slots. The initial dimensions of the MPAs were determined according to well-known equations 2-8 to 2-12 for designing of microstrip patch antennas [62]:

The width of the patch is given as:

$$W = \frac{c_o}{2f_r}\sqrt{\frac{2}{\varepsilon_r+1}} \tag{2-8}$$

Where c_o is the speed of light in vacuum and f_r is the desired resonant frequency of the antenna.

The effective dielectric constant E_{reff} of substrate when $^{w}/_{h} > 1$:

$$E_{reff} = \frac{\epsilon_r+1}{2} + \frac{\epsilon_r-1}{2} + \left[1 + 12\frac{h}{w}\right]^{-\frac{1}{2}} \quad (2\text{-}9)$$

The effective length L_{eff} of the patch is:

$$L_{eff} = \frac{c_o}{2f_r\sqrt{E_{reff}}} \quad (2\text{-}10)$$

The length extension ΔL of the patch due to fringing effect of the E-fields is:

$$\frac{\Delta L}{h} = \frac{\left(E_{reff}+0.3\right)\left(\frac{w}{h}+0.264\right)}{\left(E_{reff}+0.258\right)\left(\frac{w}{h}+0.8\right)} \quad (2\text{-}11)$$

Now, the actual Length of the patch is given as:

$$L = L_{eff} - 2\Delta L \quad (2\text{-}12)$$

Step 3) The spacing between the neighbouring array elements is an important parameter which determines the phase difference between the two adjacent array elements and affects the radiation pattern of the antenna array [64]. In order to minimise the side-lobe levels and grating lobes, the centre-to-centre distance between the individual MPA array elements should be $\lambda_0/2$ at the operating frequency of 30 GHz [63]. Therefore, in order to excite all patch elements in-phase, the centre-to-centre distance of the transverse coupling slots should also be $\lambda_0/2$. Since the slots themselves are positioned above neighbouring in-phase maxima of the E-

field in the SIW cavity, it follows that the guide wavelength in the SIW cavity λ_g^{SIW}, should be equal to one-half the free-space wavelength $\lambda_0/2$. Therefore, the relative permittivity ε_r of the SIW substrate should be selected according to the relation $\lambda_g^{SIW} = \lambda_0/\sqrt{\varepsilon_r}$.

For the designs presented in this research work, Rogers TMM 4 with relative permittivity 4.5 and thickness 0.508 mm was used for the lower (SIW) substrate layer and Rogers RT/Duroid 5880 with relative permittivity 2.2 and thickness 0.787 mm was used for the upper (MPA) substrate layer. As the free space wavelength is 10 mm for a centre frequency of 30 GHz, the $\lambda_0/2$ spacing between the patches should be approximately 5 mm, and the guide wavelength λ_g^{SIW} was calculated to be approximately 5 mm for a substrate with $\varepsilon_r = 4.5$ at 30 GHz.

Step 4) Finally, parametric analysis in HFSS™ was used to find the optimal positions and dimensions of the coupling slots and radiating patches to maximize the coupled power from SIW cavity to MPA array and to minimize the side-lobe levels. The dimensions and position of the coupling slot significantly affect the coupling between the SIW and the microstrip patch, while the dimensions of the patch affect the resonant frequency of the antenna. A parametric analysis and optimization results of the length and width of coupling slots are given in Appendix B. A tapered microstrip-to-SIW transition is used to feed the higher-order mode SIW cavity. The length of the microstrip feed line is extended to avoid possible reflections due to the

coaxial end-launch connector. The final, optimised values for the dimensions of the proposed AC-MPA arrays are summarized in Table 2-1.

Table 2-1 Final design parameter values

Parameter	**Value (mm)**	**Parameter**	**Value (mm)**
L_1	12.0	**L_S**	3.25
W_1	11.5	**W_S**	0.25
L_2	25.0	**L_P**	3.0
W_2	25.0	**W_P**	3.5
H_1	0.51	**D_X**	5.5
H_2	0.787	**D_Y**	6.0

2.3. Measured results and discussion

The two arrays shown in Figure 2-6 were fabricated and measured using the in-house facilities at the University of Leeds. Several samples for both the 2x2 and 4x4 variants were fabricated and tested, the measured results are presented here.

The return loss performance of the antennas was measured in laboratory conditions using a Keysight N5247A PNA-X with 1-port Short, Open, Load

(SOL) calibration, bringing the S-parameter reference plane to the end of the coaxial cable used. The E-plane and H-plane radiation patterns were measured in a far-field anechoic chamber using a Keysight E8361C PNA and a 20 dBi WR-28 standard gain horn antenna. The gain at boresight of the proposed antenna was determined using the gain transfer method [73], with two 20 dBi WR-28 reference pyramidal horns used to establish a baseline. Radiation pattern measurement setup is shown in Figure 2-5.

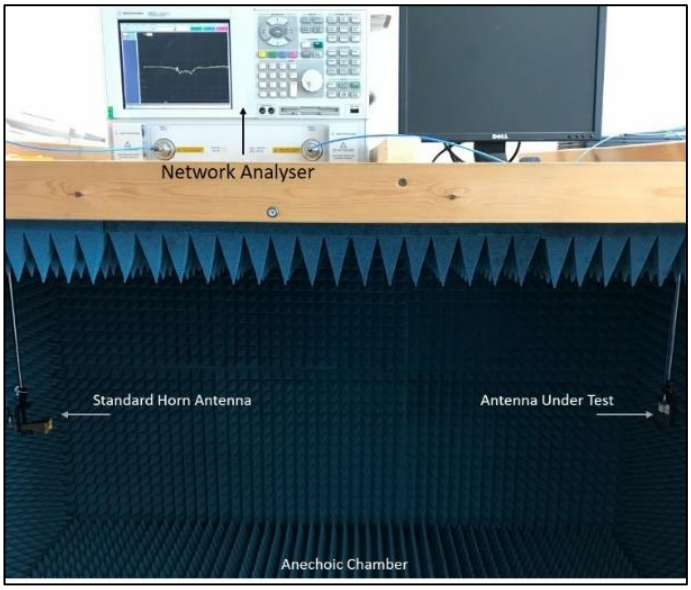

Figure 2-5: Radiation pattern measurement setup

To analyse the electromagnetic properties of the structures and the effects of surface waves, the finite element method is used to simulate their performance. The effects of surface wave excitation are lower antenna efficiency, degradation of the radiation pattern and undesired coupling between the elements in an array design [74, 75]. The reflection coefficient

and the radiation efficiency of proposed antennas clearly shows the minimum effect of surface wave propagation in proposed design. Surface currents distribution on top radiating patches of proposed antenna arrays are shown in Figure 2-7 which shows minimum surface wave propagation and mutual coupling between the arrays elements.

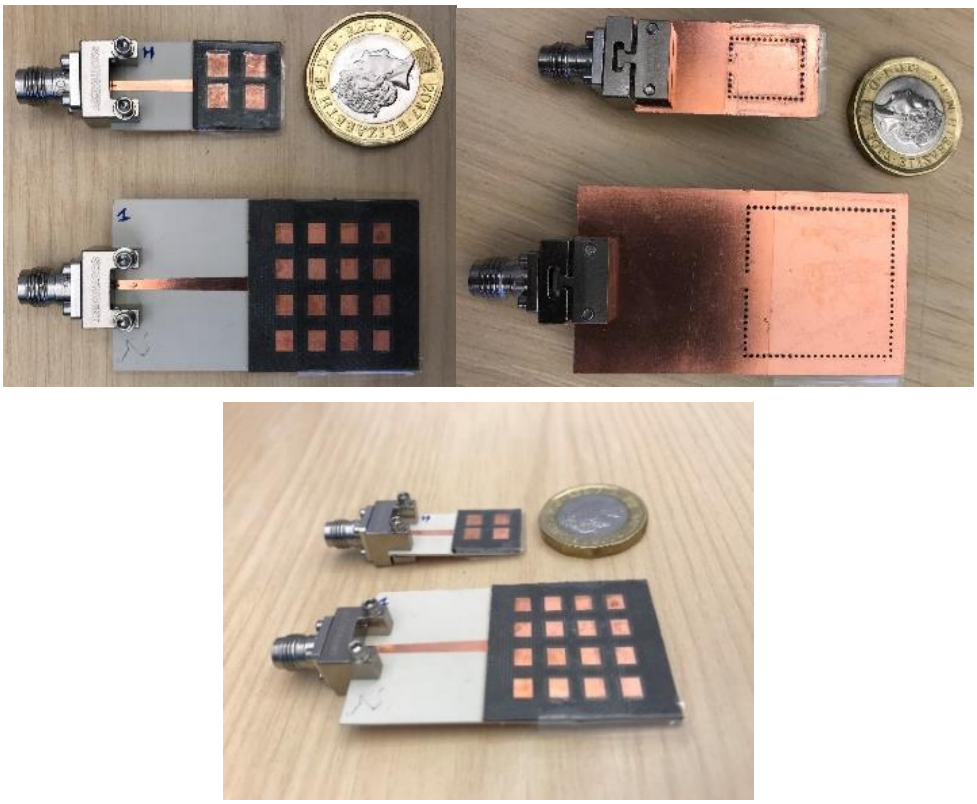

Figure 2-6 Fabricated AC-MPA array circuits, a) top view, b) bottom view and c) Side view

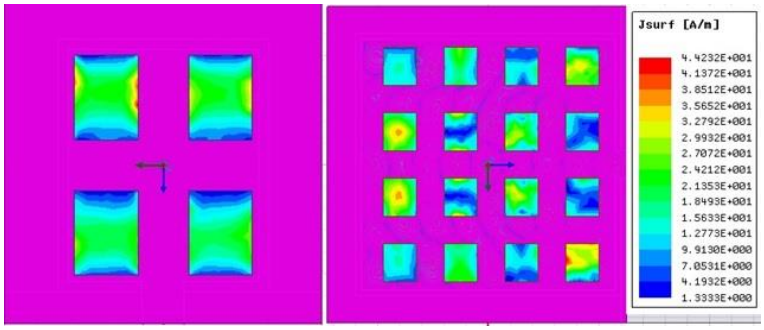

Figure 2-7 Surface current distribution on the top radiating elements at 30 GHz; a) 2x2 array, b) 4x4 array

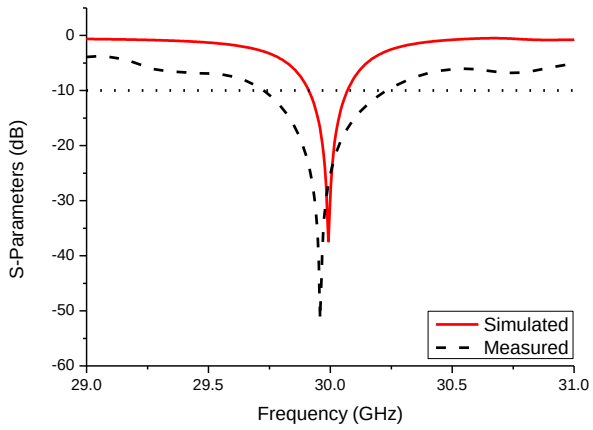

(a)

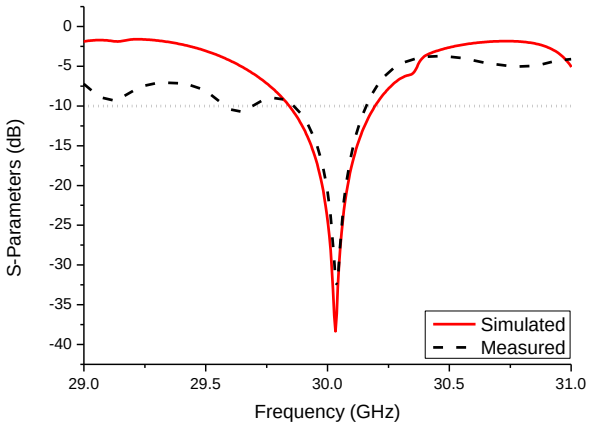

(b)

Figure 2-8 Simulated and measured return loss performance: a) 2x2 array and b) 4x4 array

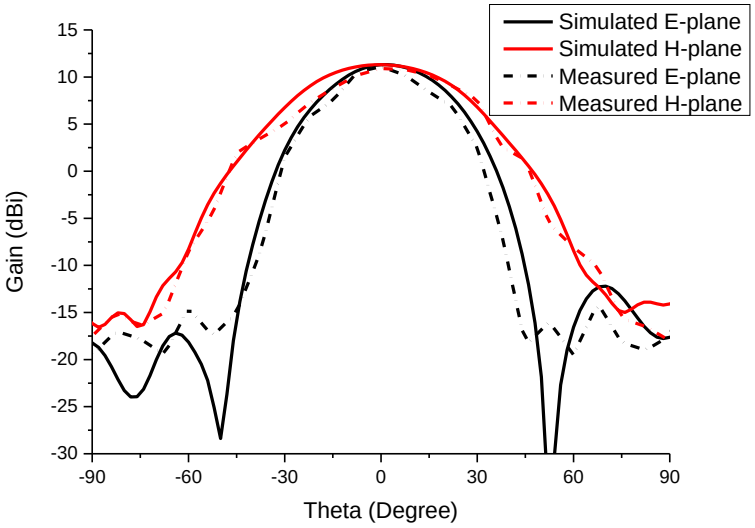

(a)

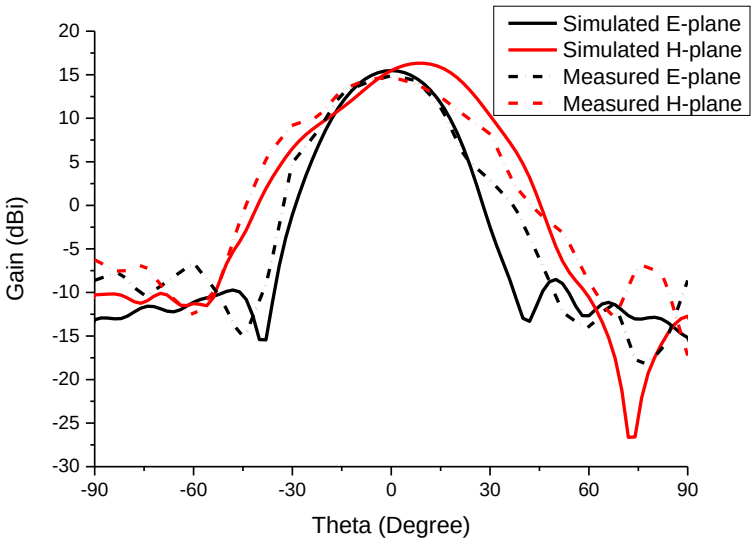

(b)

Figure 2-9 Simulated and measured E-plane and H-plane radiation pattern at 30 GHz: a) 2x2 array and b) 4x4 array

A comparison between the simulated performance in HFSS™ and the measurement results for both the 2x2 and 4x4 arrays is presented in Figure 2-8. A return loss level of 10 dB is used to define the operating bandwidth

of the antennas, found to be 505 MHz for the 2x2 array and 300 MHz for the 4x4 array. The graphs demonstrate excellent match between simulation and measurement, with minor differences in out-of-band performance. The differences are attributed to the coaxial end-launch connector, as well as higher-than-expected dielectric loss at millimetre-wave frequencies.

The simulated and measured results for the E-plane and H-plane radiation patterns of the two arrays are shown in Figure 2-9. There is again an excellent qualitative and quantitative agreement between the two, validating the proposed design method, 2x2 array provides a maximum gain of 11.1 dBi at the centre frequency of 30 GHz, with SLLs below -24 dB in the E-plane and -22 dB in the H-plane. Full-width at half-maximum (FWHM) for this array is found to be $38^0/56^0$ in the E/H plane. From Figure 2-9(b), the 4x4 array provides a maximum gain of 15 dBi, with SLLs below -29 dB and -26 dB for the E-plane and H-plane, respectively, while the FWHM in this case is $29^0/38^0$ in the E/H plane. The measured efficiencies of the 2x2 and 4x4 array are 83.2% and 86.5%, calculated as follows [62]:

$$D \approx \frac{32400}{\theta_{1d}\theta_{2d}} \qquad (2\text{-}13)$$

Where θ_{1d} & θ_{2d} are the half-power beamwidths in E & H plane (in degrees) respectively.

$$\varepsilon = \frac{G}{D} \qquad (2\text{-}14)$$

Where G is the gain and D is the directivity calculated from the approximate formula for planar antennas (MPA)**.**

The obtained results demonstrate the excellent performance of the proposed feeding and excitation approach of higher-order mode SIW cavity backed AC-MPA arrays. While this approach yields inherently narrowband antenna arrays, this is seen as an advantage as the target application is SWIPT for low data-rate IoT devices. Furthermore, these designs can be readily scaled to higher frequencies, potentially enabling SWIPT at the 60 GHz ISM frequency band. Table 2-2 demonstrates a comparison of results of proposed antenna arrays with other similar antenna designs in the open literature.

Table 2-2 Comparison of proposed design approach with recent published work in open literature

Ref.	Freq. (GHz)	Size (mm)	Gain (dBi)	SLLs (dB)		Efficiency %	Antenna type	SIW cavity mode	Design Complexity
				E-Plane.	H-Plane				
[60]	5.8	$2.11\lambda_o$x$2.11\lambda_o$x$0.18\lambda_o$	12.9	-14	-15	-	Slot Antenna	TE404	High
[59]	28	$2.33\lambda_o$x$2.33\lambda_o$x$0.19\lambda_o$	15.5	-14	-16	96 (Sim)	Slot Antenna	TE404	High
[58]	11.8	$5\lambda_o$x$5\lambda_o$x$0.19\lambda_o$	15~20	-	-	50	Helical	TE707	High
[47]	24	$4.8\lambda_o$x$1.28\lambda_o$x$0.13\lambda_o$	12.5	-20	-15	62	MPA	TE104	High

[61]	5.8	$1.68\lambda_o$x$1.68\lambda_o$x$0.17\lambda_o$	13.5	-22	-12	91	Slot Antenna	TE303	High
Proposed 4x4	30	$2.5\lambda_o$x$3\lambda_o$x$0.13\lambda_o$	15	-29	-26	86.5	MPA	TE707	Low
Proposed 2x2	30	$1.2\lambda_o$x$1.6\lambda_o$x$0.13\lambda_o$	11.1	-24	-22	83.2	MPA	TE303	Low

2.4. Chapter summary

In this chapter, a new approach for the design of AC-MPA arrays fed by a higher-order mode SIW cavity is presented and validated through measurement results of 2x2 and 4x4 arrays. The proposed arrays are straightforward to design and cost-effective to fabricate. The measurement results show excellent agreement with simulated ones. The arrays exhibit extremely low side-lobe levels in both the E-plane and the H-plane as compared to recent published work, summarised in Table 2-2, with high gains. The proposed antenna arrays have highly directional radiation pattern with high gain, and low side lobe levels which makes them a promising candidate for high frequency wireless power transfer to IoT sensor nodes.

Chapter 3. 3D-Printed Dielectric Lens Antennas

Fifth-generation (5G) wireless communication systems are expected to enhance reliability and drastically increase data rates to an ever-growing number of mobile users and Internet-of-Things devices [76]. To address this increase in telecommunication traffic requirements, portions of the underused millimetre-wave spectrum have been offered by regulators and used by service operators worldwide for fixed wireless access [77]. Candidate bands include 28 GHz, 38 GHz, 39 GHz, as well as 26 GHz, recently recommended by the United Kingdom's regulatory body, Ofcom [77].

However, millimetre-wave communication systems have limited range due to higher path loss and atmospheric attenuation and absorption [77]. This drawback has motivated the research to develop efficient and high-gain antennas, especially in the Ka band for 5G mobile communication. Currently, several solutions have been proposed to address this issue of limited range due to higher path loss at millimetre-wave frequencies [78, 79]. A particularly attractive and cost-effective method is gain enhancement using dielectric lenses, placed on top of source antennas such as microstrip patch antennas (MPAs) or substrate integrated waveguide (SIW) slot antennas [80-82]. These are also known as integrated lens antennas (ILAs).

The dielectric lens increases the directivity of the source antenna by transforming the spherical wave front of the radiated wave into a planar one [80, 83]. MPAs and SIW slot antennas are preferable for source antennas, due to the ease of their fabrication, straightforward integration with other planar circuits, low mass, and low profile [43, 48, 84].

3D printed lens antennas are already extensively used in the upper millimetre-wave frequency region, as evidenced by recent research, reported in [85-87]. A waveguide fed 3D printed lens antenna for the 60 GHz millimetre-wave Industrial, Scientific and Medical (ISM) band is presented in [84]. Industrial poly-jet 3D printing was used to manufacture the hemispherical lens, which provided gain enhancement of the source antenna. Another 3D printed “meta-lens” is proposed in [82] for gain enhancement at Ka band. The lens provided gain improvement of 7.5 dB at 32.5 GHz.

Recently, a combination of 3D printed dielectric lens and dielectric polarizers have also been reported for polarization conversion, in addition to gain enhancement at millimetre-wave frequencies [88, 89]. The drawbacks of these polarizers are fabrication complexity, lower gain enhancement, and more losses when compared to a stand-alone dielectric lens. The polarizers also increase the overall footprint of the antenna.

Most of the dielectric lens antennas reported in the literature have high manufacturing cost and excessive weight due to the use of expensive and dense dielectric materials such as quartz, in addition to costly fabrication techniques [15, 16]. Furthermore, gain improvement due to the addition of these lenses is not always quantified and reported in these works.

The use of commercially-available 3D printers for the quick and cost-effective prototyping of dielectric lens antennas has recently increased rapidly [83]. However, most reported results use industry-grade printers such as Stratasys™ or slower and more expensive fabrication techniques such as stereolithography (SLA) [15, 83]. Dielectric lenses fabricated through desktop 3D printers using fused deposition modelling (FDM) technology tend to be printed as solid objects (100% infill density), which increases the cost and weight of ILAs and decreases the radiation efficiency due to the high dielectric losses of FDM materials [81, 90-92].

In this chapter, the design and implementation of low-cost, low-loss, easy to fabricate and integrate dielectric lens antennas at 28 GHz are reported. The fabrication process features commercially available desktop 3D printer, CEL Robox RBX02-DM, using standard FDM process. The ILAs were fabricated with a reduced infill percentage of 50%, which speeds up prototyping time, and simultaneously decreases dielectric loss, manufacturing cost and weight. At the same time, the lens antennas provide considerable gain

enhancement of 6 dB, for two different types of source antennas - a 2x1 MPA array and a SIW slot antenna array. These were jointly designed and optimized to operate over the cluster of 5G candidate bands around 28 GHz. A parametric analysis on infill density and infill pattern of dielectric lenses and free space dielectric characterization of Polylactic Acid (PLA) with reduced infill densities have also been experimentally verified and are presented.

3.1. Dielectric Characterization of PLA Having Different Infill Densities

The dielectric constant and loss tangent of PLA filament given in supplier's datasheet is $\varepsilon_r = 2.7$ and tanδ=0.01 at 1 GHz. To accurately design and simulate the 3D printed dielectric lens antennas with reduced infill density, the effect on the complex relative permittivity of the 3D printed samples needs to be quantified for mmW frequency band. For this purpose, three PLA samples with dimensions of 50 x 50 x 25 mm^3 were fabricated using 25%, 50%, and 75% infill density. The resulting fabrication parameters of these samples are summarized in Table 3-1.

The Keysight Technologies™ 85071E free-space measurement software was used to measure the dielectric properties of the PLA samples having different infill densities over the frequency range of 26 - 32 GHz. Figure 3-1 shows the measurement setup for the complex relative permittivity, with

results from the free-space measurements given in Figure 3-2(a) and Figure 3-2(b). A network analyser and two standard gain horn antennas facing each other with sample them were used for transmission and reception of signals through PLA samples for dielectric measurements. Keysight 85071E software converts the transmission and reflection coefficients to dielectric properties i.e. ε_r and tanδ. Gated Reflect Line (GRL) technique was used to calibrate the system before starting actual dielectric characterization measurements. Further details on GRL calibration are given in Appendix C. Each sample was measured 3-4 times from different sides and using different distances, i.e. 25-40 cm, between the antennas to minimize the measurement error due to the anisotropic nature of PLA samples.

Measured results show that the relative permittivity and dielectric loss linearly decrease with a reduction in the infill density of PLA samples from 100% to 25%. The values of dielectric constant and loss tangent for different infill densities at 28 GHz are given in Table 3-1. Reduction of infill density also shows a clear impact on the fabrication time, weight and production cost, as summarized in Table 3-1.

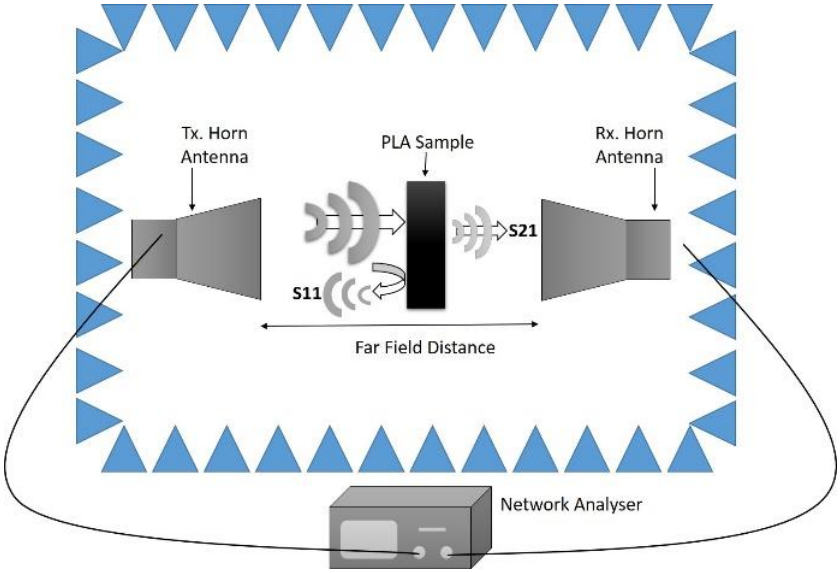

Figure 3-1 Free space measurement setup for dielectric characterization of PLA samples having different infill densities.

Table 3-1 Effect of infill density on the fabrication parameters

Metric	**25 % Infill**	**50 % Infill**	**75 % Infill**
Dielectric constant at 28 GHz	1.45	1.78	2.1
Loss tangent at 28 GHz	0.01	0.025	0.04
3D Printing time (HH/MM)	01:05	01:41	02:11
PLA Sample Mass (gram)	30.1	45	60.2
PLA Sample Cost (£)	0.79	1.6	2.39

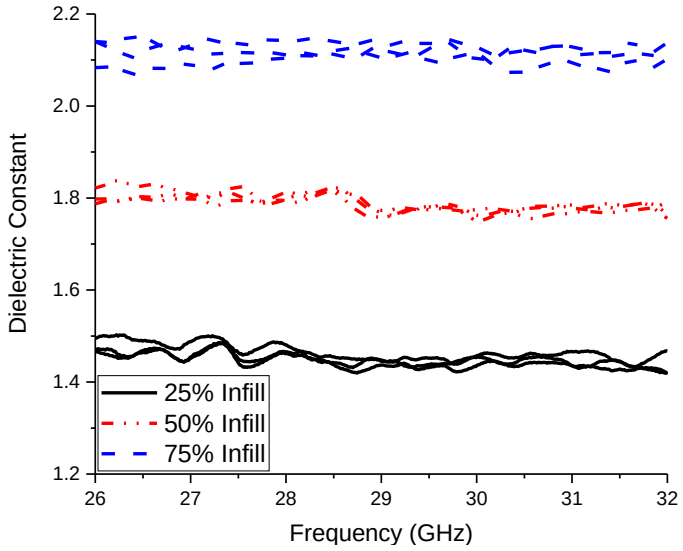

(a)

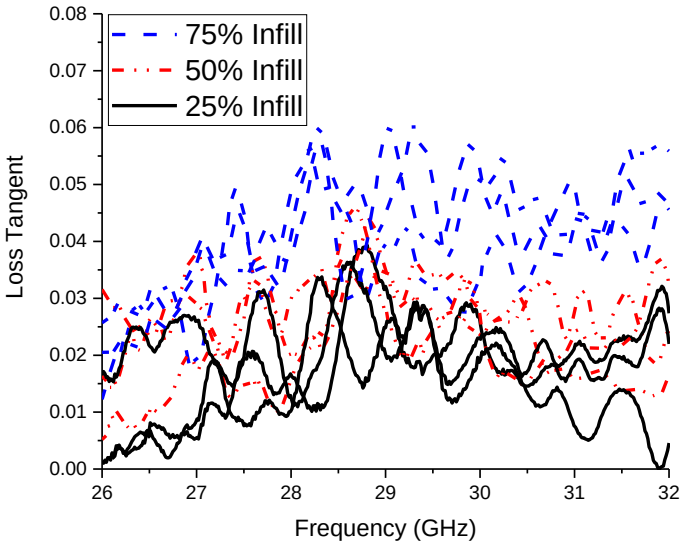

(b)

Figure 3-2 (a). Dielectric constant and (b) loss tangent of PLA samples having different infill densities from 26 GHz to 32 GHz, measured using the Keysight Technologies 85071E material characterization suite.

3.2. Impact of infill pattern and infill density on 3D printed dielectric lens

An extensive set of simulations, using Ansys HFSS™, was carried out to analyze the effects of infill pattern and infill density on the radiation properties of the 3D printed dielectric lenses. Three different types of infill pattern (rectilinear, triangle and honeycomb) with different infill densities (25%, 50% and 75%) were studied in the analyses. Figure 3-3(a), (b), and (c) show the surface current distributions at the top wall of radiation boundary above the dielectric lens at a far field distance for the three different infill patterns, respectively. It is evident that the dielectric lens with a rectilinear infill pattern has the strongest surface current density due to less inhomogeneity in its structure as compared to the other two patterns. Table 3-2 summarizes the simulated antenna parameters for the different infill patterns.

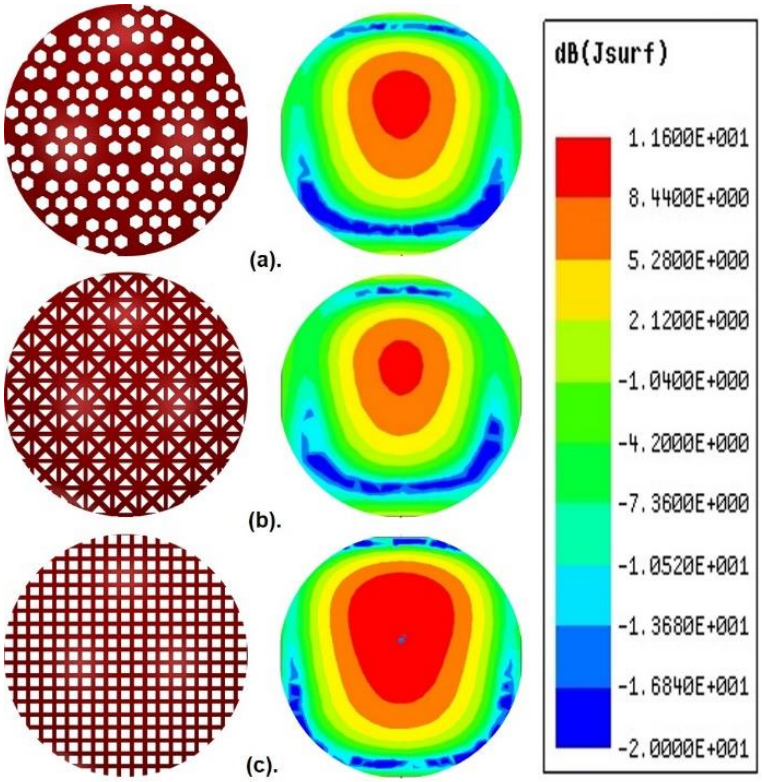

Figure 3-3 Infill patterns with surface current distribution on top wall of radiation boundary above the dielectric lens at a far field distance, (a). Honeycomb, (b). Triangle, (c). Rectilinear

Table 3-2 Effect of infill pattern on the antenna parameters

Parameters	**Infill Pattern**		
	Rectilinear	**Triangle**	**Honeycomb**
Gain (dB)	12.1	11.6	12.4
Radiation Efficiency (%)	82	76	78
Side Lobe Levels (dB)	-30	-22	-22
Return Loss (dB)	58	30	45
Simulation/Fabrication Time	Minimum	Moderate	Maximum
Surface Current Density (A/m)	3.6	2.2	2.7
Design Complexity	Low	Medium	High

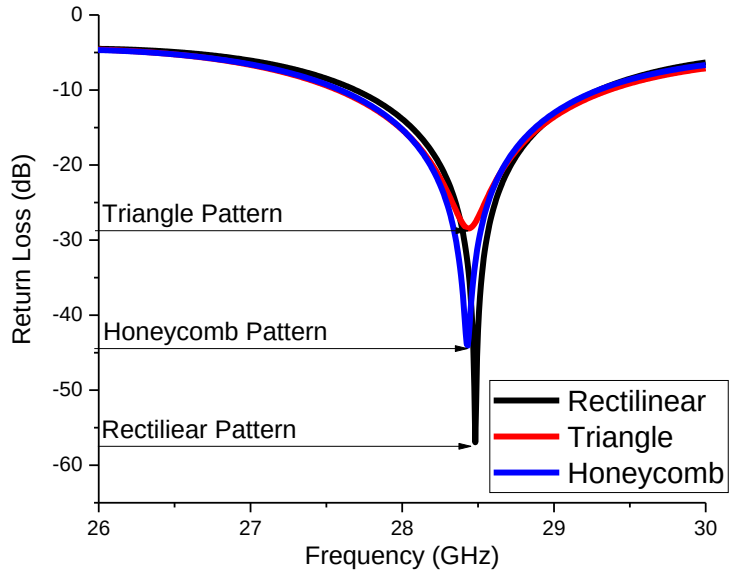

Figure 3-4 Impact of different infill pattern of dielectric lens on the reflection coefficient

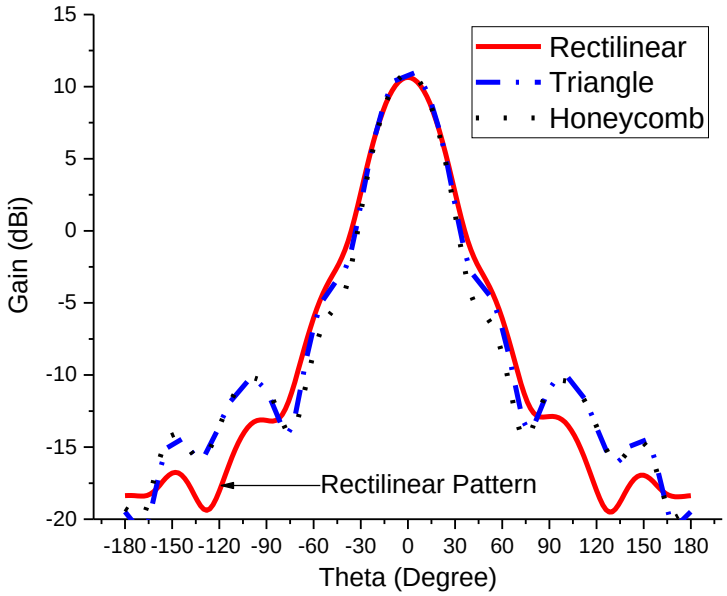

Figure 3-5 Impact of different Infill patterns of dielectric lens on radiation pattern

Figure 3-4 and Figure 3-5 depict the impact of the different infill patterns on the performance of the dielectric lenses in terms of reflection coefficient and radiation pattern, respectively. Rectilinear infill pattern shows the best impedance matching with return loss of less than 50 dB as compared to 30 dB and 45 dB for triangle and honeycomb infill patters, respectively. The peak realized gain is approximately constant for all three types of infill patterns, however the rectilinear one exhibits the best results in terms of radiation efficiency and side lobe levels, as summarized in Table 3-2.

The performance of the 3D printed dielectric lenses is affected by the infill density in a similar way to the infill pattern. The density can be varied to tailor the effective relative permittivity and loss tangent of the PLA - air mixture. The impact of infill density on both gain and return loss is shown in Figure 3-6(a) and Figure 3-7(a) for the SIW slot antenna and Figure 3-6(b) & Figure 3-7(b) for the MPA array. It is also summarized in Figure 3-8, for a fixed ratio of lens height to lens radius. It is evident that the gain is directly proportional to the infill density, whereas radiation efficiency is inversely proportional as shown in Figure 3-8(a) and Figure 3-8(b), respectively.

After analysing the results of the parametric study, it is concluded that the gain of ILAs is directly related to the infill density of the lens dielectric material. However, the impact of infill density on gain enhancement needs to be weighed against the impact on other parameters, such as cost, weight

and prototyping time. The decision to use 50% for subsequent experimental validation is therefore a trade-off between the gain enhancement on one hand, and the bandwidth, cost, weight, and prototyping time on the other. These factors must be considered in the design of ILAs. All these findings suggest that in-depth studies on infill patterns and infill density are necessary for design and development of dielectric lens antennas using 3D printing technology.

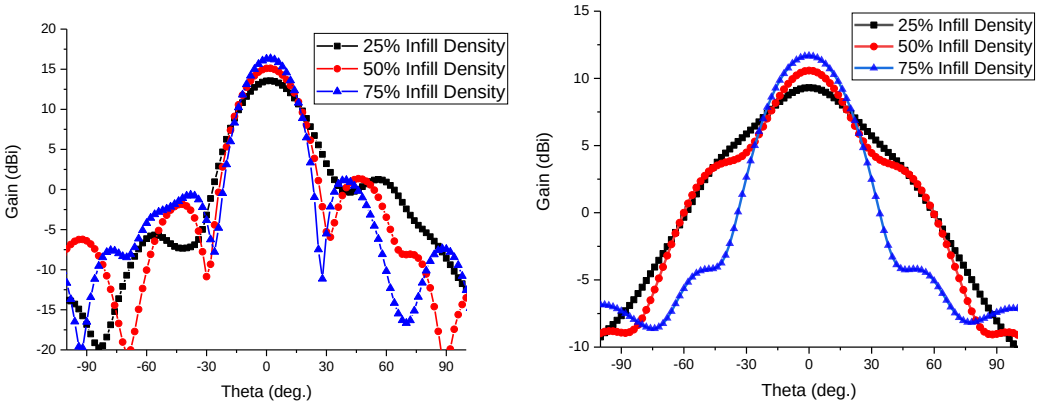

(a) (b)

Figure 3-6 Radiation pattern of ILAs at 28 GHz for different infill densities of dielectric lens materials (a). SIW (b). MPA

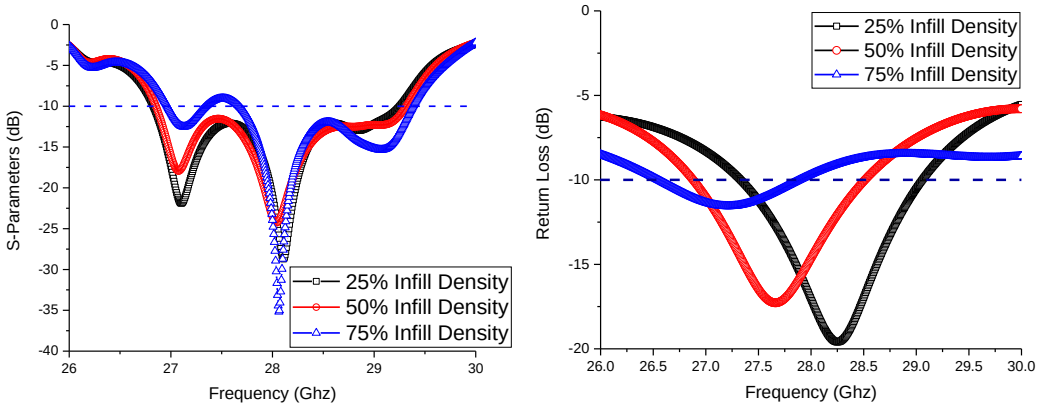

(a) (b)

Figure 3-7 Return loss of ILAs for different infill densities of dielectric lens materials (a). SIW (b). MPA

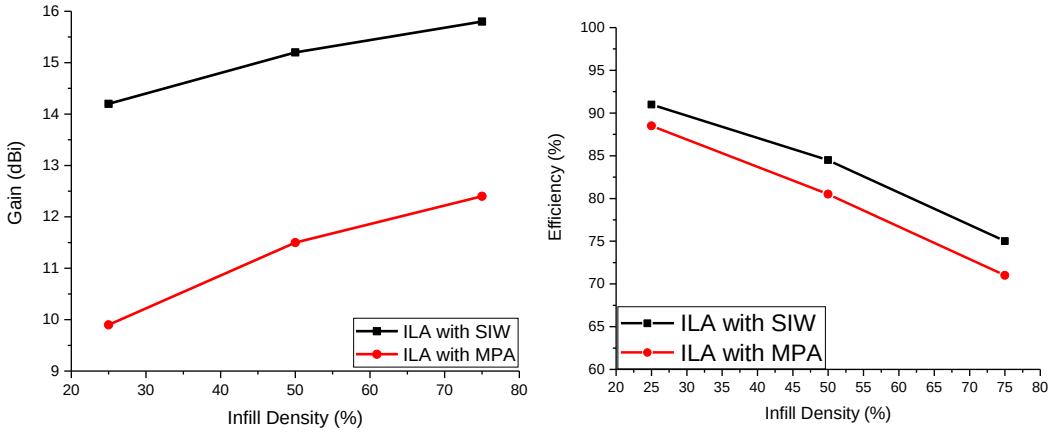

(a) (b)

Figure 3-8 (a) Gain and (b) Radiation efficiency for different infill density of dielectric lens material for H/R = 0.3 at 28 GHz

3.3. Design of source antennas

Two different antenna arrays were selected to be used as source antennas for the proposed ILAs, to demonstrate the applicability of the design and fabrication process to different scenarios. Both antennas were fabricated in-house at the University of Leeds, using modern PCB fabrication techniques. The substrate used in both cases was the low-loss RT/Duroid™ 5880 with relative permittivity $\varepsilon_r = 2.2$ and thickness of 0.787 mm.

3.3.1. SIW slot antenna

The SIW slot antenna array consists of three SIW cavities, designed according to [93] to support the TE_{102} mode at the center frequency of 28 GHz. The resonant frequency for TE_{m0n} mode of rectangular SIW cavity is calculated from the equations 2-1 to 2-5.

The TE_{102} mode was chosen to support two radiating slots in order to increase the base gain of the SIW slot antenna [43, 94]. The E-field distribution for the TE_{102} cavity mode is shown in Figure 3-9(b). In the top metal wall of each cavity, two T-shaped slots are etched over the position of maximum E-field, offset from each other to compensate the 180^0 phase difference between the two adjacent E-field peaks. Their linear dimensions and positions were optimized using the commercially available 3D EM simulator Ansys HFSS™, with the final structure shown in Figure 3-10(a).

The initial dimensions of the radiating slots were determined using equations 2-6 and 2-7 [41]:

A microstrip line in combination with a SIW power divider is used to feed the SIW cavities and to facilitate connection to test and measurement equipment through a Southwest Microwave 2.4 mm end-launch connector.

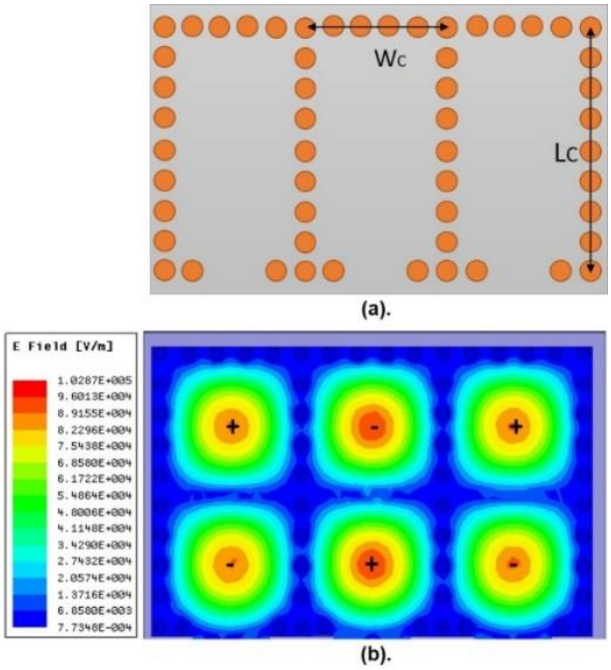

Figure 3-9 (a). SIW cavities and (b). E-field distribution for TE102 mode inside the SIW cavities

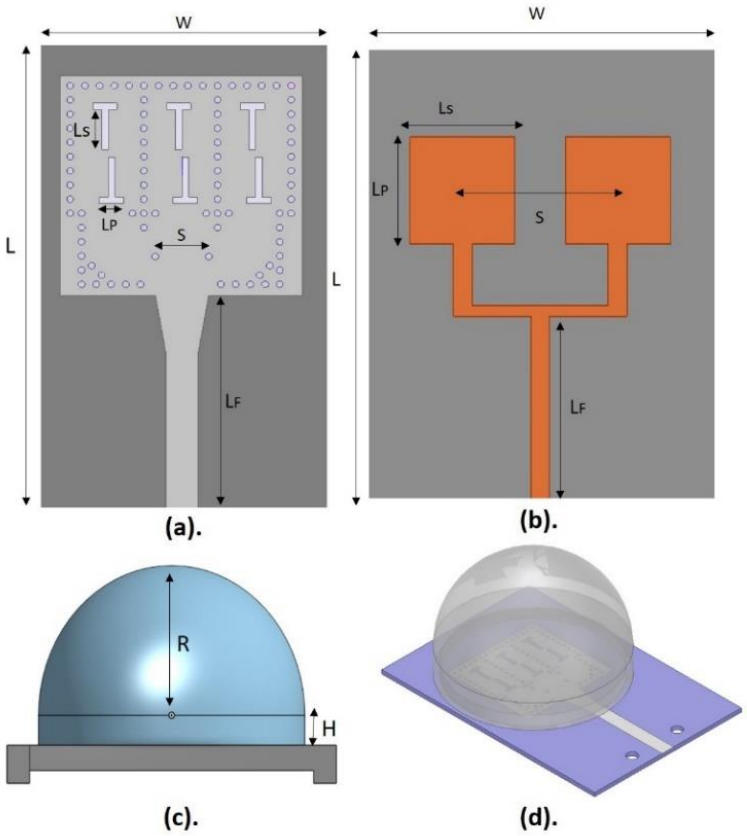

Figure 3-10 Integrated Lens Antennas fed by SIW slot antenna and MPA array (a) SIW slot antenna (b) MPA Array (c) side symmetric view of dielectric lens (d) simulation model of ILAs

3.3.2. Microstrip patch antenna array

The second antenna used as a source radiator for the dielectric lens was a simple 2x1 MPA array, again designed for a centre frequency of 28 GHz. A microstrip transmission line is used as the feeding network and to connect to the test and measurement equipment, similarly to the SIW slot antenna array. An illustration of the MPA array, together with the physical layout parameters, is shown in Figure 3-10(b).

The initial dimensions of the individual patches were determined using standard design method given in [95], before subsequent optimization in Ansys HFSS™. The centre-to-centre distance was specified to be $\lambda_0/2$ at 28 GHz, in order to minimize the grating lobes [63].

3.4. 3D printed dielectric lens design

It has been previously established that dielectric lenses provide an effective way to increase the directivity of a source antenna by reshaping the spherical wave front into a planar one [15, 83]. There are several different types of dielectric lenses [83], and in this research work an extended length hemispherical lens was chosen, due to its straightforward design. An extended hemispherical lens is fully defined by the parameters dome radius R, base diameter $D = 2R$, and base height H [86], which are illustrated in Figure 3-10(c).

A parametric analysis of the effect of R and H on antenna directivity is reported in [85], showing that increasing the base height H to radius *R* ratio increases the directivity of antenna but after a certain value of R/H the directivity starts decreasing. Results of parametric analysis on the base height H and radius R of the dielectric lens are given in Appendix C. Using these insights, together with the design process described in [16, 96], the initial values for the lenses were selected and simulation models created,

as illustrated in Figure 3-10(d). Full-wave EM simulation in the commercially available software package Ansys HFSS™ was then used to optimize the lens parameters for high gain, low return loss, and low side lobe levels. Optimization results are given in Appendix C. The final dimensions are listed in Table 3-3 for the two ILAs fed by SIW and MPA arrays at 28 GHz.

3.4.1. Dielectric lens fabrication

The lenses were fabricated using the commercially available desktop 3D printer (CEL Robox RBX02-DM) using the fused deposition modelling (FDM) technique with a vertical layer resolution of 0.1 mm. The material used was PLA (Polylactic Acid). PLA also has a slightly lower relative permittivity when compared to ABS, which is seen as an advantage, since using a high ε_r material for a dielectric lens has the drawback of excessive internal wave reflections [86]. The lenses were designed, simulated and fabricated using a 50% infill, i.e. only 50% of the internal volume of the lenses is made up of PLA. The infill pattern used was rectilinear one, which gives the best results as compared to triangle and honeycomb infill pattern as discussed in Section 3.2. The geometry of the lens designed in HFSS was exported as a Stereolithographic (STL) format and then imported into 3D-printing slicing and G-code generating software for manual adjustment of the infill density to tailor the permittivity and loss tangent accordingly.

Table 3-3 Final values of design parameters

Parameter	Value (mm)		Parameter	Values (mm)	
	SIW	MPA		SIW	MPA
L	45	22	**L_S**	3.6	4
W	31	20	**L_P**	1.5	3
R	16	8	**L_F**	20.5	9.5
H	5	2.5	**W_C**	6	-
S	4	5.5	**L_C**	18	-

3.4.2. Lens antenna integration

The integration of 3D printed dielectric lenses on top of source antennas is also a crucial task as well after fabrication of source antennas and dielectric lens antenna individually. A parametric analysis has already been done to optimize the exact position of dielectric lens on top of source antennas. For this purpose, a sliding channel was designed at the base of lenses to easily and accurately integrate and align the source antennas with the 3D printed dielectric lenses as shown in Figure 3-10(c). The advantage of using a sliding channel was not only the good alignment between the lens and

source antenna, but also the avoidance of any adhesive material used to combine the dielectric lens and source antenna that might affect the gain enhancement and radiation patterns of ILAs.

3.5. Experimental results

Several samples of each source antenna, i.e. SIW slot array and 2x1 MPA array, were fabricated and tested, with typical best results presented and discussed here. Photographs of these source antennas, both individually and after integration with the dielectric lenses are shown in Figure 3-11(a) and Figure 3-11(b).

The return loss and the E-plane and H-plane radiation patterns for both antennas, with and without lenses, were measured using the high-frequency measurement facilities at the University of Leeds. A Keysight N5247 PNA-X was used for the S_{11} measurement, with a 1-port mechanical Short, Open, Load (SOL) calibration to bring the reference plane up to the coaxial connector. A Keysight E8361C PNA was used to measure the radiation patterns in a far-field anechoic chamber, using a 20 dBi WR-28 standard gain pyramidal horn antenna as a transmit antenna. The gain at boresight of the proposed antenna was determined using the gain transfer method [73], with two 20 dBi WR-28 reference pyramidal horns used to establish a baseline. Radiation pattern measurement setup is shown in Appendix C.

These measurements were then compared to the simulation results obtained from Ansys HFSS™, using the Finite Element Method.

One such comparison for the SIW slot array antenna is presented in Figure 3-11 to Figure 3-14. A good overall agreement between predicted and measured performance in terms of return loss and radiation pattern is observed in either case, i.e. with and without the dielectric lens mounted on top of the source antenna. The antenna exhibits a wide bandwidth of 2.8 GHz at -10 dB return loss level, from 26.6 GHz to 29.4 GHz, covering most 5G candidate frequency bands. The benefit of the dielectric lens is clearly evidenced by comparing Figure 3-13 and Figure 3-14. The full-width at half-maximum (FWHM) decreases from 115^0 and 132^0 for the E and H planes, respectively, to 58^0 and 75^0. At the same time, the gain at the centre frequency of 28 GHz is increased from 9.8 dBi to 15.6 dBi.

(a) (b)

Figure 3-11 Fabricated prototypes of ILAs (a) source antennas (b) 3D printed dielectric lens on top of source antennas

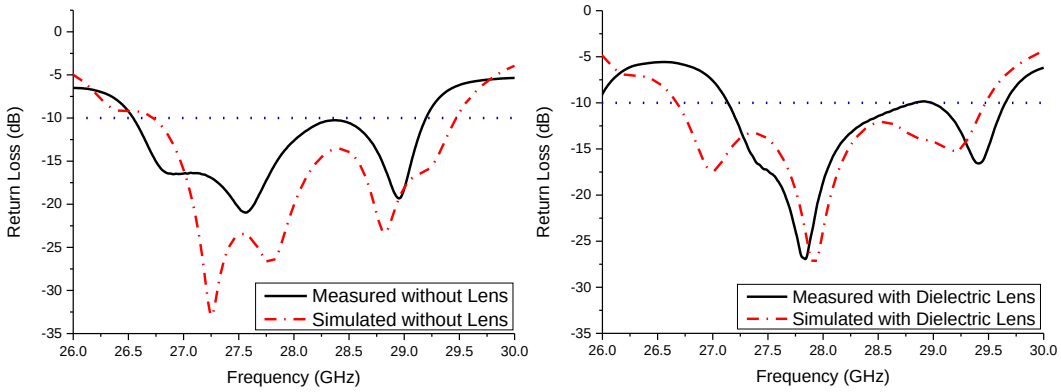

(a) (b)

Figure 3-12 S-parameters of SIW slot antenna (a) without dielectric lens, (b) with dielectric lens

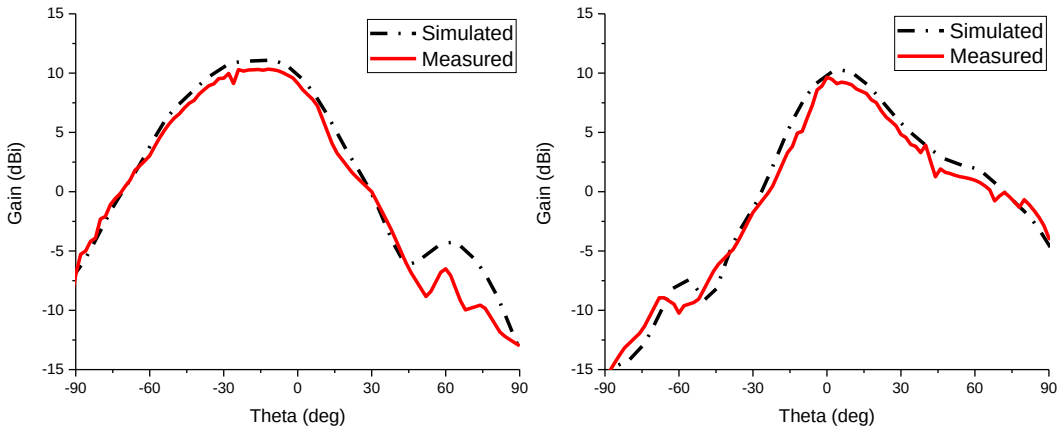

(a) (b)

Figure 3-13 Radiation pattern of SIW slot antenna without dielectric lens at 28 GHz (a) E-plane (b) H-plane

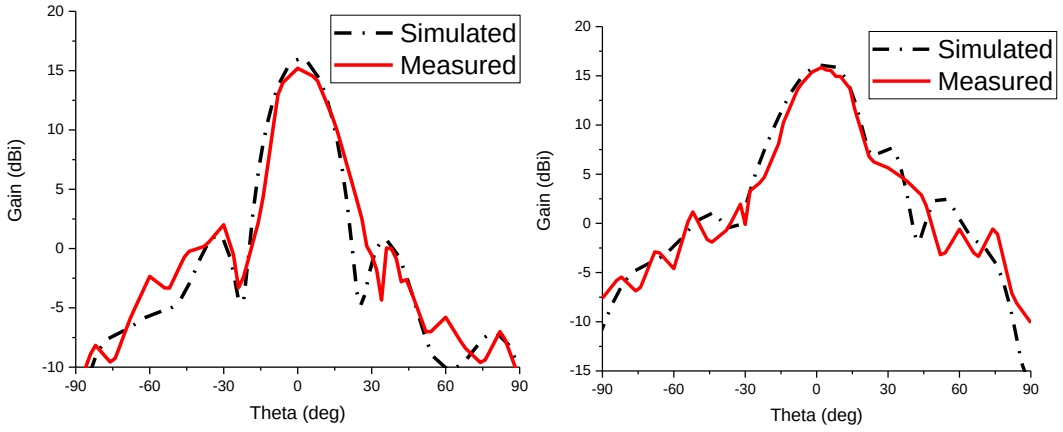

(a) (b)

Figure 3-14 Radiation pattern of SIW slot antenna with dielectric lens at 28 GHz (a). E-plane (b). H-plane

A similar comparison is shown in Figure 3-15 to Figure 3-17 for the 2x1 MPA array. Likewise, this antenna design exhibits a wide bandwidth at -10 dB return loss level, spanning the 28 GHz 5G frequency band. However, the gain enhancement in this case is lower, from 8.9 dBi to 12.4 dBi. The increase in directivity is again demonstrated by the reduction in the FWHM at 28 GHz, from $129^0/145^0$ to $90^0/122^0$ for the E/H plane, respectively. Finally, Figure 3-18 demonstrates that the achieved broadband gain is relatively flat over the frequency band of interest, 15.5 ± 0.5 dBi for the SIW ILA and 12 ± 0.5 dBi for the MPA ILA.

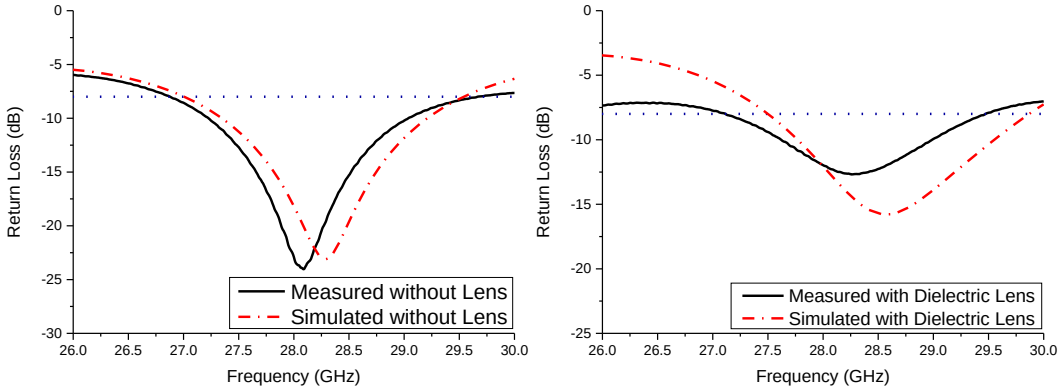

(a) (b)

Figure 3-15 S-parameters of MPA array (a) without dielectric lens (b) with dielectric lens

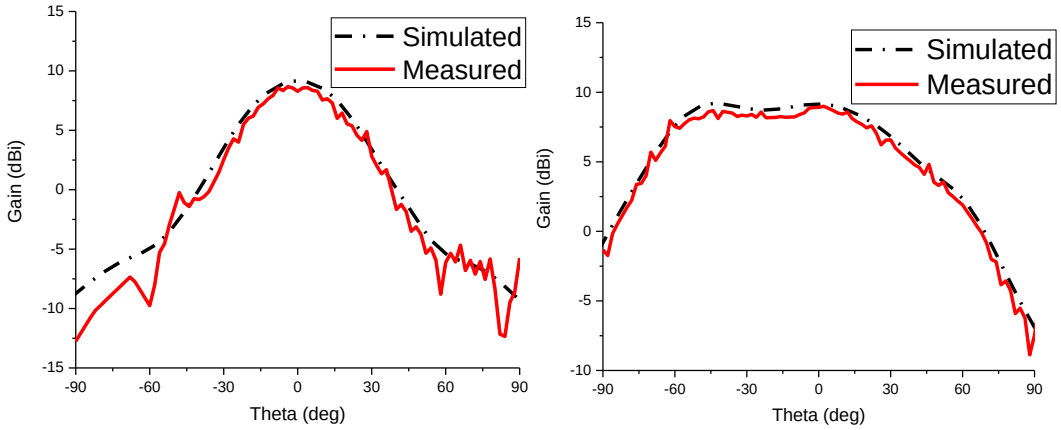

(a) (b)

Figure 3-16 Radiation pattern of MPA array without dielectric lens at 28 GHz (a) *E*-plane (b) *H*-plane

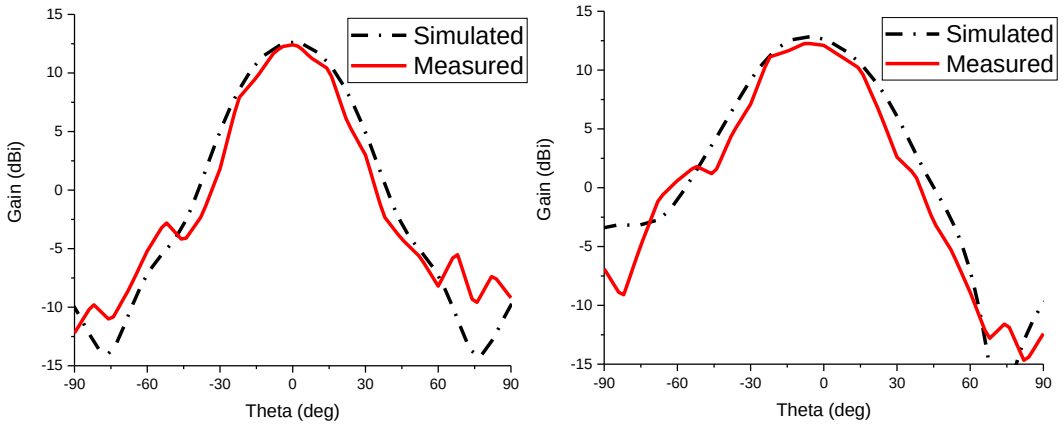

Figure 3-17 Radiation pattern of MPA array with dielectric lens at 28 GHz (a) *E*-plane (b) *H*-plane

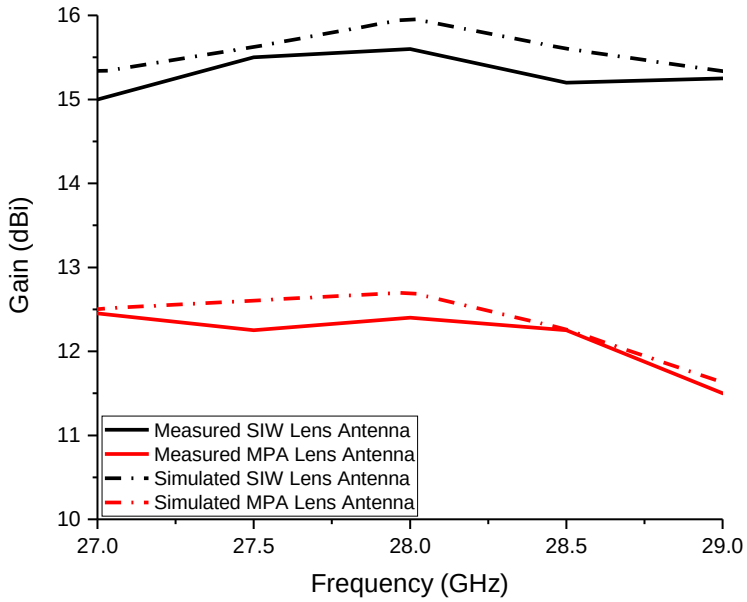

Figure 3-18 Measured gain vs frequency of MPA and SIW with dielectric lens antennas for H/R = 0.3

A summary of the obtained results for the antennas designed and developed in this thesis is given in Table 3-4. At the same time, a comparison on several key metrics with previously published results for dielectric lens antennas at similar frequency ranges is presented in Table 3-5, showing that our dielectric lenses compare favorably in terms of gain, side lobe levels, weight and cost with those produced using more expensive fabrication methods and high-cost and dense dielectric materials.

Table 3-4 ILAs performance comparison at 28 GHz

Metric	SIW Antenna	MPA Array
Bandwidth (GHz) with lens	26.6-29.4	27.6-29
Bandwidth (GHz) without lens	26.5-29.5	27.3-29.2
Gain (dBi) with lens	15.6	12.1
Gain (dBi) without lens	9.8	8.9
Side lobe level (dBi)	-20.5	-24
FWHM without lens E/H plane (0)	115/132	129/145
FWHM with lens E/H plane (0)	58/75	90/122
Efficiency (%)	84.5	81.25
Footprint (mm2)	31x45	20x22

3.6. Discussion and Applications

The reason for using two types of source antennas is to investigate and compare the performance of the proposed low infill 3D printed dielectric lenses for two different scenarios in terms of bandwidth, gain and efficiency. Antennas most commonly used as source antennas under dielectric lenses are the MPAs and SIW slot antennas, due to the ease of their fabrication, straightforward integration with other circuits, low mass and low profile. Dielectric lenses with SIW slot antennas have high bandwidth, gain and efficiency as compared to dielectric lens with MPA. SIW slot antenna have better impedance matching with dielectric lens when we compare the reflection coefficient of SIW slot antenna and MPA after integration with 3D printed dielectric lens in Figure 3-12(b) and Figure 3-15(b) respectively. In other words, SIW source antennas have more directional radiation pattern and achieve more gain enhancement after integration with dielectric lens as compared to MPAs. Therefore, ILAs with SIW are a promising candidate for 5G mobile communications. On the other hand, dielectric lenses with MPAs are more suitable for phased array and beam steering applications due to their straightforward integration with phase shifters, unlike SIW.

In our proposed research work we have used low cost 3D printing technology to fabricate low infill dielectric lenses which are efficient, light weight and straightforward to prototype and integrate with source antennas.

The ILAs presented in this chapter exhibit highly directional radiation patterns with correspondingly high gain, as well as low side lobe levels. Such lens antennas have already been successfully used in several industrial applications for gain enhancement and improving the directionality of the radiation pattern of a source antenna. One such application has been demonstrated in [97], where a hemispherical dielectric lens was integrated on top of a 122 GHz radar front end. The inclusion of this lens has led to a reported improvement in the directionality of the main beam from ±30° FWHM to ±4° FWHM, with a corresponding increase in detection range from 10 m to 100 m.

SIW-fed dielectric lens antennas for satellite communication systems at K/Ka band were presented in [81, 98]. The basic purpose of using the dielectric lens is to improve the radiation properties source antenna. A wideband circularly-polarized lens antenna is proposed for the 77 GHz automobile radar system [89]. In this case, a hyperbolic lens is fed by a rectangular horn antenna to increase the directivity and decrease the side lobe levels of source antenna for more accurate detection of the target by the radar system.

Finally, lens antennas can have potential applications in unmanned aerial vehicles (UAVs) for high-speed, point-to-point communication with sensor nodes. Using ILAs in this scenario offers several advantages and benefits.

One of them is retaining a small footprint while providing a 6 dB gain enhancement. An equivalent increase obtained using a larger array would require a quadrupling of the number of array elements and corresponding occupied area, which may not always be practical. The gain enhancement also provides flexibility from the point of view of the communication link budget. Either the transmitter power can be reduced, which will translate directly to decreased battery usage, or the distance between the UAV and the sensor node can be doubled. UAVs are known to lose aerodynamic stability and expend more energy when hovering at low altitudes due to the ground effect, therefore this increased distance will improve their flight time as well. In addition to this, the narrower antenna beam would allow the UAV to establish a link with a single node, without causing interference to adjacent ones. These concepts are illustrated in Figure 3-19 and will be a subject of a future study by the authors for smart city infrastructure monitoring.

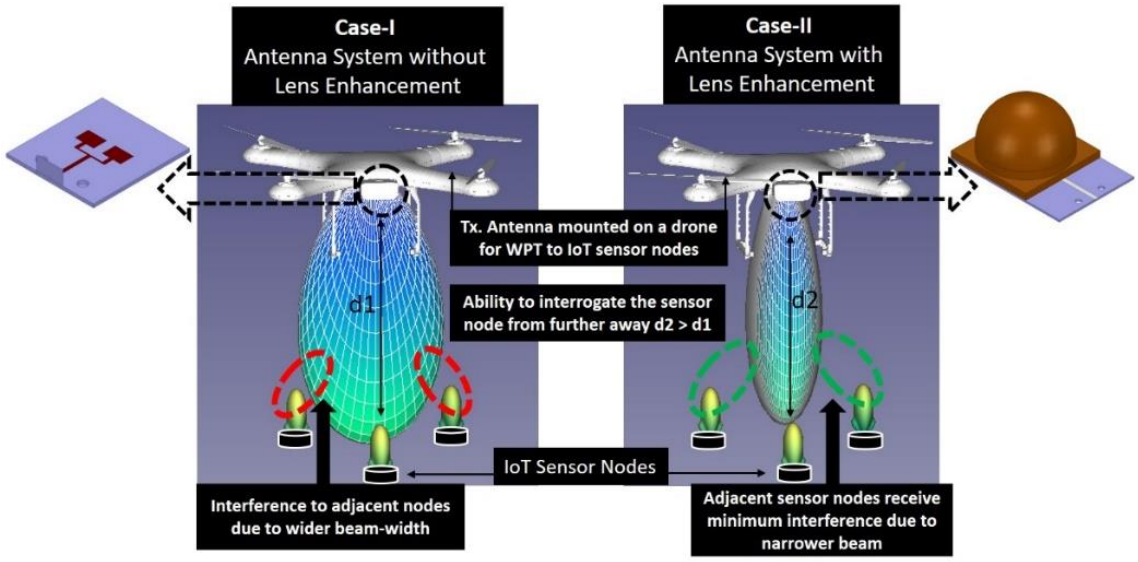

Figure 3-19 Application in sensor interrogation using unmanned aerial vehicles

Table 3-5 Comparison of the proposed ILAs with other ILAs reported in open literature

	[86]	[88]	[98]	[91]	[99]	[100]	[16]	[81]	Proposed	Proposed
Source Antenna	Waveguide	Waveguide	SIW	MPA	Dipole Array	Helical Antenna	Aperture coupling	SIW	SIW	MPA
Lens Size (mm)	20	10.33	7	15	23	70	44	7	30	16
Freq. (GHz)	51-67	60	18-32	50 – 67	14-20	8.8	28	19.5-32	26.5 – 29.5	27.5 – 29
Gain(dBi)	21.4	15	6.2-7.6	13.1	11.2	12.9	11	8	15.5	12.1
SLLs(dB)	-12	-10	-	-23	-11	-16	-15	-16	-20.5	-24

Fabrication Method	SLA 3D Printer	Poly-jet 3D Printing	N/A	HDI Organic	Industrial Multi-Jet Printing	Industrial Poly-jet printing	CNC	Industrial 3D printing	FDM Desktop 3D Printer	FDM Desktop 3D Printer
Lens Material	Polymer $\varepsilon_r = 2.9$	RGD240 material	Polymer $\varepsilon_r = 3.5$	ABS	Plastic resin	Polymer $\varepsilon_r = 2.6$	Rexolite	PTFE	50% PLA/50% air	50% PLA/50% air
Cost	High	High	High	High	Low	High	High	High	Very Low	Very Low

3.7. Chapter summary

In this chapter, we have presented a simple, low-cost method of design and fabrication for dielectric lens antennas for wireless communication at millimetre-wave frequencies. The impact of the infill pattern of the 3D-printed dielectric lens on the performance of ILAs and dielectric characterization of 3D-printed PLA samples with varying infill densities have been presented for the frequency range 26-32 GHz. Results for two different types of antennas, usable in different scenarios, are analyzed, and compared. The use of commercially available 3D printing technology with low infill density for the rapid prototyping of highly-efficient dielectric lens antennas is demonstrated. Excellent agreement between simulation and measurement results has been demonstrated.

Chapter 4. Millimetre-waves SIW Phase Shifter and 3D-Printed Hollow Integrated Waveguide

In recent years, the components and devices implemented in Substrate Integrated Waveguide (SIW) technology are emerging as a promising candidate for microwave and millimetre-wave transmission. SIW technology is widely used for the design and implementation of RF and microwave components such as phase shifters, filters and antennas arrays because of its low profile, high Q-factor, low-cost fabrication and straightforward integration with other circuits [101, 102]. SIW is a more competitive technology as compared to other planar technologies such as microstrip line transmission or coplanar waveguide (CPW) due to lower loss transmission and higher power handling capability [101]. The drawbacks of a microstrip line transmission and CPW include undesired radiation and high insertion and propagation loss at millimetre-wave and terahertz frequencies, which can significantly degrade the efficiency of the components [103, 104]. The conventional metallic rectangular waveguides despite having low loss and high Q-factor are not suitable for the design of low cost, light weight applications due to their bulky size, relatively high cost and their difficult integration with microwave and millimetre-waves planar circuits [105].

4.1. Electronically controllable SIW phase shifter

Phase shifters, which are circuits that change the phase of a signal with minimum insertion loss, are fundamental to the operation of electronically steerable phased array antennas at microwave and millimetre-wave frequencies [106]. Components and devices implemented in SIW technology are emerging as a promising candidate for high Q-factor circuits and low loss antenna feeding networks, due to the reduced amount of conduction loss [107]. SIW phase shifters are widely used because of their low profile, high Q-factor, low-cost fabrication and straightforward integration with other circuits [108]. Conventionally, these circuits use fixed metal posts to perturb the propagating electromagnetic field in order to provide a fixed value of phase shift between their input and output [27, 109-111].

However, there are only a handful of reports on electronically controllable SIW phase shifters. A circuit using a design approach similar to the one reported in this work has previously been demonstrated over the X-band frequency range [112], achieving a maximum phase difference of 45^0 using 4 PIN diodes; however the diodes used were housed in large ceramic packages, which in turn imposed a limit on the minimum size, and hence maximum frequency, of the SIW circuit. In another research work, a phase shifter implemented in a multilayer SIW technology was presented, which utilised aperture coupling slots alongside PIN diodes for electronic control

[113]. The circuit provided a 90^0 phase shift with an operational bandwidth of 4 GHz by using 10 PIN diodes. Nevertheless, the complicated multilayer SIW structure resulted in complex fabrication requirements. Realising an electronically controlled SIW phase shifter with a wide operating bandwidth and low insertion loss has remained a challenging task for the research community [114].

In the first part of this chapter a new design approach for a compact and broadband SIW phase shifter is presented. The phase shifter consists of a simple single layer SIW structure, with different values of phase shift obtained through the use of a combination of reconfigurable conductive posts. The proposed phase shifter has an operational bandwidth of 6 GHz (26 GHz – 32 GHz), covering the main 5G candidate frequency bands, and has an good insertion loss performance of less than 3 dB at the centre frequency.

4.1.1. Design of the SIW phase shifter

4.1.1.1. Initial design and operating principle

There are several different ways to implement a phase shifter circuit using SIW technology. The simplest way is by adjusting the length of the SIW to provide a phase shift relative to another transmission line. Another approach to introduce a fixed amount of phase shift in an SIW circuit is to insert vertical

metal posts at carefully selected positions inside the waveguide channel [115].

This work proposes a novel design approach for SIW phase shifter, using either 2 or 4 metal posts that can be switched between providing an inductive or capacitive loading of the SIW transmission line. Initially, the switching is provided manually by using metallic strips over the ring gap between the conductive post and the top metal surface and later these metallic strips could be replaced by pin diodes to make the phase shifter electronically controllable, naturally this would require an optimization and slight redesign stage to take account of the effect that the diode related parasitic will have on the ideal behaviour of the shorted metal posts without the diodes providing the capacitive shorts. The illustrations of the proposed circuits are shown in Figure 4-1 and Figure 4-2, respectively. The relevant dimensions of the phase shifter circuits are *Lf*, length of the microstrip feed line, *L1* and *L2*, length of SIW line for a phase shifter with 2 and 4 reconfigurable conductive posts respectively, and *W*, width of the SIW transmission line. Furthermore, *x* and *y* denote the offset of the centre of the switched metal posts from the geometric centre of the SIW transmission line and a ring gap between the reconfigurable conductive posts and top metallic surface of SIW.

The first step of the phase shifter design is to ensure single mode propagation over the frequency band of interest, i.e. 26 GHz – 32 GHz. The

initial dimensions of the SIW were calculated using the equations (2-1) to (2-5) provided in [71] for an RT/Duroid 5880 substrate with ε_r = 2.2 and thickness *h* = 0.787 mm. These were subsequently optimized in the commercial 3D FEM software HFSS, and the final SIW dimensions are listed in Table 4-1.

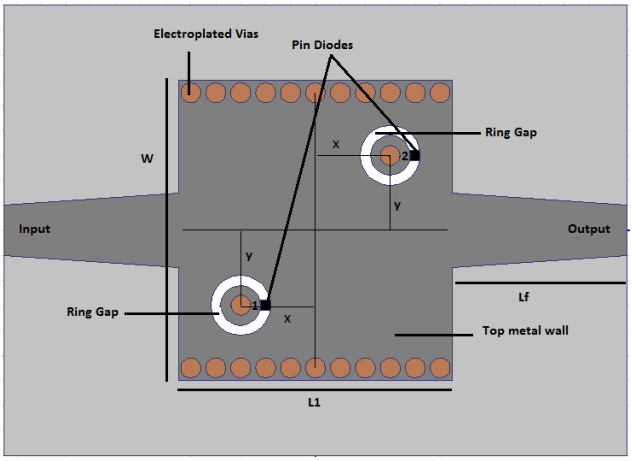

Figure 4-1 SIW phase shifter with 2 reconfigurable metal posts.

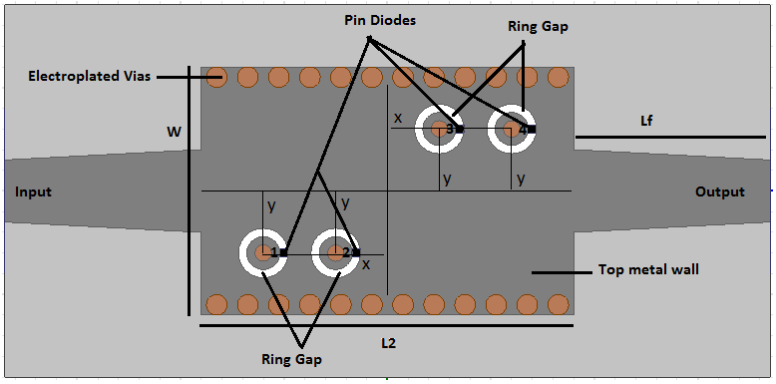

Figure 4-2 SIW phase shifter with 4 reconfigurable metal posts.

Table 4-1 Parameter values of proposed SIW phase shifters

Parameter	**Value**	**Parameter**	**Value**
L1	6.00 mm	x	1.50 mm
L2	8.00 mm	y	1.50 mm
W	5.50 mm	d	0.50 mm
Lf	4.55 mm	p	0.80 mm

The next step is to introduce the metal posts, each offset at a distance *y* from the centre of the SIW width and a distance *x* from the centre of the SIW length, which are used to achieve the required phase shift. There is an annular ring gap between the metal posts and the top metal wall of the SIW line, where the switching metal strips are mounted. The metal posts are then switched between providing capacitive loading (without metal strip, or state '0') and inductive loading (with metal strip, or state '1') of the SIW transmission line, thereby resulting in a phase difference between the different states of the metal posts.

Simulations have been carried out for different values of the *x* and *y* offsets to explore the range of obtainable phase difference as well as their effect on the insertion loss. It was found that moving the posts closer to the centre

line of the SIW increases the phase difference, as does moving them closer to the edges of the SIW line.

4.1.1.2. PIN diodes

A DSG9500-000 planar beam-lead PIN diode could be used to provide switching capability. The equivalent circuit of the diode and its physical dimensions are shown in Figure 4-3, while the parameters used in the simulation model are summarised in Table 4-2.

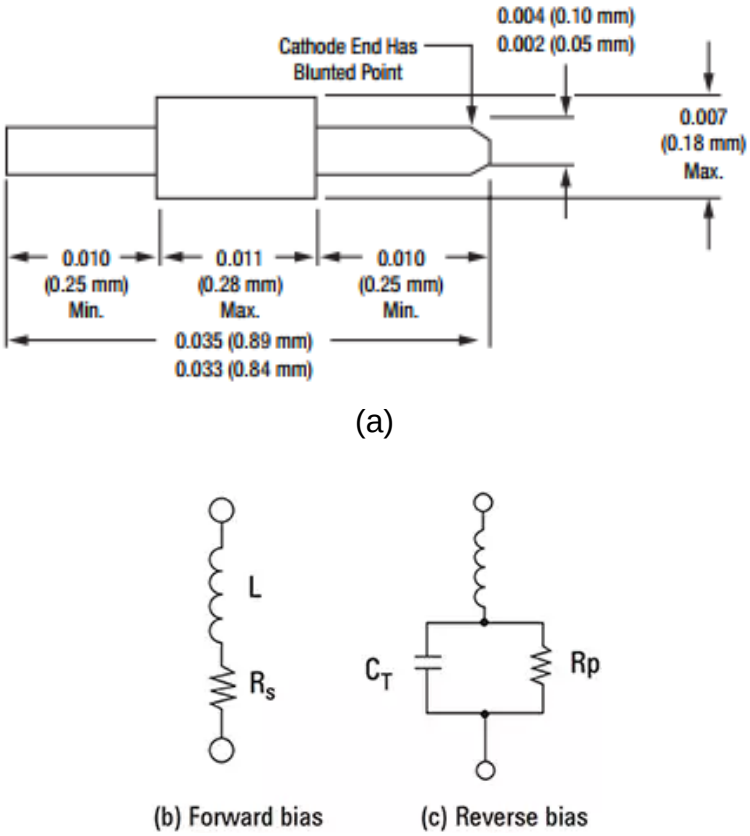

Figure 4-3 Physical dimensions (a) and equivalent circuit of the DSG9500 PIN diode in forward (ON) (b) and reverse (OFF) (c) bias condition.

Table 4-2: Parameter values of the PIN diode

Parameter	Value	Parameter	Value
L	0.5 nH	C_T	0.025 pF
R_S	4 Ω	R_P	10 Ω

4.1.2. Simulation results & analysis

The first step of the analysis of this new SIW phase shifter was to conduct a parameter study in HFSS on the effect and sensitivity of the provided phase difference and insertion loss versus the position and diameter of the metal posts. Practical fabrication considerations, such as available drill sizes and minimum gap width were used when choosing the range of values for the different parameters.

The simulated phase difference over the frequency range of interest, 26 GHz – 32 GHz, provided by an SIW phase shifter with 2 metal posts is presented in Figure 4-4 for the 4 different states of the circuit. The phase shift obtained is $32^0 \pm 5^0$, $52^0 \pm 8^0$ and $85^0 \pm 10^0$ for the 10, 01 and 11 states, relative to the 00 state. These values can be increased or decreased by adjusting the positions of the metal posts.

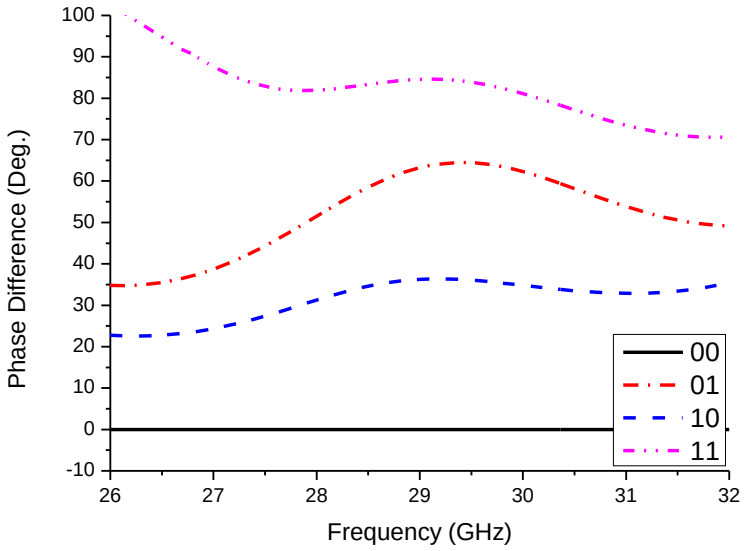

Figure 4-4 Phase difference obtained with 2 metal posts.

It was found that moving the two posts closer to the centre of the SIW increases the phase shift due to the increased perturbation of the E-field. The results from a parametric analysis of the effect of the *y* and *x* position of the metal posts on the provided phase difference is presented in Figure 4-5 and Figure 4-6, respectively. It should be noted that the proposed circuit is capable of providing more than 90^0 phase shift while only requiring 2 PIN diodes. However, this increase in phase shift provided is at the expense of increased insertion loss. The overall phase shift can also be increased by connecting two or more of these circuits in a cascade fashion.

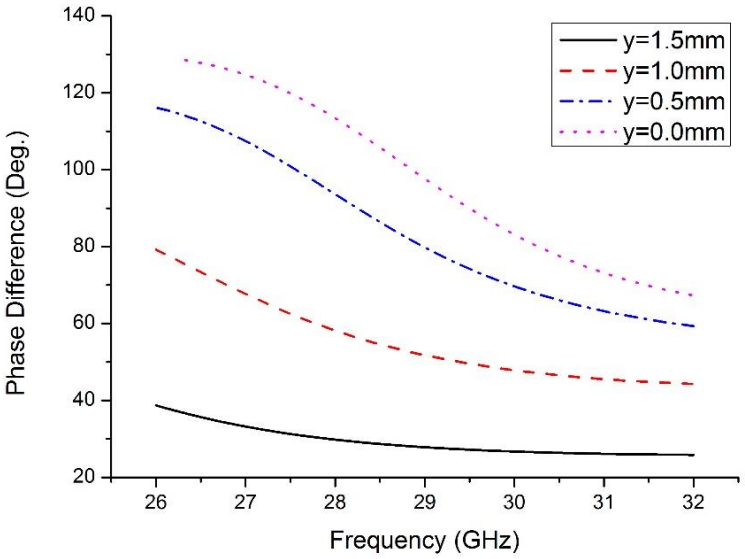

Figure 4-5 Phase response of SIW phase shifter with 2 metal posts for different values of y when x=1.5mm. Difference shown between the 00 and 11 states.

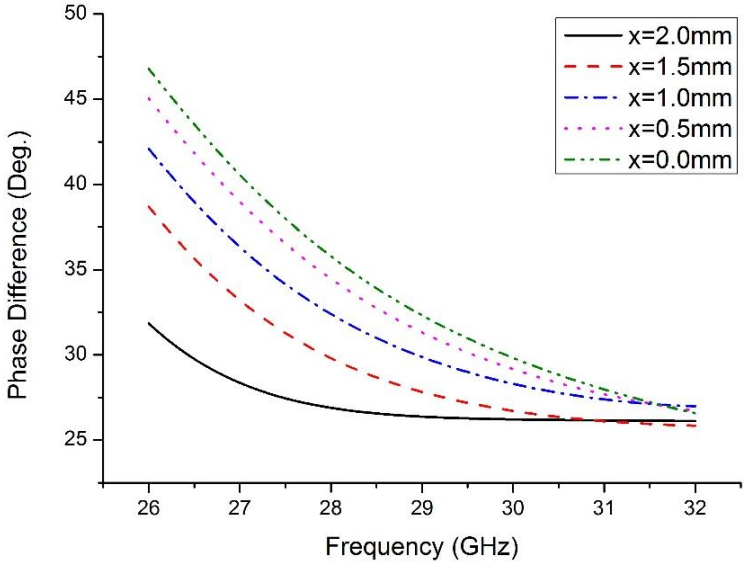

Figure 4-6 Phase response of SIW phase shifter with 2 metal posts for different values of x when y=1.5mm. Difference shown between the 00 and 11 states.

The simulated S-parameters of the SIW phase shifter with 2 metal posts are shown in Figure 4-7 and Figure 4-8 . The circuits exhibit a return loss of more than 6 dB and an insertion loss of less than 3.5 dB from 26 GHz to 32 GHz. Both of these are for a circuit with y = 1.5 mm and x = 1.5 mm, and metal post diameter d = 0.5 mm.

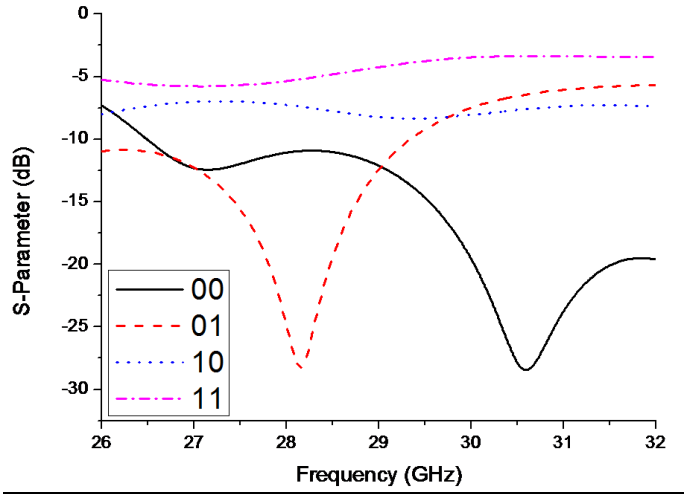

Figure 4-7 Simulated return loss for SIW phase shifter with 2 metal posts.

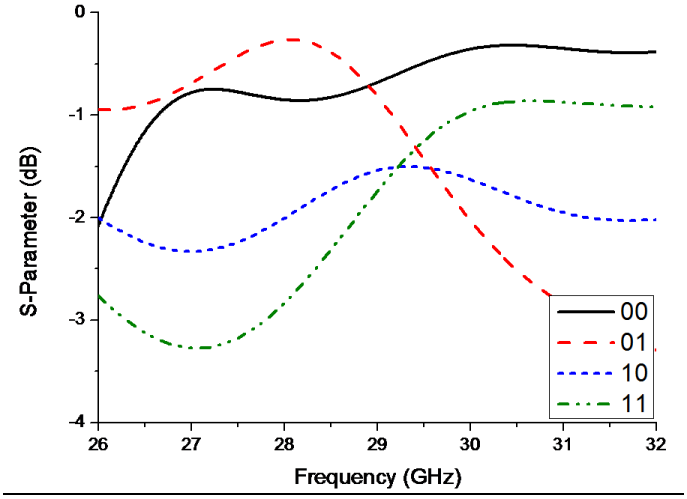

Figure 4-8 Simulated insertion loss of SIW phase shifter with 2 metal posts.

The simulated phase difference provided by an SIW phase shifter with 4 metal posts is given in Figure 4-9. The largest phase shift obtained is approximately $100^0 \pm 5^0$ in the 26 GHz – 32 GHz range, when all 4 conductive posts are active. As can be seen in Figure 4-9, for certain combinations the values of phase difference are similar, which is due to the symmetric structure of the circuit. Simulated S-parameters for this SIW phase shifter with 4 metal posts, for different states of the reconfigurable conductive posts, are shown in Figure 4-10. It is evident that the insertion loss is less than 3.5 dB from 26 GHz to 32 GHz.

The presented results for a 4 post phase shifter are for a variant with the same values for *y* and *x* as the 2 post one. Increasing the number of metal posts, while keeping the other parameters the same, has the effect of increasing the maximum phase difference obtainable, while having a negligible impact on the insertion and return loss performance.

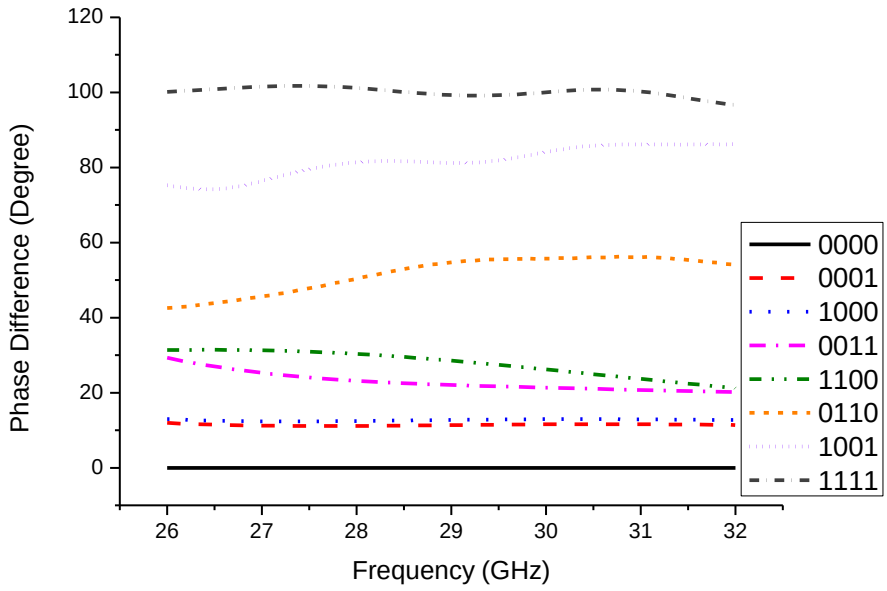

Figure 4-9 Phase difference obtained with a phase shifter with 4 metal posts.

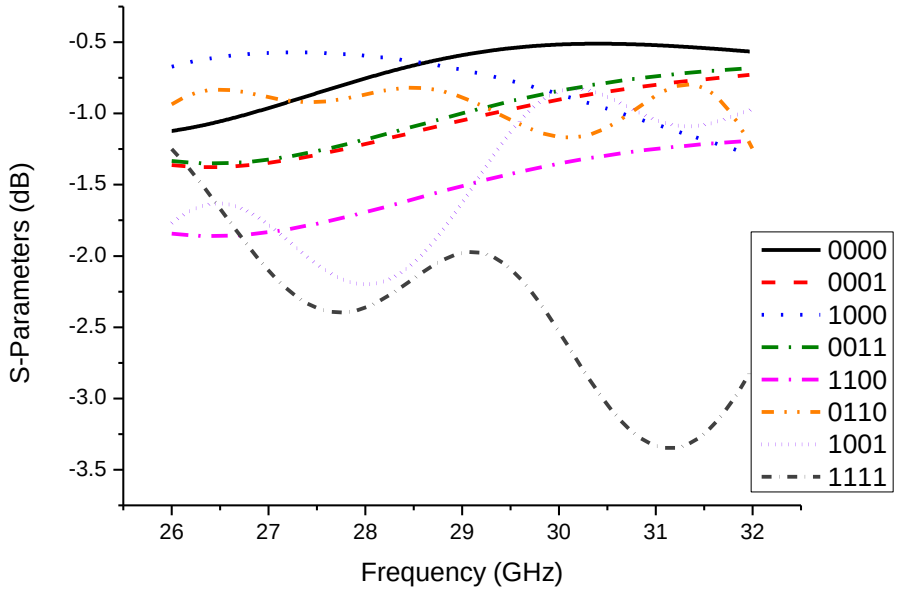

Figure 4-10 Simulated insertion loss of SIW phase shifter with 4 metal posts.

4.1.3. Measured results & fabrication

To quickly validate the proposed approach, circuits in which the proposed PIN diodes are selectively replaced with copper strips were fabricated on a 0.787 mm thick RT/Duroid 5880, using the in-house circuit fabrication facility at the University of Leeds. The circuits fabricated correspond to the 4 different configurations (00, 01, 10, 11) of a 2-bit SIW phase shifter as well as selected configurations (0000, 0001, 0011, 1000, 1100, 0110, 1001, 1111) of a 4-bit SIW phase shifter. Photographs of these circuits, together with the measurement setup, are shown in Figure 4-11(a), (b) and (c), respectively. Precision field-replaceable 2.4 mm Southwest Microwave connectors were used to connect the circuits to the coaxial-based measurement equipment.

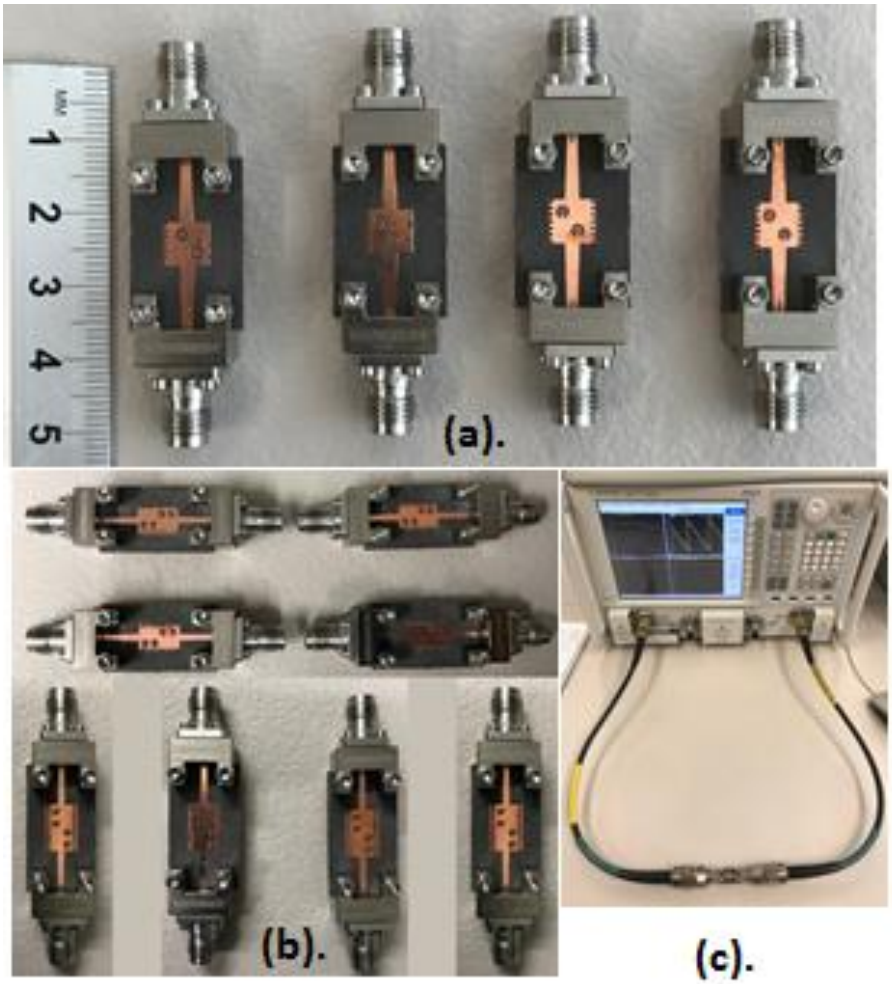

Figure 4-11 Fabricated prototypes (a) 2-bit SIW phase shifters (b) 4-bit SIW phase shifters and (c) Measurement setup.

The circuits were measured using a Keysight PNA-X N5247A with a full 2-port SOLT calibration, over the frequency range of interest, i.e. 26 GHz – 32 GHz, with 601 frequency points.

A comparison between the measured and simulated phase difference are presented in Figure 4-12 and Figure 4-13 for the 2-bit and 4-bit SIW phase shifter respectively. Overall, there is good agreement between simulated

and measured results. The differences are considered due to the effect of the 2.4 mm connectors used for measurements, which were not soldered on the circuits and coaxial-to-microstrip transition; as well as errors from fabrication tolerances which can't be neglected at mmW frequencies.

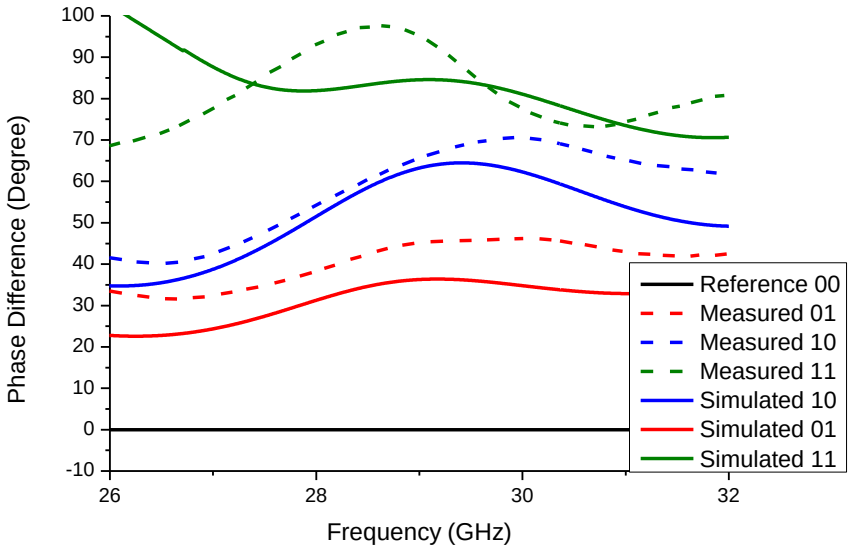

Figure 4-12 Simulated and measured phase difference of a 2-bit SIW phase shifter.

A similar comparison for the insertion loss of the proposed circuits are given in Figure 4-14 and Figure 4-15, where similar observations can be made. There is a qualitative agreement between measurements and simulations, with the difference attributed to the coaxial to microstrip transition.

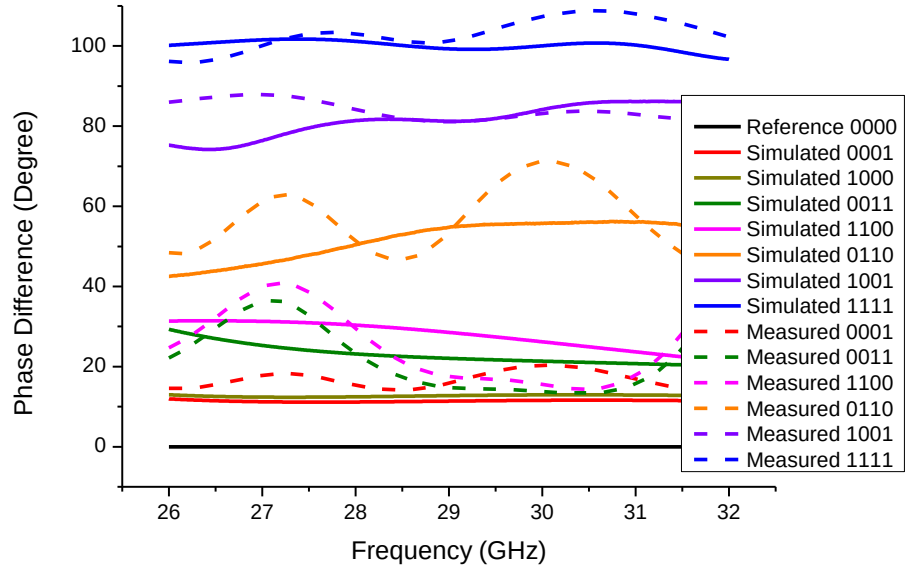

Figure 4-13 Simulated and measured phase difference of a 4-bit SIW phase shifter.

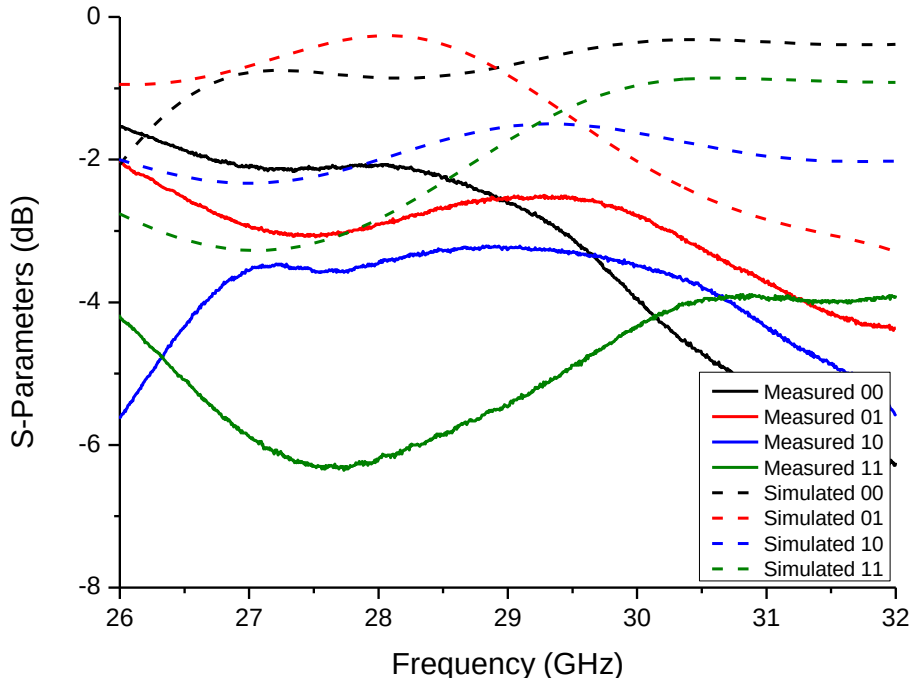

Figure 4-14 Simulated and measured insertion loss of 2-bit SIW phase shifter.

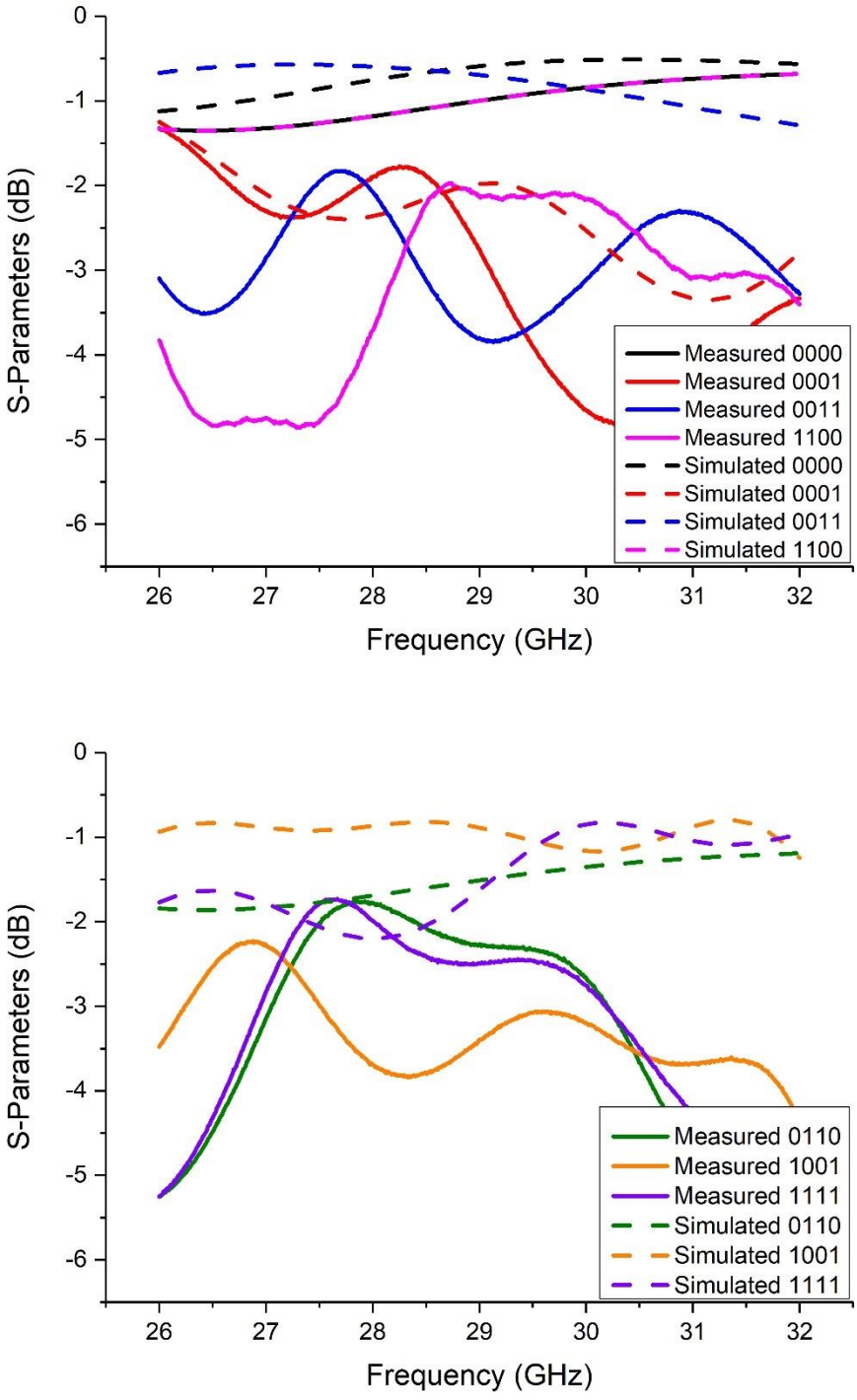

Figure 4-15 Simulated and measured insertion loss of 4-bit SIW phase shifter for different states of metal posts.

4.2. 3D Printed Hollow Integrated Waveguide

There are two major types of SIWs. One is the dielectric filled SIWs and the other one is the hollow substrate integrated waveguides. Many dielectric filled SIW based microwave and millimetre-wave components have been reported in the literature during the last decade [101, 116-118]. Dielectric filled SIWs are planar but difficult to conform due to substrate materials, placement of via holes and manufacturing limitations. In [116], SIW was presented using flexible dielectric material and the vertical walls of SIW consists of very thin and closely spaced metallic wires. In this way the leakage loss has been reduced but the insertion loss was increased up to 1.8 dB due to lossy flexible dielectric substrate. In another research work [103], a transition between CPW and SIW was proposed for microwave and millimetre-wave circuit designs. Author claimed an insertion loss of better than 0.4 dB over the entire Ku band. It was fabricated with PCB process using metallic via holes around the CPW transition as well. One of the basic reasons to move from dielectric filled SIWs to hollow SIW is the dielectric loss of the substrate which can be minimized only up to some extent due to dielectric properties of materials. HIW have no dielectric loss due to air filled structure. Air filled SIWs have low transmission and reflection losses, but they have complex and high cost fabrication process i.e. low-temperature co-fired ceramic (LTCC). However, there are only a handful

of reports on hollow waveguides. Design and analysis of a HIW is presented in [105]. In this research work author claims an average insertion loss of 0.009 dB / mm. Despite promising results for the average insertion loss per mm, the reported HIW has a complex and costly fabrication process of using LTCC. In another research work [119], an HIW was design and implemented in a multilayer structure using standard PCB process for U-band. A dielectric filled SIW to hollow SIW transition was used to feed the HIW structure which increases the overall insertion loss of HSIW from 0.122±0.122 dB/cm to 0.4±0.13 dB/cm. Similarly in [120], an air-filled substrate integrated waveguide made up of multilayer structure was proposed for millimetre-wave applications. HSIW is sandwiched between the top and bottom layers of lossy FR4 dielectric material and was manufactured by using PCB technique. Dielectric filled SIW to HIW transition similar to [5] was used to insert the signal in HIW. It had a measured insertion loss of 0.6±0.2 dB/cm over frequency range of 27 to 40 GHz.

In this research work, a novel design and fabrication method for hollow integrated waveguide based on low cost 3D printing technology is presented. The proposed HIW is compact, low cost and low loss with an operational bandwidth of 16 GHz (24 GHz – 40 GHz), covering the main 5G candidate frequency bands, and has an excellent propagation loss performance of less than 0.15 dB/cm over entire frequency band which

is much comparable to other published designs of hollow waveguides but with very simple design approach and very low cost fabrication based on 3D printing technology as compared to designs presented in open literature.

4.2.1. Design and manufacturing

The proposed hollow integrated waveguide consists of low-cost 3D printed inner structure having hollow waveguide channel at the middle and go through series of holes at both sides of hollow channel for side walls of HIW as shown in Figure 4-16. Acrylonitrile butadiene styrene (ABS) dielectric material with dielectric constant $\varepsilon_r = 2.7$ and loss tangent 0.01 was used to fabricate the inner structure using a commercially available 3D printer Object1000 [121]. The reason for using ABS here is because of 3D printer used for the fabrication of HIW is different from the one used for the fabrication of ILAs and this printer uses ABS instead of PLA. The design and dimensions of inner structure are the most crucial part of HIW design because all other components of full HIW prototype are dependent on the design of this 3D printed structure. The width of hollow waveguide channel, the diameter of holes and the spacing between the two adjacent holes will determine the cut-off frequency and operational bandwidth of HIW. The initial dimensions of the hollow waveguide channel were calculated using the conventional relations for rectangular waveguide provided in [120] for TE10 mode of

propagation. For air $\varepsilon_r = 1$ and $\mu_r = 1$ and thickness of HIW is *h* = 0.5 mm. The TE10 cut-off frequency is calculated using Equation (2-1) to be 24 GHz.

According to below mentioned conditions the value of *d* and *p* should be less than 0.35 mm and 0.69 mm, respectively at 100 GHz for a substrate material having $\varepsilon_r = 3.0$. Those feature sizes are difficult to fabricate using conventional machining.

$$d < \frac{\lambda_g}{5} \qquad (4\text{-}1)$$

$$p < 2d \qquad (4\text{-}2)$$

Where *d* is the diameter of holes and *p* is the distance between two adjacent holes, λ_g is the wavelength inside the dielectric medium.

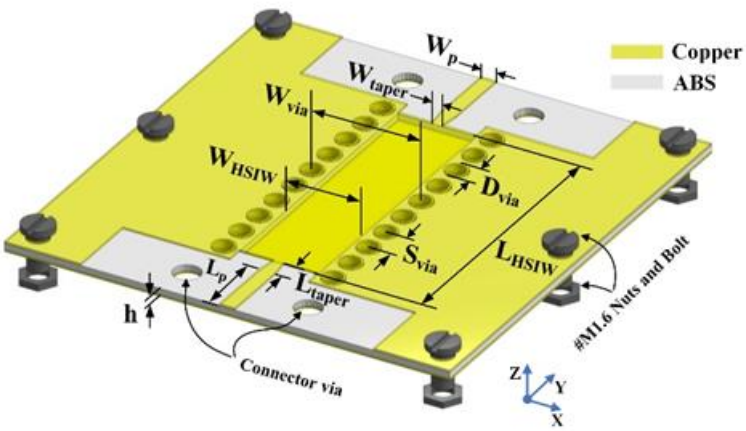

Figure 4-16 General layout of proposed 3D printed HIW

After 3D printed the inner structure of HIW the next step was to cover the top and bottom sides of inner structure with copper sheets as shown in Figure 4-16. The copper sheets were processed by using waterjet-guided laser cutter. Copper rivets were used instead of electroplated via holes to make the side walls of HIW according to conditions mentioned in equation (4-1) and (4-2). Rivets are placed in the holes and punched, alternating the side to be punched so that the rivet heads would not collide with another. A tapered microstrip to SIW transition line was used to excite the HIW. The complete prototype of HIW was fastened with the nut and bolt. Complete assembled fabricated prototypes of proposed structures are shown in Figure 4-17 and the individual components of the prototype are shown in Figure 4-18. Final values of all the parameters are summarized in Table 4-3.

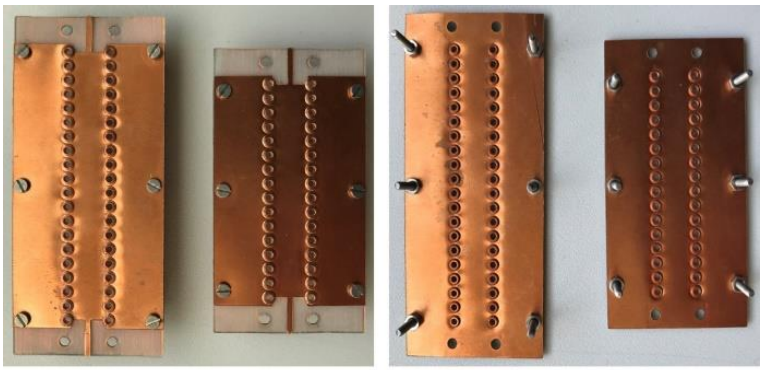

Figure 4-17 Assembled 3D printed hollow waveguide prototypes a) Top view, b) Bottom view

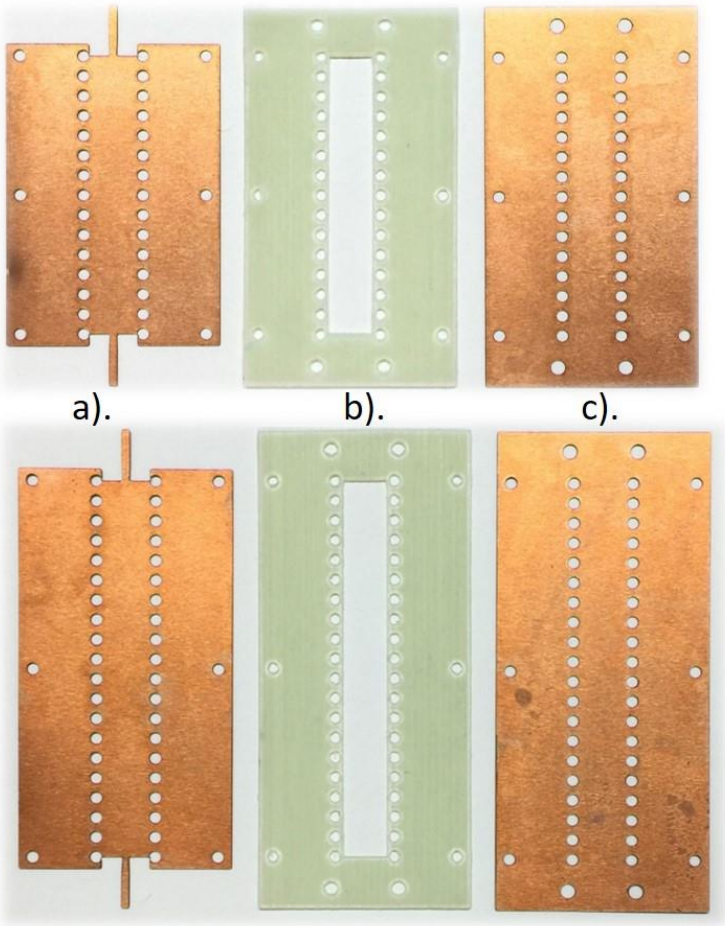

Figure 4-18 Fabricated prototypes of proposed HSIWs a). Top copper sheet, b). Inner 3D printed structure c). Bottom copper sheet

Table 4-3 Final values of design parameters

Parameter	Description	Dimension (mm)
W_p	Width of microstrip line	1.2
W_{taper}	Width of taper transition from Microstrip line to HSIW	0.8
W_{via}	Width distance between via	8.6
W_{HSIW}	Width of Hollow-SIW	6.2
L_p	Length of microstrip line	5.5
L_{taper}	Length of microstrip line	1.5
L_{HSIW}	Length of Hollow-SIW	39, 42
D_{via}	Diameter of via (rivets)	1.6
S_{via}	Distance between two via	2.4
h	Substrate height	0.5

4.2.2. Measured results and discussion

The proposed 3D printed HIWs were fabricated and measured using in-house facilities at the University of Leeds. Several samples with different

lengths were designed and fabricated using proposed design approach and the measured results are presented here.

The S-parameters of fabricated circuits were measured in laboratory conditions as shown in Figure 4-19 using a Keysight N5247A PNA-X with 2-port Short, Open, Load and Thru (SOLT) calibration, bringing the S-parameter reference plane to the end of the coaxial cables over the frequency range of interest, i.e. 24 GHz – 40 GHz, with 1001 frequency points. A comparison between the measured and simulated S-parameters of HIW having different lengths are presented in Figure 4-20. For all prototypes the values of measured insertion and reflection losses are less than 2 dB and -10 dB respectively.

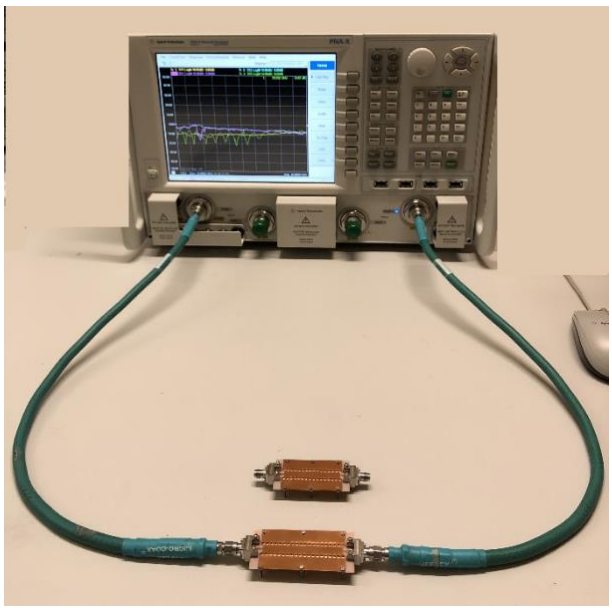

Figure 4-19 Measurement setup for HIW prototypes

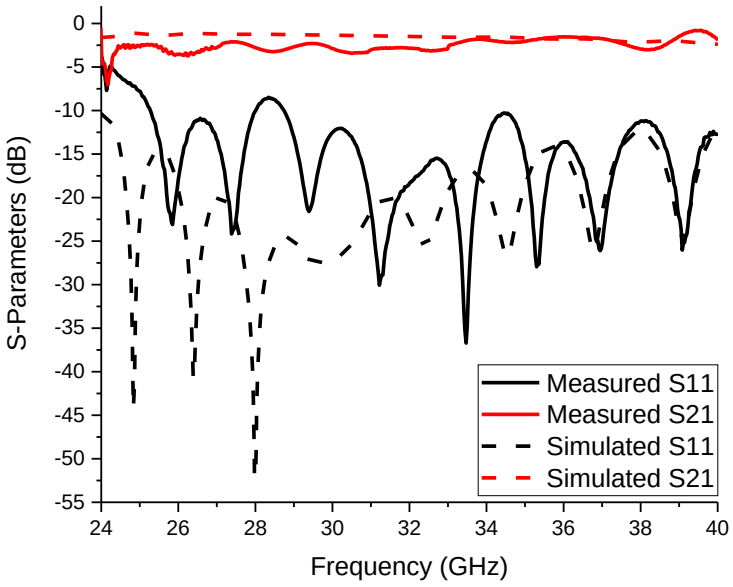

(a)

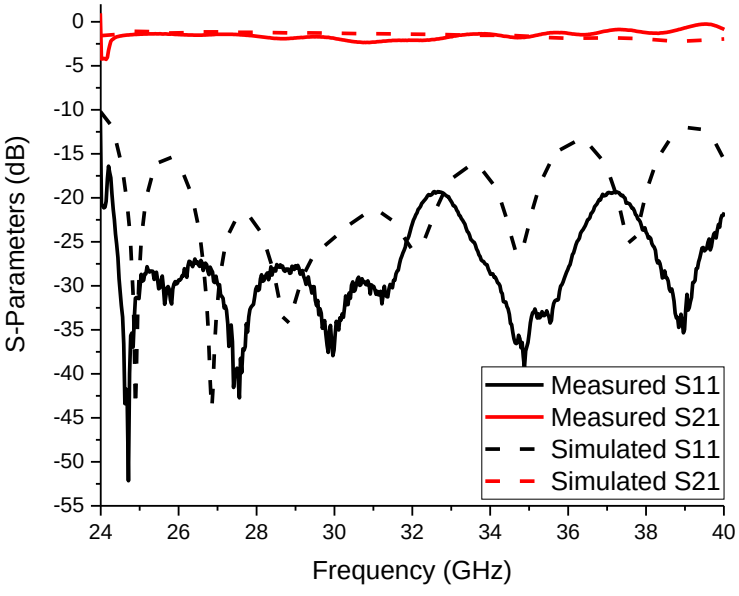

(b)

Figure 4-20 Simulated and measured S-parameters of HIWs with different lengths a). 42 mm b). 53 mm

A multimode calibration method proposed in [122] is used to analyse and determine the propagation constant of the HIW. The multimode calibration method is basically a multiline method in which the propagation constant can be calculated by using the uncalibrated S-parameter measurements of at least two transmission lines. Simulated and measured attenuation and phase constant of proposed structures are shown in Figure 4-21. The proposed structures have an average propagation loss of less than 0.15 dB/cm which is acceptable and very much comparable to some other proposed hollow waveguides in open literature with complex and costly manufacturing process [18, 19]. Overall, there is good agreement between simulated and measured results. The differences are considered due to the effect of the microstrip transition and the 2.4 mm connectors, which were not de-embedded on the circuits; as well as errors from fabrication tolerances. For all the fabricated designs the simulated as well as measured reflection coefficients are less than -10 dB for almost the entire band of interest. There is a qualitative agreement between simulated and measured insertion loss, with the difference attributed to the microstrip to HIW transition.

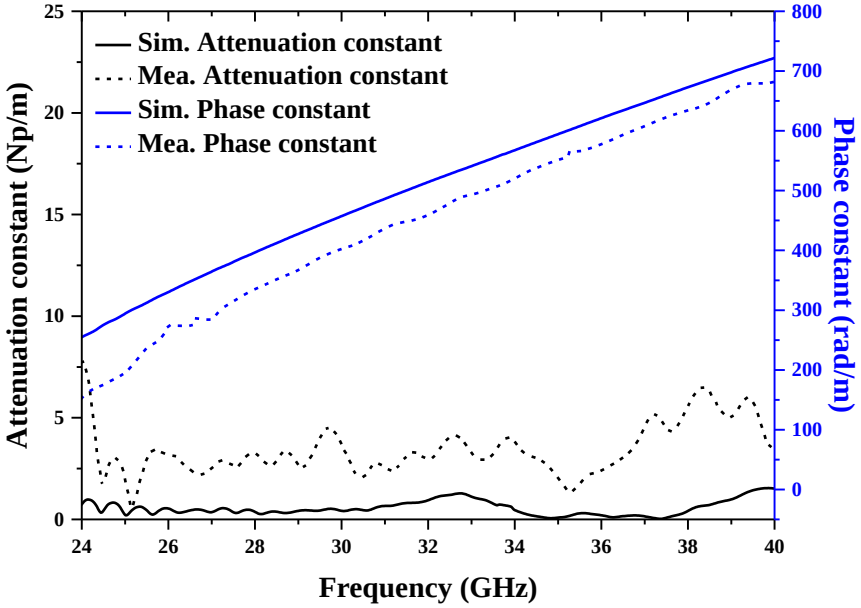

Figure 4-21 Simulated and measured attenuation and phase constant of proposed HIW

In [104], the author proposed a simplified parameter q to determine the effect of dielectric material portion a_1 inside the HIW to characterize a RWG as shown in Figure 4-22. The value of q can be calculated from equation (4-3).

$$q = {2a_1\sqrt{\varepsilon_r}}/{W_{HIW}} \qquad (4\text{-}3)$$

According to equation (4-3), if the value of q lower or equal to 0.35 that proves that the dielectric portion will not have that much effect on the cut-off frequency and the HIW will behave like an air-filled hollow rectangular waveguide. So by using the same criteria as used in [104] the value of q for our proposed HIW is 0.187 which is much lower than 0.35, which clearly shows that our proposed design approach is better

in terms of effects of inside dielectric portion on the electric fields propagation of HIW as shown in Figure 4-23.

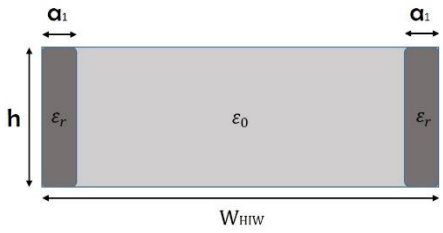

Figure 4-22 Cross sectional view of proposed HIW

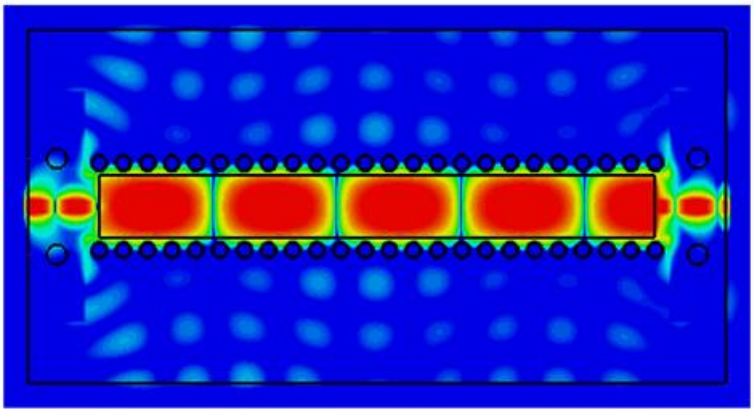

Figure 4-23 E-field distribution inside the proposed HIW

Figure 4-24 shows a comparative study based on the effects of dielectric portion inside the hollow waveguide on the attenuation constant. It clearly shows that the amount of attenuation constant increases with the increase of values of *q*. Similarly Figure 4-25 presents the effects of loss tangent of the inner 3D printed structure on the attenuation constant of HIW.

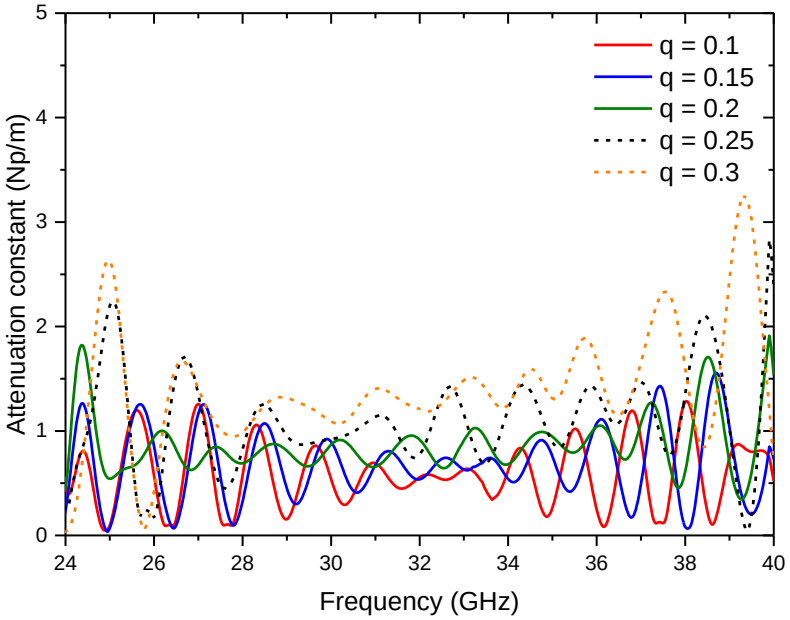

Figure 4-24 Effects of *q* on the value of attenuation constant of proposed HIW

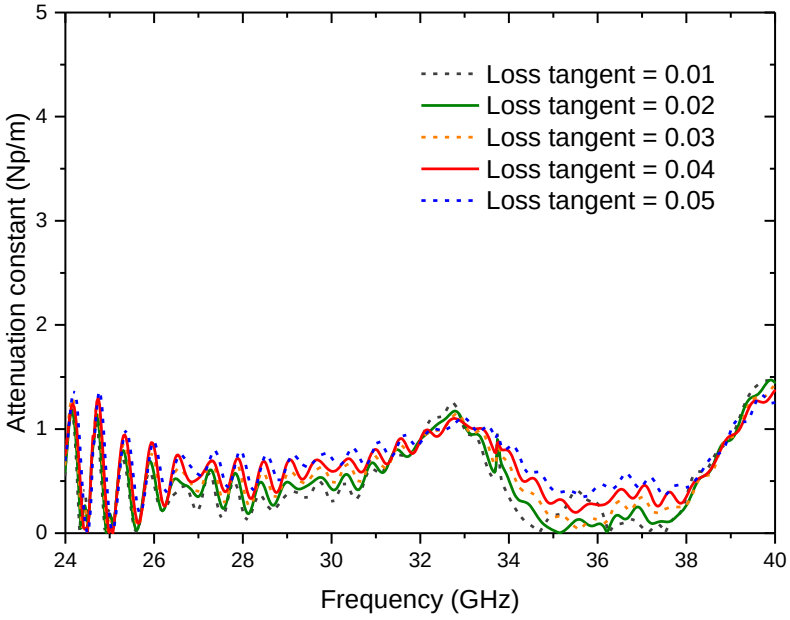

Figure 4-25 Effects of loss tangent of 3D printed material on the attenuation constant of proposed structures

Figure 4-26 compares the performance of proposed 3D printed hollow integrated waveguide with the SIW and the conventional metallic rectangular waveguide. It can be seen that the value of attenuation constant of proposed HIW is very low as compared to SIW and close to rectangular waveguide. A comparison on several key metrics with previously published results for HIW at similar frequency ranges is presented in Table 4-4, showing that the proposed HSIW compare favourably with those produced using more expensive and complex fabrication methods.

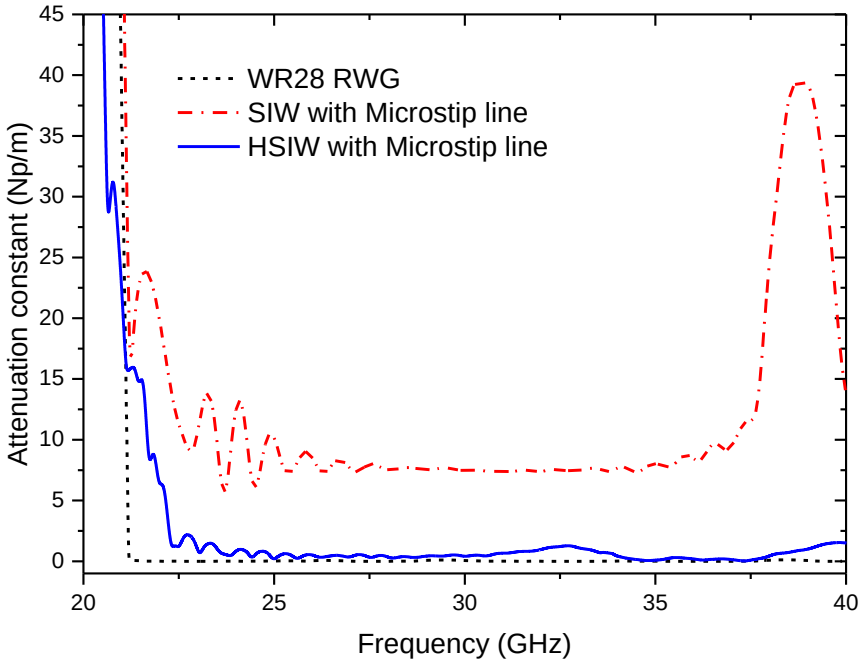

Figure 4-26 Comparison of attenuation constant of proposed HW with the metallic rectangular waveguide (RWG) and substrate integrated waveguide (SIW).

Table 4-4 Comparison of proposed work with open literature

	[103]	**[123]**	**[119]**	**[105]**	**Proposed**
Design method	SIW with CPW transition	SIW with microstrip transition	Air-filled SIW	HSIW	HIW
Substrate material	Roger 6002	Rogers 5880	Roger 6002	LTCC	ABS
Fabrication process	PCB	PCB	PCB	LTCC	3D printed
Fabrication procedure	Simple	Simple	Simple	Difficult	Simple
Attenuation	~ 0.25 dB/cm at 30 GHz	~ 0.3 dB/cm at 30 GHz	0.3 dB/cm at 30 GHz	0.09 dB/cm	0.15 dB/cm at 30 GHz
Possible to Design Conformal	No	No	No	No	Yes
Cost	Medium	Medium	Medium	Very High	Low

4.3. Chapter summary

In this chapter a novel approach to the design and implementation of a broadband SIW phase shifter and a 3D printed hollow waveguide structure has been presented. To demonstrate the proposed concept, a phase shifter operating over the main 5G candidate frequency bands (26 GHz – 32 GHz) has been designed and optimized using ANSYS HFSS. The proposed SIW phase shifters and hollow integrated waveguide structures are compact, broadband and easy to fabricate and integrate with other planar circuits. Measurement results from fabricated prototypes show good agreement with simulation results, confirming that the proposed SIW phase shifter is an attractive candidate for use in beamforming and beam steering modules in phased array antennas for 5G communication. The proposed low loss HIW could be an alternative to conventional bulky metallic air filled waveguides.

Chapter 5. Millimetre-Waves Wireless Power Transfer

The field of Wireless Power Transfer (WPT) has attracted considerable attention due to providing wireless power charging and battery-free solutions in many emerging applications in different domains such as infrastructure robotics, Internet of Things (IoT) devices, and sensor networks [5, 124]. A lot of research has already been done for WPT at sub-6 GHz frequency bands, and now effort is shifted towards millimetre-wave frequency bands [125-127]. The two major requirements of an efficient wireless power transfer system are a high-gain directional antenna and a rectifier circuit with high RF-DC conversion efficiency [124]. A rectenna is a combination of the antenna and rectifier and is considered the most critical component of a WPT system [5, 127]. The overall performance of a WPT system directly depends on the efficiency of the rectenna [128]. An overview block diagram of such a system is shown in Figure 5-1.

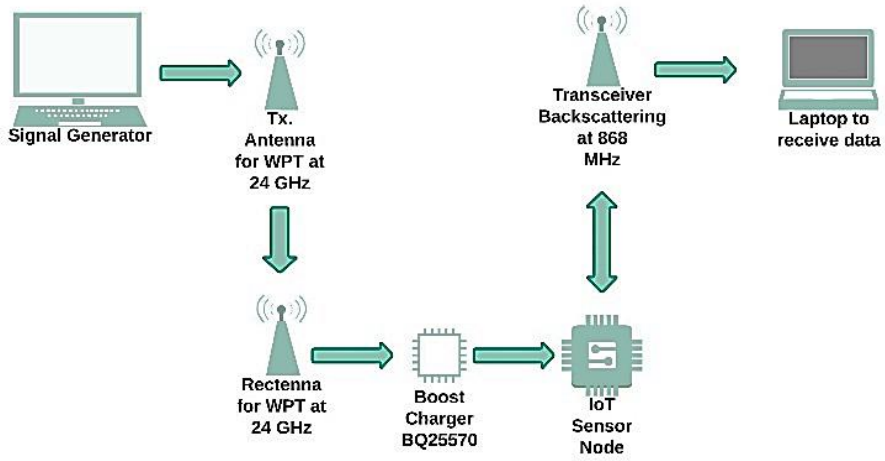

Figure 5-1 System block diagram of wireless power transfer to IoT sensor node for backscattering communications

5.1. Millimetre-waves WPT to IoT sensor nodes

IoT technology is expected to have a lot of practical applications in many industries, including agriculture, construction, manufacturing, healthcare, energy and transportation [20, 21]. However, batteries present in these IoT devices have many drawbacks in terms of size, weight, and cost, in addition to needing replacement once depleted. This in turn can make the installation of battery-powered IoT devices in remote and hard-to-reach places unfeasible. Hence the battery life of an IoT device is one of the challenges that need to be addressed. The solution proposed in this research work is to use a small energy storage element, e.g. a super-capacitor, which can be charged through mmW wireless power transfer. The motivation behind this research work is to replace the need for a battery in sensor nodes deployed in places with limited accessibility.

One of the main benefits of using millimetre-waves for WPT is the reduction in the physical space occupied by the rectennas while retaining the same output power density. Furthermore, the beam directivity can also be enhanced by using mmW which is better for far field WPT [5].

Various rectifier designs have been proposed in literature. Jo Bito et al. [129] demonstrated a flexible, inkjet printed mmW rectenna at 24 GHz for wearable IoT applications. The author gets 2.5V dc voltage with an input power of 18 dBm at 24 GHz. Daskalakis et al. [130] developed a 24 GHz rectenna on paper substrate with RF-DC conversion efficiency of 32.5% at 15 dBm input power for RFID applications. Naoki and Ken [131] designed a rectifier circuit which has a RF-DC conversion efficiency of 47.9% with input

power of 23.22 dBm using 16QAM modulated signal for fixed access wireless applications at 24 GHz. Laden et al. [128] presented the design and implementation of rectennas using SIW technology at 24 GHz. Their results show that the rectification efficiency was 24% for an input power density of 10 mW/cm^2. Colado et al. [132] proposed an SIW based rectenna at 24 GHz having a maximum RF-DC conversion efficiency of 15% at 8 dBm of input power. In [133], a 24 GHz rectenna was proposed for fixed wireless access applications with an RF-DC conversion efficiency of 43.6% at 27 dBm input power. In another research work for a similar application, a 4x4 microstrip patch array (MPA) for energy harvesting at mmW frequencies was proposed [134]. It has an RF-DC conversion efficiency of 67% and a maximum voltage of 2.18 V at 35.7 GHz at a distance of 8 mm from a horn antenna at 35 GHz.

In most of the above-mentioned research works the authors only presented the simulated RF-DC conversion efficiencies, which are always much higher than the actual measured efficiencies as summarized in Table 5-1. The experimental RF-DC conversion efficiency of rectenna are extraordinarily lowered than the simulated efficiency due to many factors such as the gain of antennas, input RF power of rectifiers, diode impedance and the optimum value of load resistance deviate from optimal values [5].

In this contribution a complete wireless power transfer system, operating at 24 GHz for the purposes of charging backscattering IoT sensor nodes, is experimentally demonstrated. RF backscatter-based IoT sensor nodes are well suited for structural health monitoring applications such as crack detection on bridges where strain gauges or vibration sensors can provide

data to a mobile station. A drone can be used for mounting the backscattering reader as well as RF power transmitter for collecting the data from the sensor nodes. Design, simulation and implementation of different types of rectifier circuits (shunt, series and voltage doubler) and rectifying diodes (MA4E2054A and SMS7621) are presented, as well as complementary antenna arrays. Initially the arrays and the rectifier circuits are individually designed, optimized, fabricated and measured. To form a complete rectenna layout the antenna array and rectifier are integrated into one board. A comprehensive performance comparison of different rectifier topologies follows, with a final demonstration of an IoT sensor node fully powered by the rectenna completing this research work.

Table 5-1 Rectennas performance in open literature

Ref.	Simulated Efficiency (%)	Measured Efficiency (%)	Output DC (V)	Frequency (GHz)	Input Power (dBm)	Distance (cm)
[128]		24	0.6	24	18	-
[129]			0.286	24	18	15
[130]	35.25		-	24	15	-
[131]	43.6		-	24	27	-
[132]		16.2	-	24	8	-
[135]	40		-	24	35	-
[134]	67		2.18	35	7	0.8

5.1.1. Rectifier Designs & Simulation Results

Microwave and millimetre-wave rectifiers can be implemented in various configurations, however, the series and shunt topologies are the most common and to increase the DC output voltage, one can also use a voltage doubler configuration [136].

In this research work these three different configurations (shunt, series and voltage doubler) have been evaluated at 24 GHz by using two different rectifying diodes (MA4E2054A and SMS7621). Following this evaluation, the optimum design was chosen to demonstrate a wireless power transfer system. The main figure of merit for the performance of rectifiers is the RF-DC conversion efficiency given as:

$$\eta = \frac{P_{out}}{P_{in}} \qquad (5\text{-}1)$$

Where P_{out} is the DC output power and P_{in} is the input RF power. Circuit parameters such as DC load resistance, smoothing and decoupling capacitors, source impedance matching networks and higher-order harmonic suppression radial stubs were optimized to obtain the maximum RF-DC conversion efficiency using Keysight Advance Design System (ADS). The general layout of a rectifier consists of a source impedance matching network to match the signal source to the input impedance of the circuit, a non-linear element, e.g. a Schottky diode, and a low-pass filter with a load resistance.

5.1.1.1. Rectifying diodes

Two different Schottky diodes were used in simulation model of rectifiers. First one is MACOM MA4E2054A in a SOD-323 package with a parasitic series resistance of 10.5 Ω, junction capacitance of 0.13 pF, reverse breakdown voltage of 3.0 V, and minimum forward voltage of 250 mV at 1 mA [137]. The other one is Skyworks SMS7621 in a 0201 package with a parasitic series resistance of 10.3 Ω, junction capacitance of 0.13 pF, reverse breakdown voltage of 2.0 V, and minimum forward voltage of 260 mV at 1 mA. The simulation models of these diodes and their packages are shown in Figure 5-2(a) and Figure 5-2(b) [138].

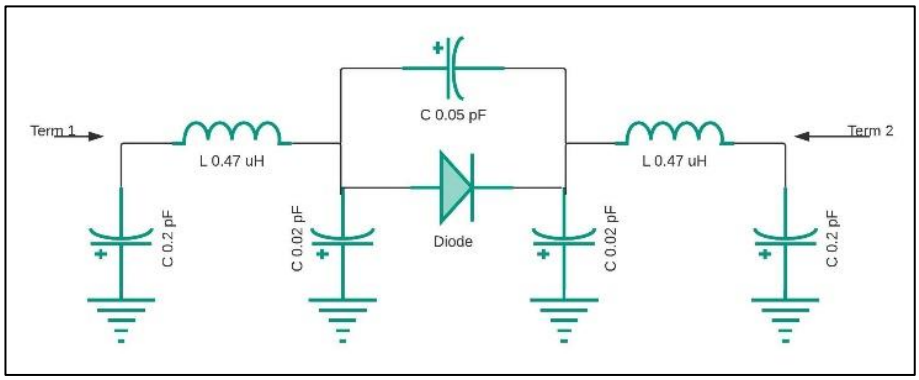

(a)

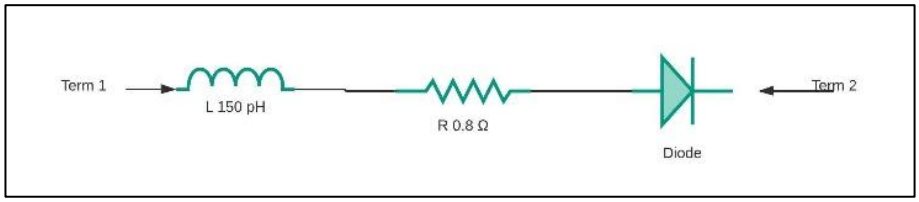

(b)

Figure 5-2 Diode package spice model a). SOD-323, b). 0201

5.1.1.2. Shunt configuration

The design of a rectifier in shunt configuration is shown in Figure 5-3. In this configuration the diode is mounted in parallel to the DC load resistance. The same circuit topology was used with the two different Schottky diodes to compare their performance in shunt configuration. Figure 5-4 shows their simulated RF to DC conversion efficiency as a function of the DC load resistance R. It can be seen that the rectifier utilising the MA4E2054A diode achieves a maximum efficiency of 46% as compared to 25% for the one with the SMS7621 diode. In both cases 200 Ω DC load resistance is the optimal one. Similarly, simulation results for rectifying efficiency for a fixed DC load but as a function of input RF power are shown in Figure 5-5(a) and Figure 5-5(b) for MA4E2054A and SMS7621, respectively.

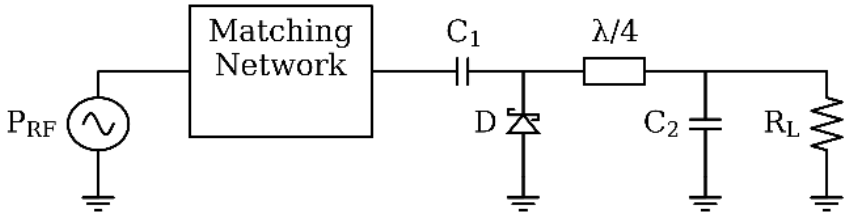

Figure 5-3 Rectifier circuit in Shunt configuration

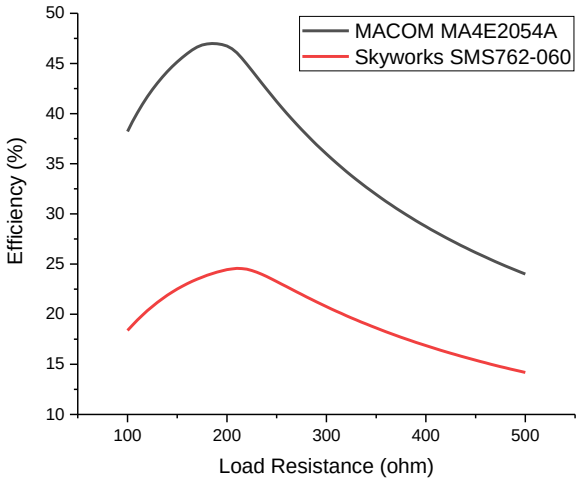

Figure 5-4 Simulated RF-DC conversion efficiency as a function of Load resistance for Pin = 14 dBm

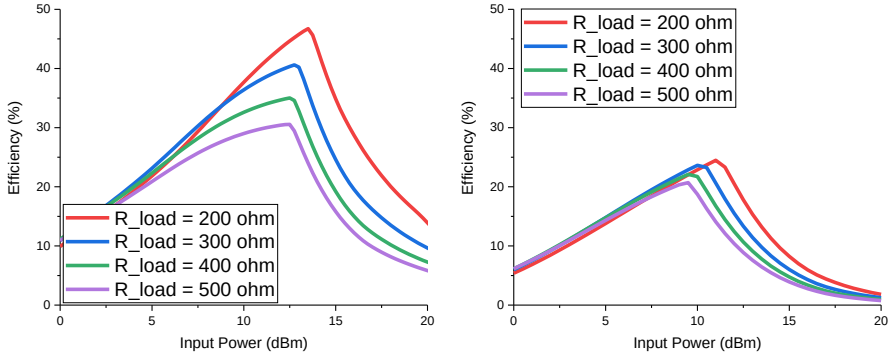

Figure 5-5 Simulated RF-DC conversion efficiency of shunt rectifiers as a function of input power a) MA4E2054A b). SMS762-060

5.1.1.3. Series configuration

Figure 5-6 shows the series rectifier design. In this topology the diode is mounted in series with the load resistance. Similarly to the shunt circuit evaluation, the performance of the two rectifier diodes was compared in terms of RF-DC conversion efficiency, with results presented in Figure 5-7 and Figure 5-8. In this case, the maximum RF-DC conversion efficiency of MA4E2054A and SMS7621 rectifier circuits was 38% and 22%, respectively, for a 200 Ω DC load resistance.

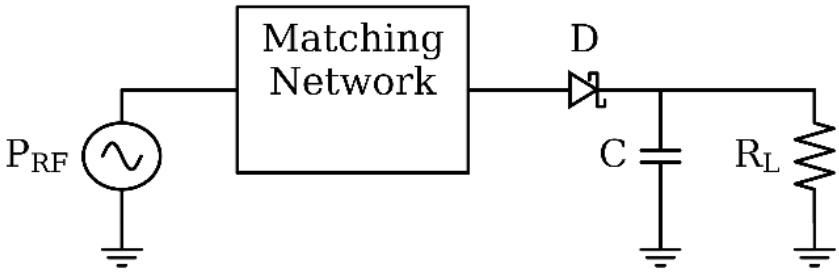

Figure 5-6 Rectifier circuit in Series configuration

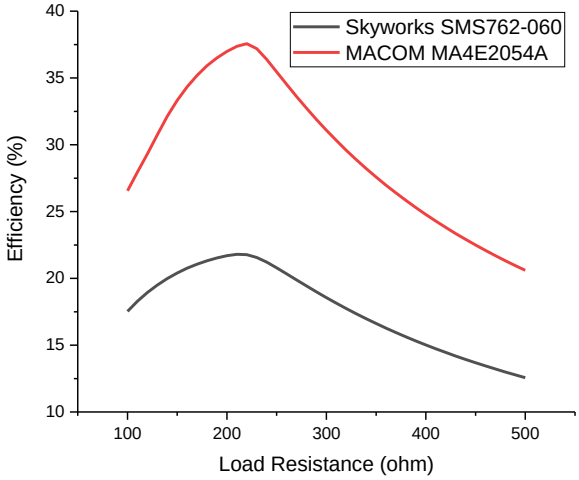

Figure 5-7 Simulated RF-DC conversion efficiency as a function of load resistance for Pin = 14 dBm

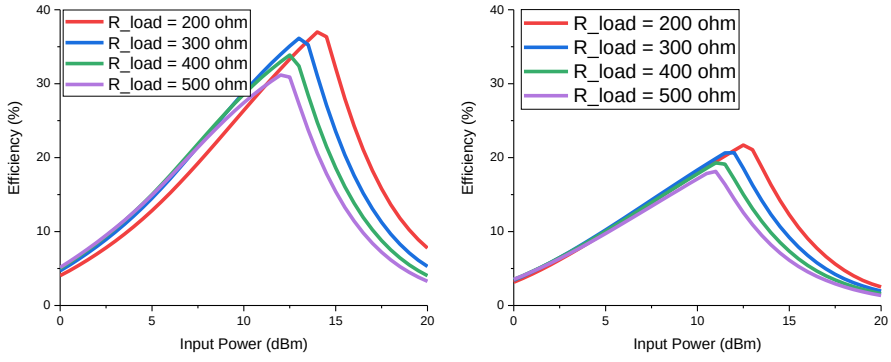

(a) (b)

Figure 5-8 Simulated RF-DC conversion efficiency of series rectifiers as a function of input power a) MA4E2054A b). SMS762-060

5.1.1.4. Voltage Doubler configuration

In this topology, illustrated in Figure 5-9, two diodes were used to enhance the output voltage and provide full-wave rectification [131]. The voltage doubler rectifier exhibits lower conversion efficiency for the same level of input RF power, when compared to the shunt and series configurations, due to more power consumption by multiple diodes. It provides a maximum rectification efficiency of 36% and 22% with a MA4E2054A and SMS7621 diode respectively for a 400 Ω DC load resistance and 12.5 dBm input power as shown in Figure 5-10 and Figure 5-11. ADS Schematic of proposed rectifier circuit in voltage doubler configuration is presented in Appendix D.

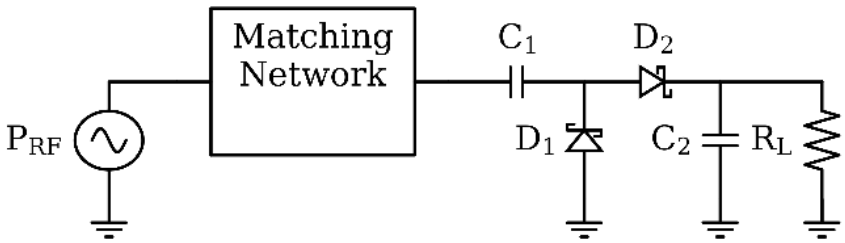

Figure 5-9 Rectifier circuit in Voltage Doubler configuration

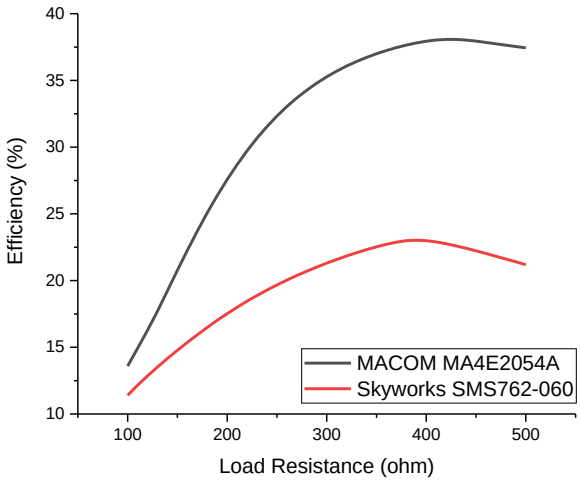

Figure 5-10 Simulated RF-DC conversion efficiency as a function of load resistance for Pin = 14 dBm

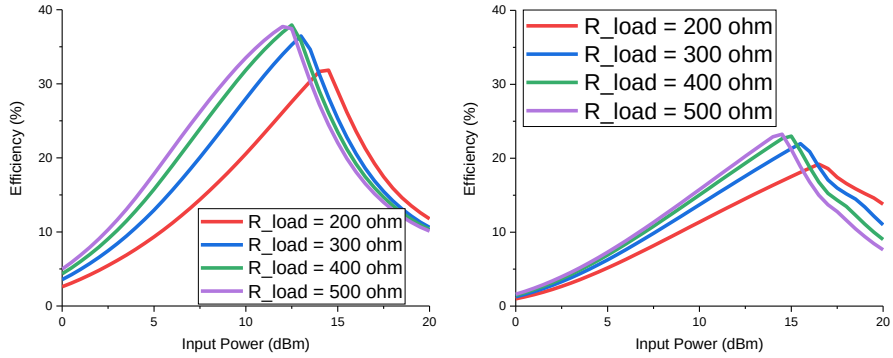

Figure 5-11 Simulated RF-DC conversion efficiency of voltage doubler rectifiers as a function of input power a) MA4E2054A b). SMS7621

5.1.2. Comparison of rectifier configurations

In this section we present a performance comparison in terms of RF-DC conversion efficiency of all the rectifier configurations using two different diode models. Figure 5-12(a) and Figure 5-12(b) shows the RF-DC conversion efficiency of proposed rectifiers as a function of load resistance and input power respectively at 24 GHz. It is evident that the rectifier in shunt configuration using a MA4E2054A Schottky diode performs best, yielding a maximum efficiency of 46% with load resistance and input power of 200 Ω and 14 dBm, respectively. The performance comparison and design parameters along with the values of all the proposed rectifiers are summarized in Table 5-2.

Table 5-2 Performance comparison of proposed rectifiers

Parameters	**Shunt**	**Series**	**Voltage Doubler**	**Diode Model**
RF-DC Conversion Efficiency (%)	46	38	36	MA4E2054A
	25	22	20	SMS7621
Output Voltage (V)	1.5	1.3	1.9	MA4E2054A
	1.1	1.05	1.4	SMS7621
Output Power (mW)	11	10.2	7.0	MA4E2054A
	5.5	5.5	3.5	SMS7621
Load Resistance (Ω)	200	200	400	MA4E2054A
	200	200	400	SMS7621

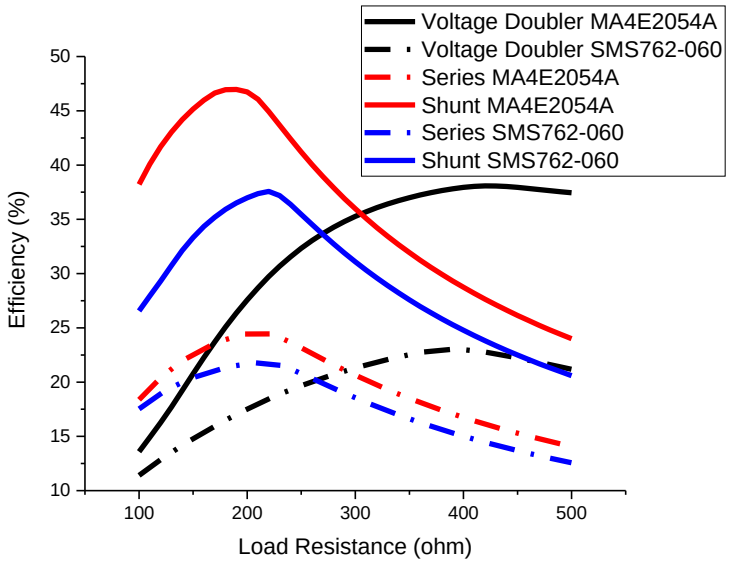

(a)

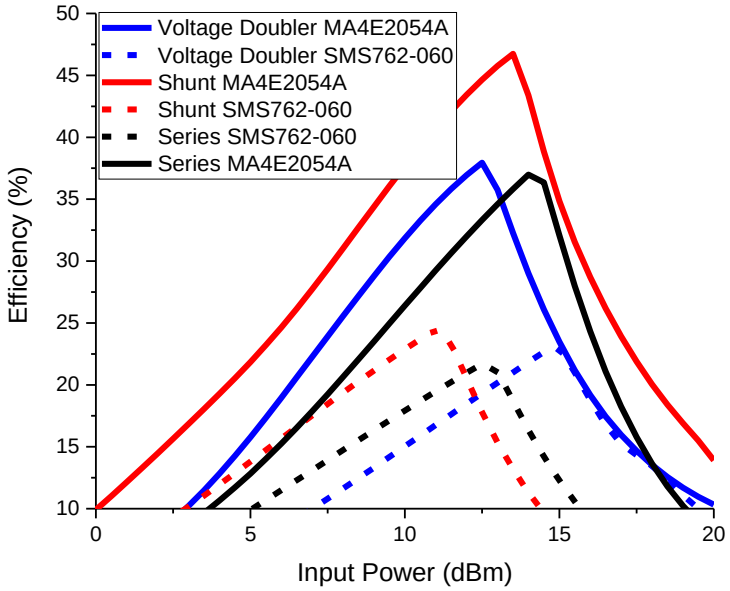

(b)

Figure 5-12 Simulated RF-DC conversion efficiency as a function of (a) load resistance, (b) input power

5.1.3. Antenna array design

A *4x4* microstrip patch antenna array has been designed to receive the RF power and transfer it to the rectifier circuit. The proposed MPA array layout with main dimensions and a fabricated sample are shown in Figure 5-13(a)

and Figure 5-13(b) respectively. A combination of corporate and series feed network was designed to connect the patches which is easy to design as compared to purely corporate feed network because of design complexity and mutual coupling effects due to the very narrow distance between the elements of MPA array at mmW frequencies. Rogers 3003 with thickness 0.51 mm, $\varepsilon_r = 3.0$ and $tan\delta = 0.001$ was used as the substrate material.

The S-parameters of the fabricated arrays were measured in laboratory conditions using a Keysight N5247A PNA-X with 1-port Short, Open, Load (SOL) calibration, bringing the S-parameter reference plane to the end of the coaxial cable, over the frequency range of interest, i.e. 22 GHz – 26 GHz, with 1001 frequency points. A comparison between the measured and simulated S-parameters and radiation pattern of the proposed MPA array are presented in Figure 5-14 and Figure 5-15, respectively. Results show a maximum realized gain of 13.8 dBi and a relative bandwidth of more than 9% at 24 GHz. To further enhance the gain of proposed antenna array we could have designed a dielectric lens on top of this 4x4 MPA array as proposed in chapter 3.

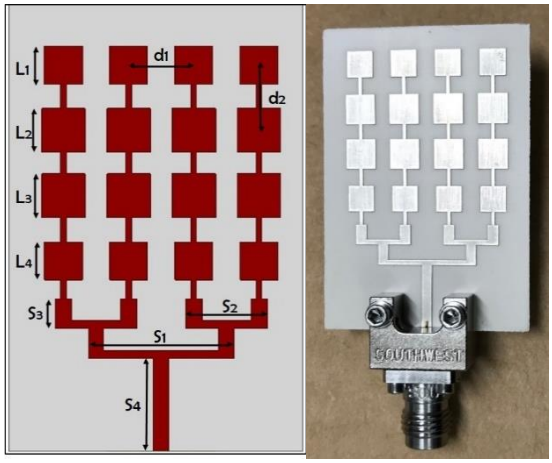

Figure 5-13 Planar 4x4 MPA array, a). Array Layout with dimensions L1=L4=3.5 mm, L2=L3=4 mm, d1=d2=6 mm, S1=13.4 mm, S2=7.5 mm, S3=2.7 mm, S4=8.55 mm, b). Fabricated array

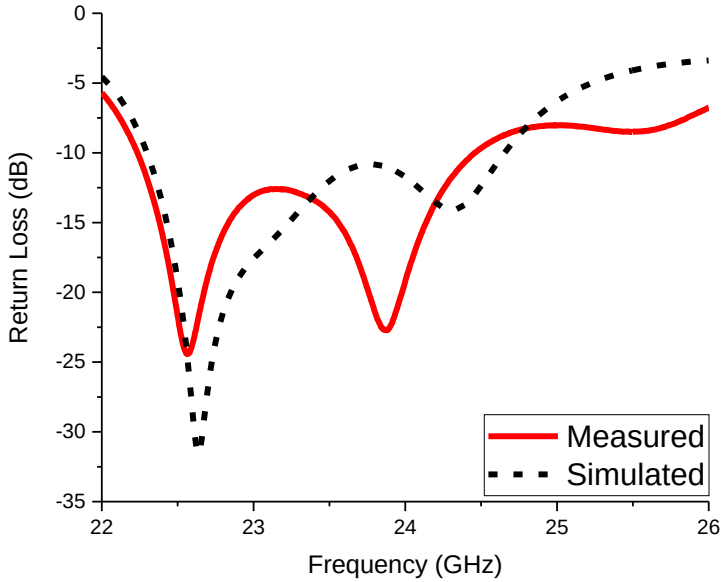

Figure 5-14 Simulated and measured return loss performance

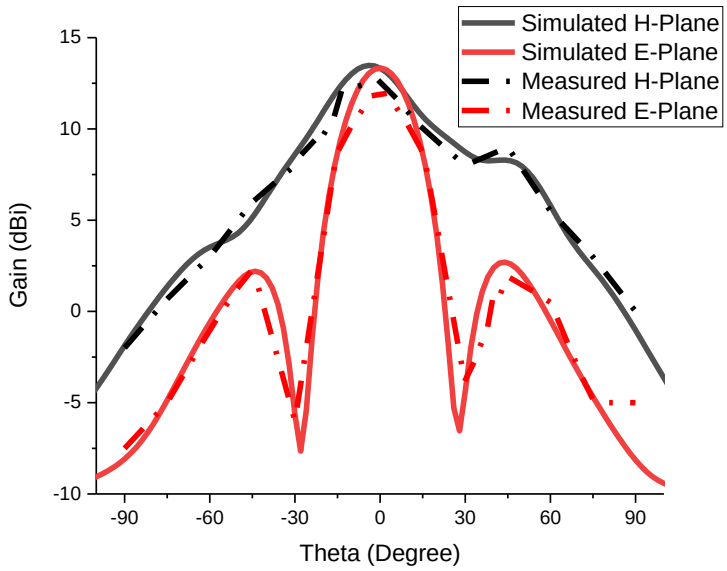

Figure 5-15 Simulated and measured *E*-plane and *H*-plane radiation pattern

5.1.4. Experimental results

5.1.4.1. Standalone rectifiers

After analysing the simulation results of the different rectifiers, the shunt and voltage doubler configuration with a MA4E2054A Schottky diode was selected for fabrication with samples shown in Figure 5-16. The circuits were fabricated on a 0.51 mm thick Roger 3003 substrate.

Precision field-replaceable 2.4 mm Southwest Microwave connectors were used to connect the circuits to the coaxial-based measurement equipment. The circuits were measured using a Keysight Signal Generator 24 GHz. The output voltage of the rectifier was measured at the load resistance of 200 Ω and 400 Ω for shunt and voltage doubler configurations respectively. The comparison of measured and simulated RF-DC conversion efficiency with respect to the RF input power is depicted in Figure 5-17 and Figure 5-18.

The differences between the simulated and measured results are attributed to the following reasons: (i) The simulation results were obtained from

Keysight ADS and the end-launch connector was not included in the simulation model; (ii) Fabrication tolerances, imperfect manual placement of parts, and soldering effects have shifted the optimum input impedance and DC load requirements.

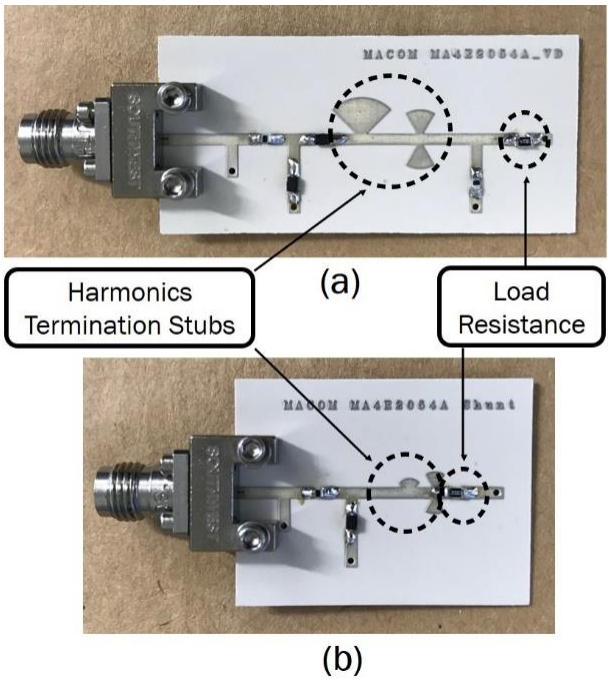

Figure 5-16 Fabricated rectifier circuits a). Voltage Doubler, b). Shunt

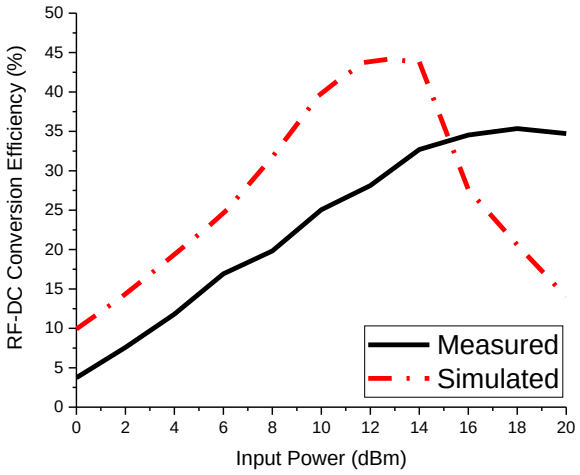

Figure 5-17 Measured RF-DC conversion efficiency of rectifier in shunt configuration as a function of input power

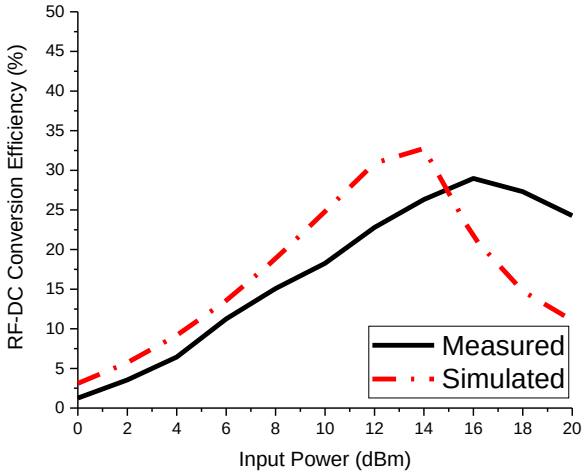

Figure 5-18 Measured RF-DC conversion efficiency of rectifier in voltage doubler configuration as a function of input power

5.1.4.2. Combined rectifier and antenna array (Rectenna)

In this section the measurements of rectifier circuits integrated with antenna arrays to form a complete rectenna for WPT at 24 GHz are presented and discussed. A fabricated sample of a rectenna along with the overall system measurement setup are shown in Figure 5-19 and Figure 5-20, respectively.

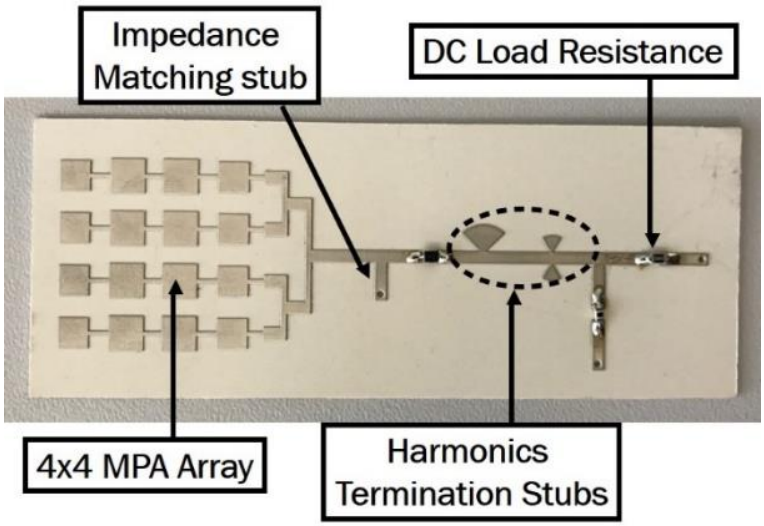

Figure 5-19 Fabricated rectenna prototype

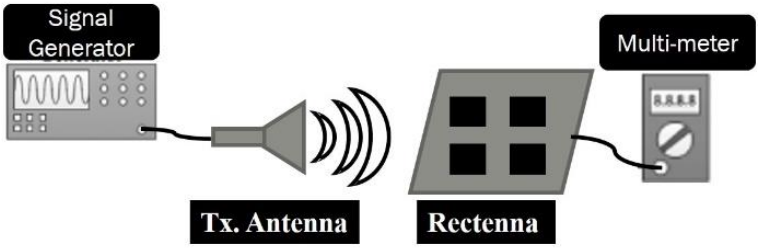

Figure 5-20 Rectennas measurement setup

A transmitter antenna, in this case a standard gain pyramidal horn, is connected to a signal generator E8267D, the output power of which is varied between 0 dBm and 20 dBm in 2 dBm steps at 24 GHz. The maximum output power was limited to 20 dBm due to the capabilities of signal generator. On the receive side, the proposed rectenna receives the RF power at a distance of 0.15 m and converts it to DC power at load resistance. Figure 5-21 shows the experimental results of the proposed rectenna. It can achieve a maximum output DC power of 0.51mW for a transmit power of 20 dBm at the specified distance of 0.15 m > far field distance (0.14 m). If we increase the distance between the transmitter and the rectenna or decrease the output power of signal generator the received power as well as efficiency decreases as shown in Figure 5-21.

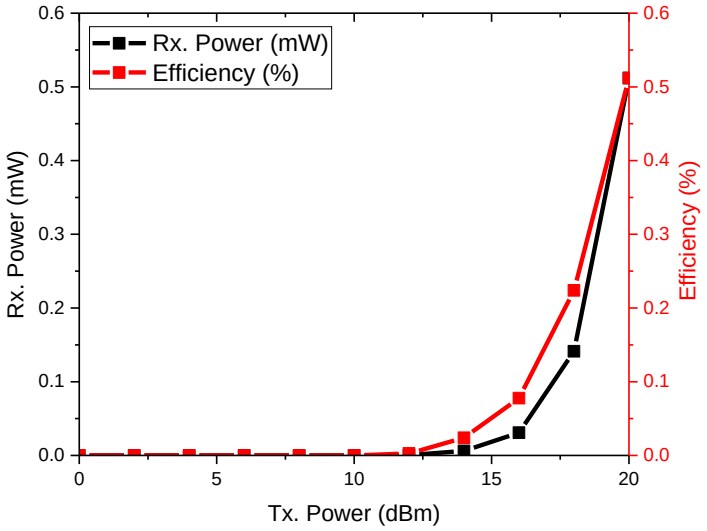

Figure 5-21 Measured output power and RF-DC conversion efficiency of proposed rectenna at 24 GHz as a function of input power at a distance of 0.15 m.

5.1.5. Demonstration of a complete WPT system for IoT sensor nodes

In this section the proposed rectennas are used for the practical demonstration of wireless power transfer to an IoT sensor node which communicates via backscatter modulation. The measurement setup is shown in Figure 5-22. An RF source transmits power to the IoT node at 24 GHz in order to provide enough energy for it to activate and take a single measurement. This way the need for batteries can be eliminated. The individual modules used in this demonstration are (i) the proposed rectifier in shunt configuration with a 4x4 planar antenna array; (ii) ultra-low power boost charger module (Texas Instruments BQ25570EVM) with a 4.7 mF charging capacitor to store the DC energy; (iii) a sensor node that uses a low-power microcontroller (ATtiny85) and switch (ADG901) that switches the RF channel between 0 Ω and 50 Ω for backscattering communication.

In particular, the backscattering sensor node tag reflects the incident RF carrier transmitted by a pure carrier illuminator by modulating the reflection coefficient of the receiving tag's antenna. This is simply achieved by connecting the antenna to two different loads (one for 0 information bit and the other for 1 bit). In our sensor node design, the load modulation is driven by the serial payload data packets generated by an ultralow power microcontroller unit (MCU). In a nutshell, our load modulation scheme translates to amplitude shift keying (ASK). We associate the higher reflection coefficient to the binary logic 0 and design a circuit which tries to minimize reflection coefficient for binary logic 1; (iv) The carrier is generated by the Nuand BladeRF software defined radio (SDR) transceiver with the transmit power of 14 dBm. The top blue waveform presents the received modulated carrier of a bit rate of 2.4 Kb/s.

Figure 5-23 shows the data received from the IoT sensor node that was energized by wireless power transfer at 24 GHz. The blue lines presents the received modulated data and the red waveform represents the decoded / demodulated data through level detection. As we can see, the reflection coefficient affects the distance between the two binary levels of the modulated carries and this directly effects the choice of constellation size 4 and the likelihood of correct demodulation (i.e., the bit error rate of the communication link). This approach combines the effectiveness of 24 GHz for narrow beam WPT and the near omnidirectional signal propagation properties at 868 MHz for data transfer.

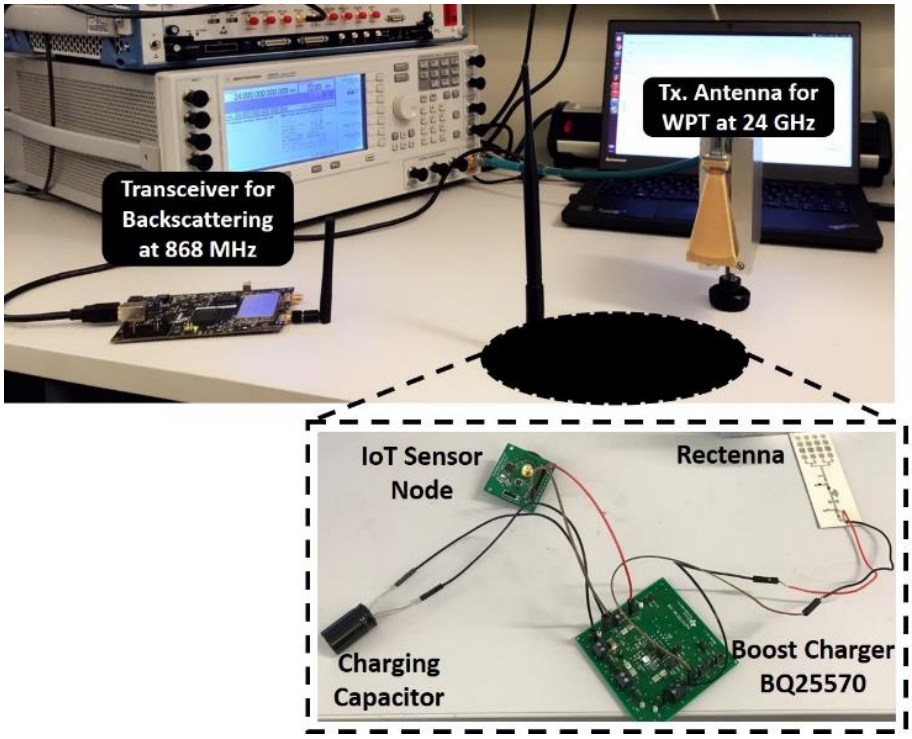

Figure 5-22 Measurement setup for WPT to backscattering IoT sensor node

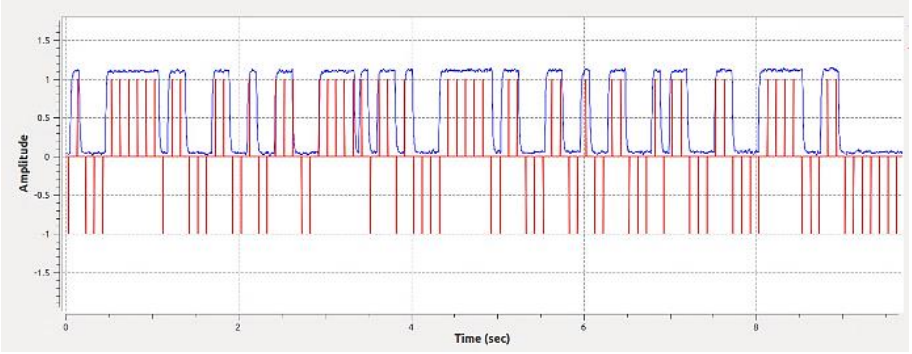

Figure 5-23 Data received through backscattering sensor node

5.2. Flexible rectennas for WPT to wearables

Flexible microwave circuits are required for the applications of wearable devices and conformal surfaces [139]. Therefore, flexible substrate materials and fabrication technologies such as microfabrication, inkjet printing, photolithography and 3D printing for flexible circuits became popular due to their number of applications in design and implementation of flexible devices [139]. The aforementioned fabrication technologies are less efficient due to high losses in printed substrates and limited accuracy of printers [139]. So in this research work we used a low loss but flexible substrate material due to very low thickness of 0.13mm.

There are very few reports available in published literature on flexible rectennas, i.e. a combination of an antenna and a rectifier. Jo Bito et al. [140] presented a flexible, inkjet-printed mmW rectenna with maximum output voltage of 2.5 V with 18 dBm of input power at 24 GHz for wearable IoT applications. Daskalakis et al. [141] developed a 24 GHz rectenna on paper substrate with RF-DC conversion efficiency of 32.5% at 15 dBm input power for RFID applications. Zhening Yang et al. [139] designed and fabricated a crossed dipoles array antenna at Ku band and K band for energy harvesting. The proposed antenna design has a maximum gain of 4 dBi at 22 GHz and a fractional bandwidth of 17% from 21.7 to 25.7 GHz for the K band. Kim et al. [142] presented the design and implementation of a flexible RF energy harvester using hybrid printed technology at UHF RFID band (868 MHz - 915 MHz) for far-field RF energy harvesting applications. The designed energy harvester generates a voltage above 2.9 V with an

efficiency of 20 % at -7 dBm of input power. In [143], a textile antenna for wearable energy harvesting at 26 and 28 GHz bands was presented. It exhibits a peak on-body gain of 7 dBi with an omnidirectional radiation pattern and radiation efficiency of 40%. In [144], a millimetre-wave flexible antenna using inkjet printing was proposed for energy harvesting applications at Ka band. It shows a peak gain of 7 dBi from 27 GHz to 31 GHz.

In this section we present the design, simulation and implementation of flexible antenna array and two different types of rectifiers depending on their configuration (shunt and voltage doubler) for wireless power transfer applications to wearable IoT devices. Initially the MPA array and the rectifier circuits are individually designed, optimized, fabricated and measured, and then the rectifiers are integrated directly with a conformal antenna array to form a complete rectenna. The whole rectenna was fabricated on a Rogers 3003 substrate with thickness = 0.13 mm, $\varepsilon_r = 3.0$ and $tan\delta = 0.001$.

5.2.1. Conformal antenna array design

A flexible cylindrical 8x3 MPA array for conformal surfaces and wearable IoT sensor nodes has been designed at 24 GHz. Simulation layout and fabricated prototype are shown in Figure 5-24(a) and Figure 5-24(b) respectively. A hybrid feed network was used for the excitation of the patches. After optimizing the simulation results for radiation pattern, the array was fabricated as planar by using very thin substrate material, i.e. Roger 3003 with thickness 0.13mm, and then wrapped array around a 3D

printed cylinder of radius *r = 10 mm* to make it conformal and to radiate in all directions.

The measured and simulated S-parameters and radiation pattern of conformal MPA array are presented in Figure 5-25 and Figure 5-26 respectively. It has a maximum realized gain of 4.8 dBi at 24 GHz and return loss of less than -40 dB across the 24.125 GHz ISM band. There is some difference in the simulated and measured reflection coefficients i.e. shift in resonant frequency. This shift in the resonant frequency could be due to the use of 3D printed dielectric cylinder to wrap the MPA array as shown in Figure 5-24(b).

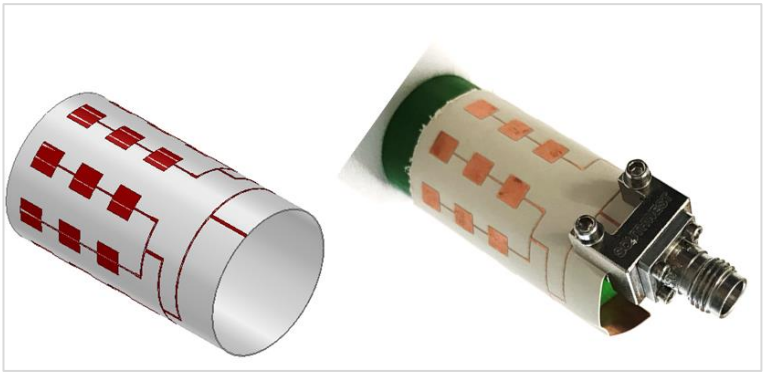

Figure 5-24 Conformal MPA array a). Simulation layout b). Fabricated prototype

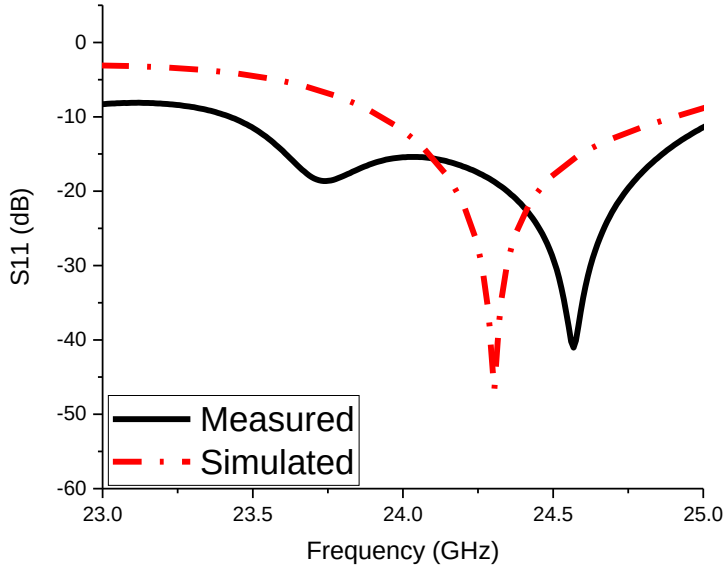

Figure 5-25 Simulated and measured S-parameters of conformal MPA array

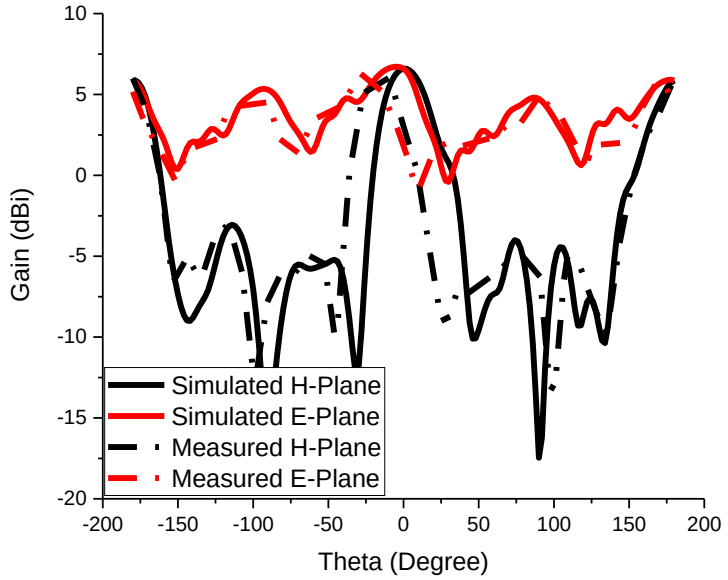

Figure 5-26 Simulated and measured *E*-plane and *H*-plane radiation pattern of conformal MPA array

5.2.2. Flexible rectifier design

5.2.2.1. Shunt configuration

The circuit schematic of flexible rectifier in shunt configuration is shown in Figure 5-27. The simulated RF to DC conversion efficiency of rectifiers in shunt configuration across different DC load resistance as a function of input power is shown in Figure 5-28. It can be seen that it gives a maximum RF-DC conversion efficiency of 35% at 300 Ω DC load resistance with an input power of 14 dBm at 24 GHz frequency.

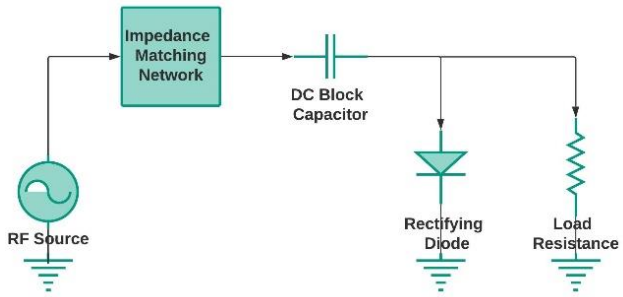

Figure 5-27 Rectifier circuit in shunt configuration

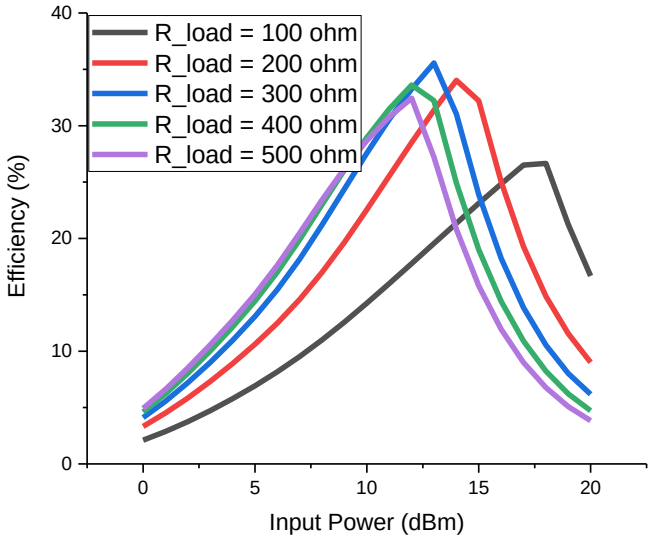

Figure 5-28 Simulated RF-DC conversion efficiency as a function of input power across different DC load resistance

5.2.2.2. Voltage Doubler configuration

Figure 5-29 shows the rectifiers layout in voltage doubler topology. It gives a maximum RF-DC conversion efficiency of 20% with 14 dBm input power and 300Ω load resistance as shown in Figure 5-30. ADS schematic of proposed rectifier circuit is given in Appendix D.

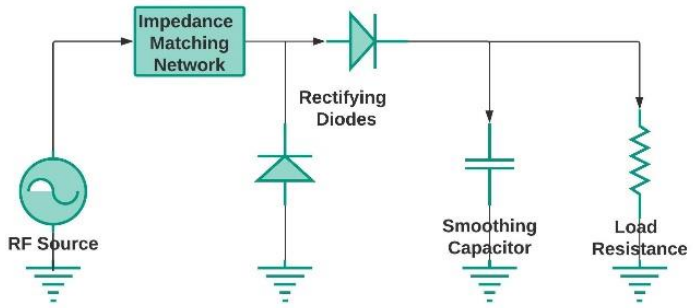

Figure 5-29 Rectifier circuit in voltage doubler configuration

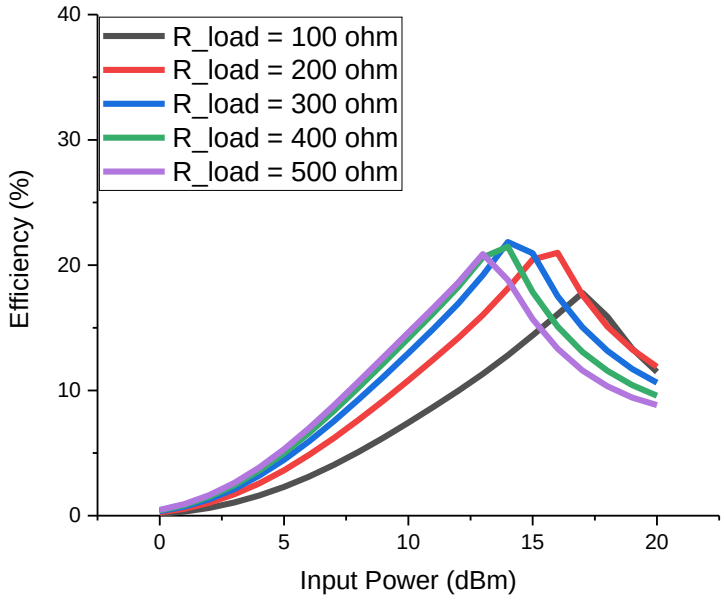

Figure 5-30 Simulated RF-DC conversion efficiency as a function of input power across different DC load resistance

5.2.3. Comparison of flexible rectifier topologies

A performance comparison of aforementioned rectifier topologies in terms of RF-DC conversion efficiency are presented in Figure 5-31(a) and Figure 5-31(b) as a function of load resistance and input power respectively at 24 GHz. It can be seen that the rectifier in shunt topology gives a maximum efficiency of 35% with an input power of 14 dBm across 300 Ω DC load resistance. As expected the RF-DC conversion efficiency of shunt topology is better than the voltage doubler due to more power consumption by the multiple diodes in latter topology [127, 145].

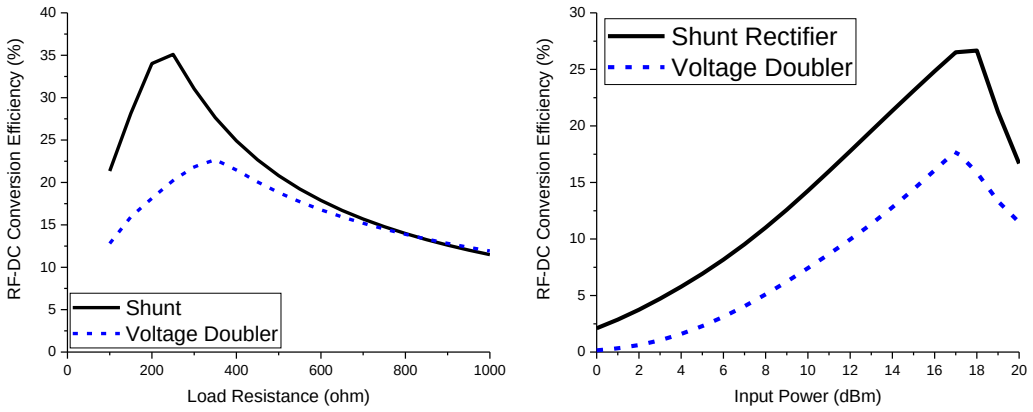

(a) (b)

Figure 5-31 Simulated RF-DC conversion efficiency as a function of (a) load resistance at 14 dBm, (b) input power for 300Ω load resistance

5.2.4. Experimental results and discussion

5.2.4.1. Standalone rectifiers

An extensive set of simulations as discussed in section 5.1.1, using Ansys HFSS™ and ADS, were carried out to optimize the gain of antenna array and RF-DC conversion efficiency of rectifier circuits to get the most optimum rectenna for WPT to wearables.

To validate the simulated results, the proposed conformal rectifier circuits were fabricated on a 0.13 mm thick Roger 3003 substrate material. Photographs of these fabricated rectifier circuits are shown in Figure 5-32. Precision field-replaceable 2.4 mm Southwest Microwave connectors were used to connect the circuits to the coaxial-based measurement equipment. The circuits were measured using a Keysight Signal Generator at 24 GHz. The output voltages of the rectifiers were measured across 300Ω DC load resistance. The comparison of measured and simulated RF-DC conversion efficiency with respect to the RF input power are depicted in Figure 5-33 and Figure 5-34 for shunt and voltage doubler configuration respectively**.**

Again, there is some inconsistency between the measured and simulated results due to three major reasons as mentioned and discussed in section 5.1.4.

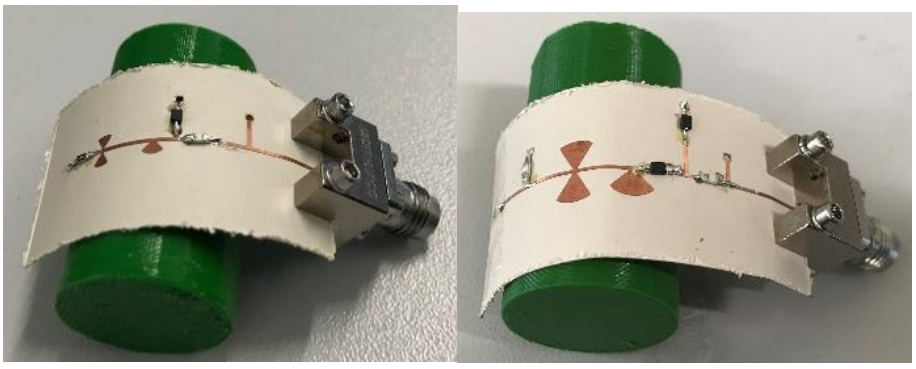

Figure 5-32 Fabricated conformal rectifier circuits a) shunt b) voltage doubler

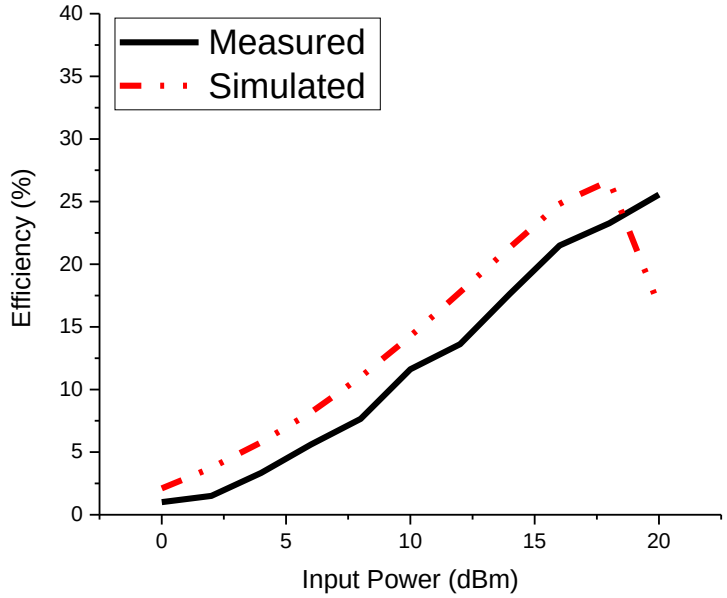

Figure 5-33 Measured RF-DC conversion efficiency of conformal rectifier in shunt configuration as a function of input power

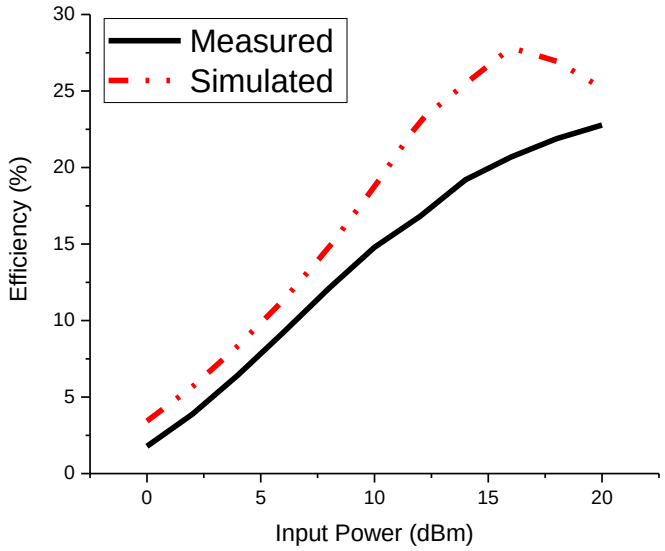

Figure 5-34 Measured RF-DC conversion efficiency of conformal rectifier in voltage doubler configuration as a function of input power

5.2.4.2. Combined flexible rectifier and conformal antenna (Rectenna)

In this section the rectifier circuit is combined with the antenna array to form a complete rectenna for WPT to wearable IoT devices at 24 GHz. The fabricated prototype of flexible rectenna on a conformal surface is shown in Figure 5-35. The measurement setup was the same as discussed in section 5.1.4.2. In this rectenna prototype an *8x3* MPA array connected to 8 individual rectifiers and the voltage across the DC load resistance of each rectifier added up in series by using jumper wires as shown in Figure 5-35.

Figure 5-35 Fabricated flexible rectenna prototype on a conformal surface

Figure 5-36 shows the measured results of output power and RF-DC conversion efficiency of proposed conformal rectenna array. It shows a maximum output DC power of 2.4mW with a transmit RF power of 20 dBm at a distance of *d = 0.15m.* The RF-DC conversion efficiency and measured

output power of proposed flexible rectennas will make them a promising candidate for mmW WPT to conformal / wearable IoT devices and on-body medical and health monitoring applications.

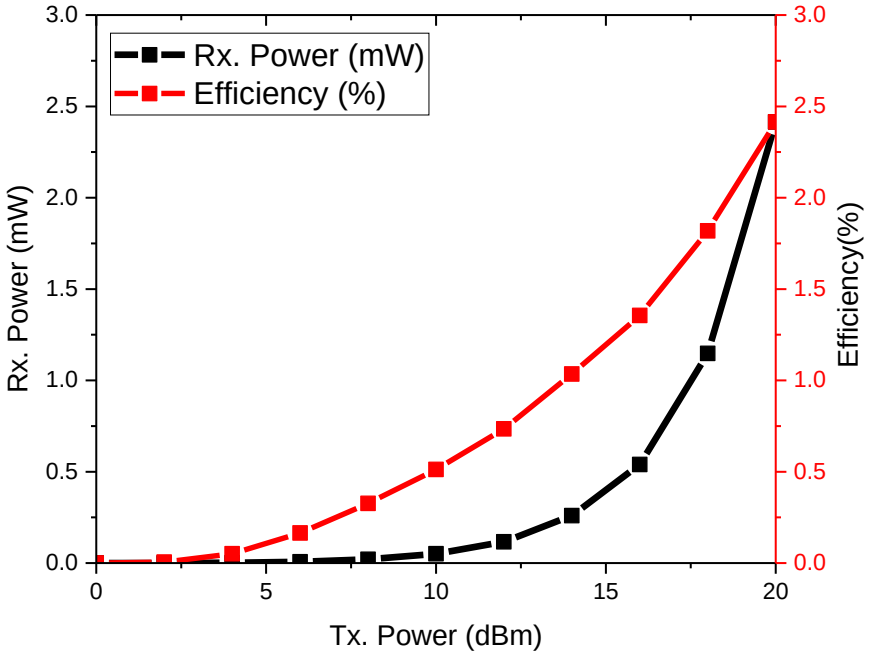

Figure 5-36 Measured output Power and RF-DC conversion Efficiency of conformal rectenna as a function of input power at d = 0.15m

5.3. Tapered slot antenna for WPT in pipe robot

A tapered slot antenna (TSA) / Vivaldi antenna has been designed, simulated and fabricated for WPT to a robot prototype inside a gas pipeline. All the antenna parameters such as length of microstrip feed line, angle of radial stub at the end of transmission feed line and size of tapered slot are optimized in Ansys HFSS to get maximum gain and radiation efficiency. The conventional design equations and procedure for tapered slot antenna is given in [7, 146]. The antenna layout and the fabricated prototype is shown in Figure 5-37 and Figure 5-38 respectively. The antenna is fabricated on a

0.78mm thick Rogers RT/Duroid 5880 substrate material with $\varepsilon_r = 2.2\ and\ tan\delta = 0.0015$. Precision field-replaceable 2.4 mm Southwest Microwave connectors were used to connect the antenna with network analyser. The circuits were measured using a Keysight network analyser over the frequency range of 10 GHz – 40 GHz.

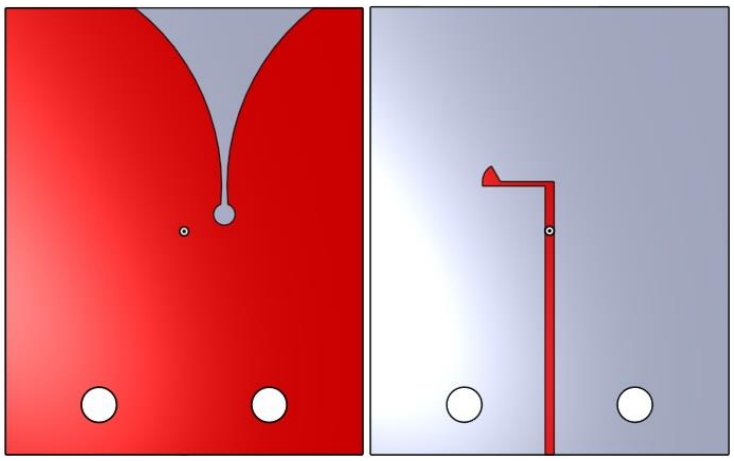

Figure 5-37 Design of tapered slot antenna (Vivaldi antenna)

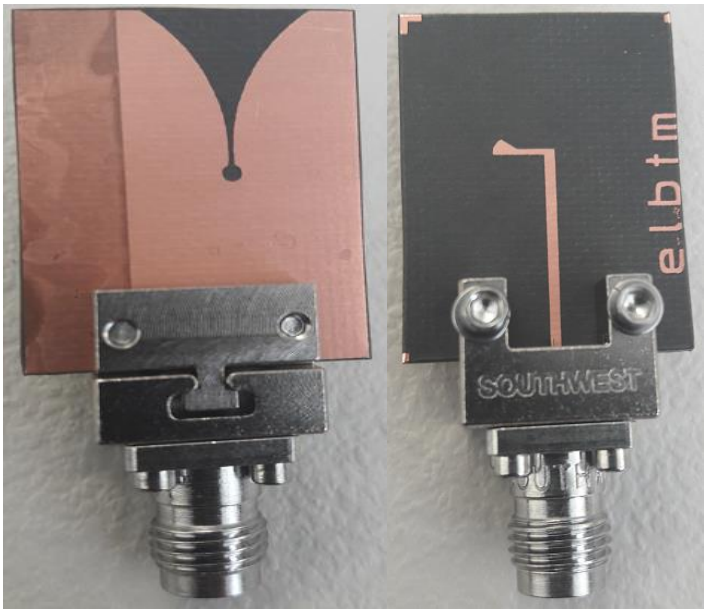

Figure 5-38 Top and bottom view of fabricated prototype of Vivaldi antenna

The measured and simulated return loss of proposed TSA is presented in Figure 5-39. It shows a large impedance bandwidth from 10 GHz to 35 GHz at -6 dB return loss level covering Ku Band, 24 GHz ISM band, K and Ka Band.

Figure 5-40 depicts the simulated radiation pattern of the proposed antenna. It presents a good directional end-fire radiation pattern with a maximum gain of 7.8 dBi and radiation efficiency of 0.89 at 30GHz. The gain of TSA over the whole bandwidth is shown in Figure 5-41. It has a minimum gain of 5.2 dBi at 15 GHz.

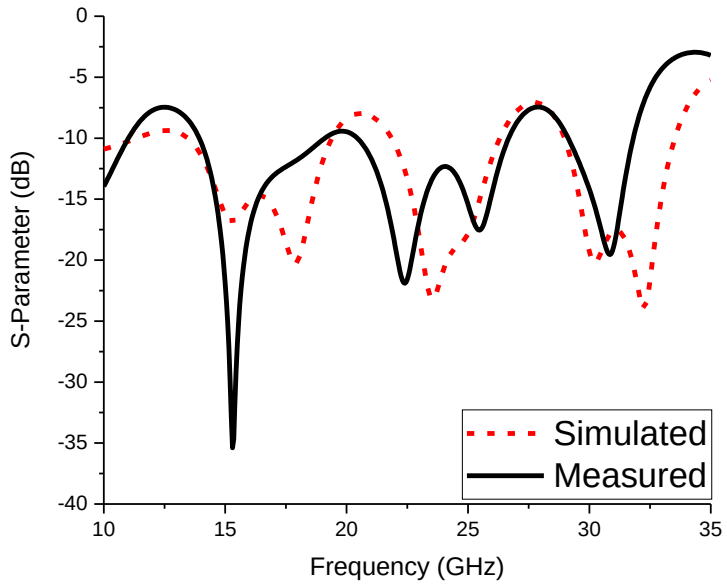

Figure 5-39 Measured & simulated return loss of tapered slot antenna

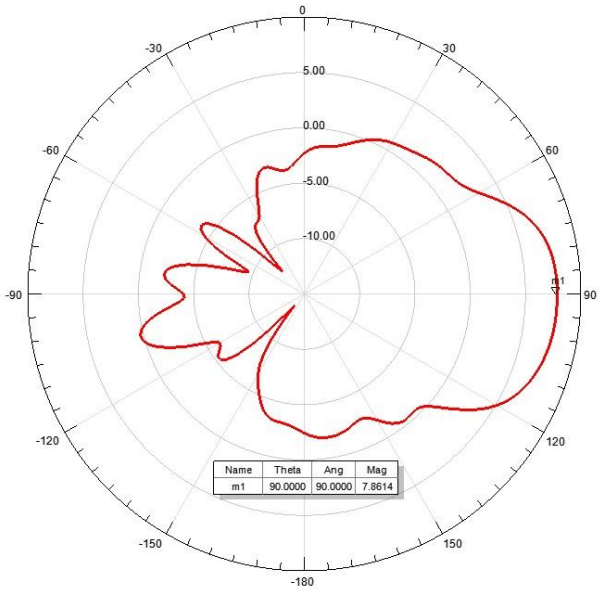

Figure 5-40 Simulated radiation pattern of tapered slot antenna

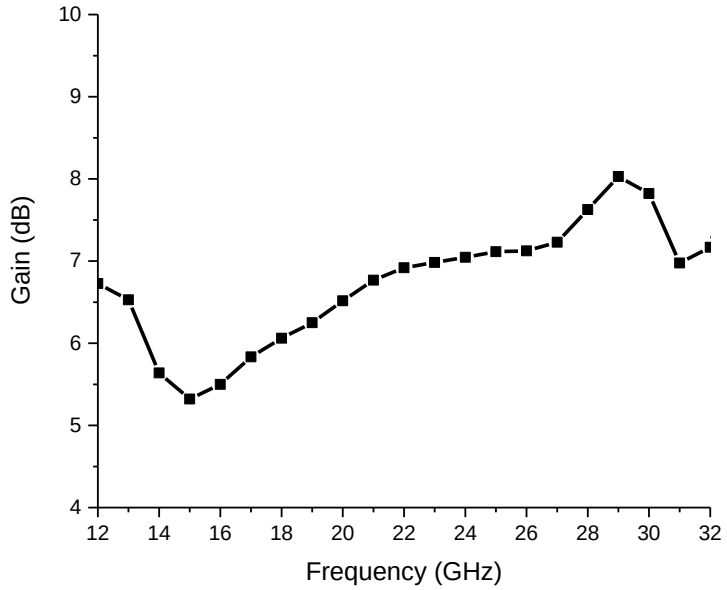

Figure 5-41 Gain of TSA for wide frequency range

The proposed tapered slot antenna was used for millimetre waves far field wireless power transfer to a small robot prototype inside a metallic pipe of 2.5cm diameter as shown in Figure 5-42. Proposed antenna was specially design for this type of application due to its end fire radiation pattern which

is suitable to fit the antenna on a robot prototype inside a narrow pipeline. I would like to mention here that the Vivaldi antenna work preceded the earlier proposed MPAs and ILAs. This was an initial investigation based on some other exploratory work and the future work might expect to swap to a different antennas possibly the MPA and ILA after comparative evaluation. The ability to transfer power wirelessly through the pipe allows the robot to operate for extended periods of time. This reduces the cost of pipe inspection and allows efficient detection of anomalies and cracks. Figure 5-42(a) and Figure 5-42(b) shows the simulation and measurement setup to analyse the response of antenna and WPT inside the metallic pipe respectively. A two meter long metallic pipe made up of cast iron was used for practical demonstration of WPT to robot inside a 1” metallic pipe. A Keysight Signal Generator E8267D was used to transmit power inside the metallic pipe through a standard gain pyramid horn antenna.

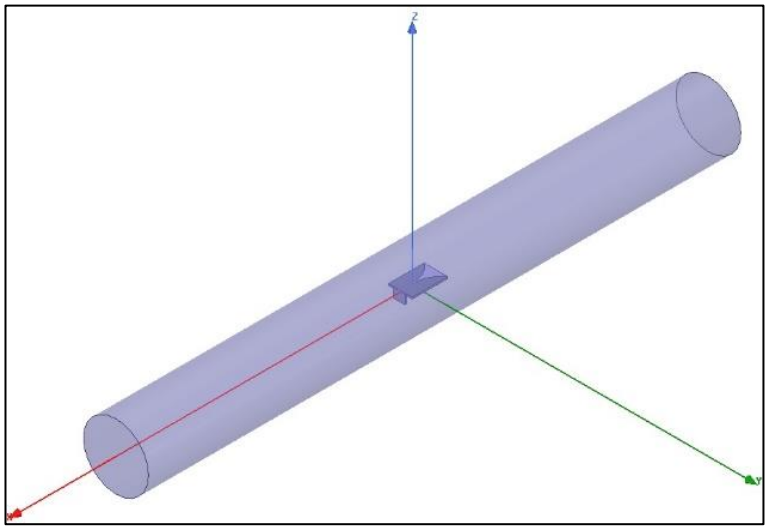

(a)

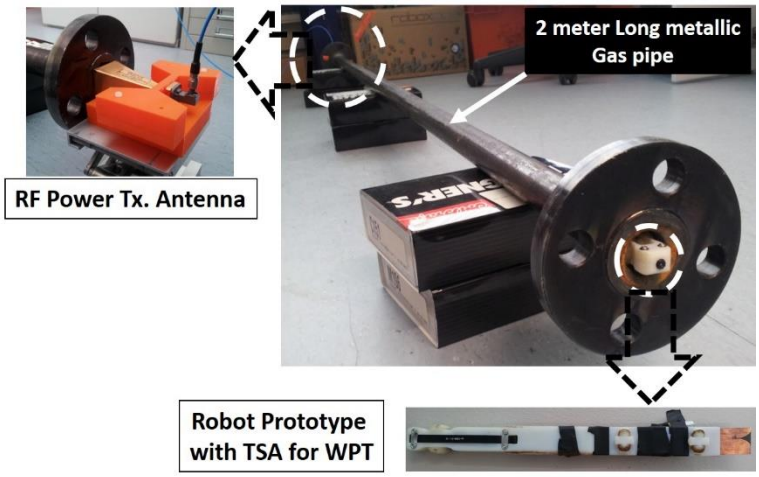

(b)

Figure 5-42 (a). Simulation, (b). Experimental setup for WPT to robot inside a metal pipe

The simulated transmission and reflections coefficients of proposed TSA inside a metallic pipe of 2m length is shown in Figure 5-43. Port 1 is defined on one open side of the pipe and port 2 is defined as the input port of Vivaldi antenna. Figure 5-44 shows the comparison of propagation loss measured with the standard horn antenna and proposed TSA. Due to very rough surface of metallic pipe from inside the propagation loss varies from -30 to -40 dB for a frequency range of 24 GHz to 34 GHz.

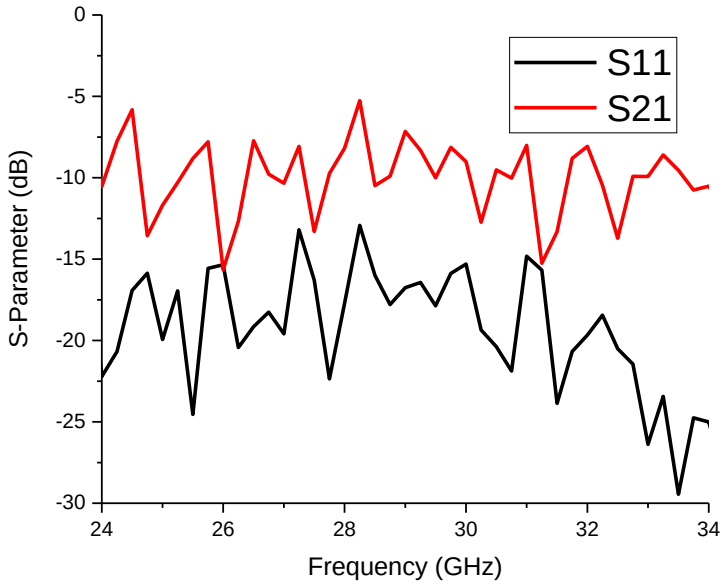

Figure 5-43 Simulated S-Parameters of TSA inside the metallic pipe

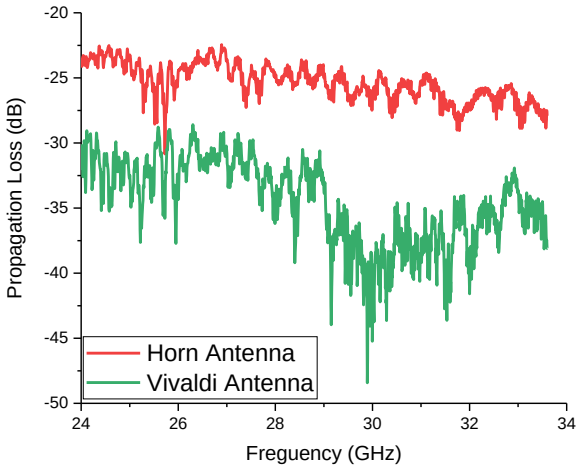

Figure 5-44 Propagation loss measurements inside the metallic pipe

For practical demonstration of WPT to a robot prototype inside a 1” metallic pipe the TSA with a rectifier was mounted on one side of robot prototype and camera cable on the other side for inspection as shown in Figure 5-45. The design, manufacturing and assembly of robot prototype was done by other group members of this research project.

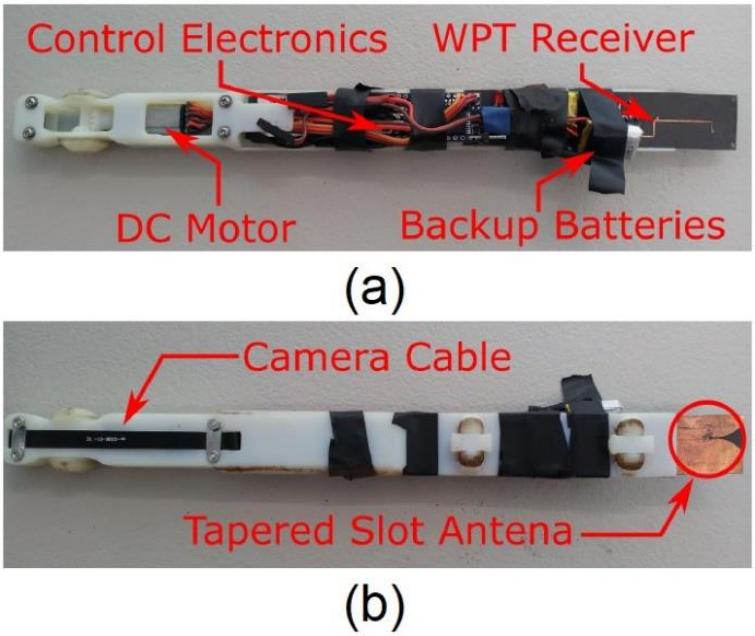

Figure 5-45 Robot prototype having TSA with rectifier for WPT inside the metallic pipe

5.4. Chapter summary

A complete wireless power transfer system for powering IoT sensor nodes at 24 GHz has been presented in this chapter. The RF-DC conversion efficiency of three different rectifier topologies using two different diodes was examined. Flexible antenna array and rectifiers for WPT to wearable IoT devices were also presented and discussed. According to the simulation results, the rectifier circuit with maximum RF-DC conversion efficiency is chosen as the rectifying component in the WPT system. A planar 4x4 MPA array and a conformal 8x3 MPA array with measured gain of 13.8 dBi and 4.8dBi respectively were used in the design and development of a rectenna. The MPA arrays and the rectifier circuits were fabricated and measured separately to verify the performance of the individual components. Then the designed antenna arrays and rectifiers were integrated together and

fabricated on a single board to validate the rectenna. A maximum output DC voltage of 2.5 V with a measured RF-DC conversion efficiency of 31% was observed across 200 Ω DC load resistance with 20 dBm input power at 24 GHz. The obtained results present a significant enhancement in the design of high-efficiency WPT rectennas. Finally, the application of the system to low-power IoT sensor nodes was demonstrated by wirelessly charging a custom sensor that communicates via backscattering.

Chapter 6. Conclusion and Future Work

6.1. Conclusion

In this thesis, challenges and possible solutions for high gain and efficient antenna arrays and a number of microwave components for future 5G wireless communication have been investigated with the aid of computationally extensive simulations and experimental verification. In regards to microstrip patch antenna arrays for mmW frequency bands, the major issues are the low gain and directivity due to high losses in substrate material and transmission lines for feeding the elements of MPA array, design complexity and mutual coupling due to the very narrow distance between the elements of MPA array at mmW frequencies and increase of cost and size of antenna arrays to achieve high gain and beam steering capabilities. To overcome these issues different approaches and techniques have been proposed for the design and fabrication of low-cost and high gain antenna arrays, phase shifters and rectifiers.

The work presented in chapter 2 was a novel simplified approach to design high-gain aperture-coupled microstrip patch antenna (AC-MPA) arrays with improved radiation pattern for mmW applications such as simultaneous wireless information and power transfer (SWIPT) and Internet-of-Things (IoT) device connectivity. Higher-order mode substrate integrated waveguide (SIW) cavity is used to feed the MPA arrays through aperture coupling which is easy to design as compared to microstrip transmission lines or coplanar waveguide (CPW) feeding methods for MPA arrays. Key performance metrics are side-lobe levels of less than -24 dB and -29 dB in the E-plane and -22 dB and -26 dB in the H-plane and realized gain of 11

dBi and 15 dBi for the 2x2 and 4x4 arrays respectively, at a design frequency of 30 GHz.

The work presented in chapter 3 was based on low cost solution to enhance the gain and directivity is the use of three-dimensional (3D) integration of low-cost, low-loss and easy-to-fabricate 3D-printed Integrated Lens Antennas (ILAs) for 5G broadband wireless communications. The ILAs are fabricated using Polylactic Acid (PLA) as the fused deposition modelling (FDM) polymer with an optimized infill density of 50%, which speeds up prototyping time and decreases the relative permittivity, dielectric loss, manufacturing cost, and overall mass of the lens. A study on the effect of infill pattern and infill density of 3D printed lenses on the radiation properties of ILAs and dielectric characterization of PLA having different infill densities are also presented and discussed in this chapter. All findings suggest that in-depth studies on infill patterns and infill density are necessary for design and development of dielectric lens antennas using 3D printing technology. From the measurement results, the ILAs achieve a fractional bandwidth of 10.7%, ranging from 26.5 GHz to 29.4 GHz with a maximum gain of 15.6 dBi at boresight and half power beam-width of approximately 58° and 75° in the *E* and *H* plane, respectively.

The work in chapter 4 is related to phase shifters and hollow integrated waveguides. Phased arrays can be used to not only focus the beam but also to steer the beam in a desired direction using different beamforming and beam steering antenna array techniques. In regard to beam steering antennas for 5G communications, a novel compact and broadband

reconfigurable SIW phase shifter intended for beam steering applications in antenna arrays for 5G wireless communication has been proposed and partially evaluated where the phase shift was achieved via reconfigurable metal posts which are manually switched between capacitive and inductive loading. To further enhance the performance of SIW components a novel design and fabrication of a low cost and low loss, easy to fabricate and integrate 3D printed hollow integrated waveguide (HIW) has been proposed. The inner structure of HIW was fabricated using a desktop 3D printer and copper rivets are used instead of electroplated via holes to make the side walls of HIW.

Finally, several rectenna (an antenna integrated with a rectifier) circuits for mmW far field WPT were presented in Chapter 5. One of the major requirement of WPT is a highly directional and high gain antenna along with a rectifier having high RF-DC conversion efficiency. The design and implementation of efficient & compact rectenna for wireless power transfer applications in IoT sensor nodes and robotics are presented and discussed. A complete wireless power transfer system for IoT sensor nodes at 24 GHz has been designed and demonstrated.

The proposed approaches and techniques presented in this thesis will be a significant enhancement in the design and implementation of a cost-effective and efficient antenna arrays and other microwave components at millimetre-waves for 5G communications and WPT applications as compared to the state-of-the-art.

6.2. Future Work

The objectives of this research work have been successfully achieved which are reported in this thesis and most of them are published as journal and conference papers.

The work presented in chapter 2 is based on the design and implementation of new simplified approach for the excitation of MPA arrays using higher order mode SIW cavity through aperture coupling was presented. Future developments could see the same design approach used to implement larger arrays of 8x8 and 16x16 elements, as well as at higher frequency bands such as 60 GHz as well. Additionally, the bandwidth could be improved using enhancement techniques discussed previously.

In chapter 3, the design and fabrication of low cost 3D printed dielectric lens antennas for gain enhancement. The proposed lens antennas can have possible applications in unmanned aerial vehicles (UAVs) for high-speed, point-to-point communication with sensor nodes. In future work a practical demonstration of this application and scenario could be done to prove the concept.

In chapter 4 a novel approach to design a compact and broadband reconfigurable SIW phase shifter for 5G phased array antennas has been presented and to quickly validate the concept copper strips are used instead of PIN diodes for fabrication and measurements. In future work the PIN diodes could be used instead of copper strips to make it electronically controllable and proposed phase shifters could be integrated with antenna arrays to develop a phased array for 5G communications.

Chapter 5 presented the design and implementation of mmW antenna arrays and rectifiers for wireless power transfer to IoT sensor nodes, wearable IoT devices and pipe robots. A complete demonstration of mmW wireless power charging to IoT sensor nodes with a drone could be investigated in future research work.

A simple conformal antenna array and flexible rectifiers for WPT applications were also presented in chapter 5. In future more research work could be done for the design and implementation of low-cost 3D printed conformal and flexible antenna arrays for robots and UAVs. We could potentially integrate and fabricate the lens antenna and robot prototype together by using low-cost 3D printing technology. Infill pattern and infill density of 3D printing technology could be investigated for beamforming.

Appendix A

List of Publications

1. B. T. Malik, V. Doychinov, S. A. R. Zaidi, I. D. Robertson and N. Somjit, *"Antenna Gain Enhancement by Using Low-Infill 3D-Printed Dielectric Lens Antennas", IEEE Access*, vol. 7, pp. 102467-102476, 2019. DOI: 10.1109/ACCESS.2019.2931772.

2. Bilal T Malik, Viktor Doychinov, Syed Ali R Zaidi, Nutapong Somjit, Ian D Robertson and Charles W Turner, *"Higher-order mode substrate integrated waveguide cavity excitation for microstrip patch antenna arrays at 30-GHz"*, Journal of Physics Communications, vol. 3, 2018. DOI: 10.1088/2399-6528/AB0074.

3. B. T. Malik, V. Doychinov and I. D. Robertson, *"Compact broadband electronically controllable SIW phase shifter for 5G phased array antennas",* 12th European Conference on Antennas and Propagation (EuCAP 2018)*,* London, 2018, pp. 1-5. DOI: 10.1049/CP.2018.1257.

4. Bilal T Malik, Viktor Doychinov, Syed Ali R Zaidi, Ian D Robertson, Nutapong Somjit and Robert Richardson, "*Flexible rectennas for wireless power transfer to wearable sensors at 24 GHz",* Research, Invention, and Innovation Congress (RI2C), 2019.

5. Viktor Doychinov, B. Kaddouh, G. Mills, Bilal Malik, N. Somjit, Ian Robertson, *"Wireless power transfer for gas pipe inspection robots"*, The UK-RAS Network Conference on Robotics and Autonomous Systems, 2017.

Forthcoming:

6. Bilal T Malik, Viktor Doychinov, Ali Hayajneh Syed Ali R Zaidi, Ian D Robertson and Nutapong Somjit, "*24 GHz wireless power transfer system for IoT sensors".* (Ready for Submission).

7. Bilal T Malik, Nuttapong Duangrit, Viktor Doychinov, Nuttapong Somjit and Ian D. Robertson*, "24-40 GHz low-cost & low-loss 3D printed hollow integrated waveguide"*. (Ready for Submission).

Appendix B

Aperture coupled microstrip patch antenna (AC-MPA)

Figure B1 and B2 shows the simulation model and the radiation pattern of AC-MPA if we use TE303 propagation mode for the excitation of 3x3 MPA array as done in previous open literature works. This approach gives very high side lobe levels and low gain as compared to our proposed design approach of using TE303 propagation mode for the excitation of 2x2 MPA array.

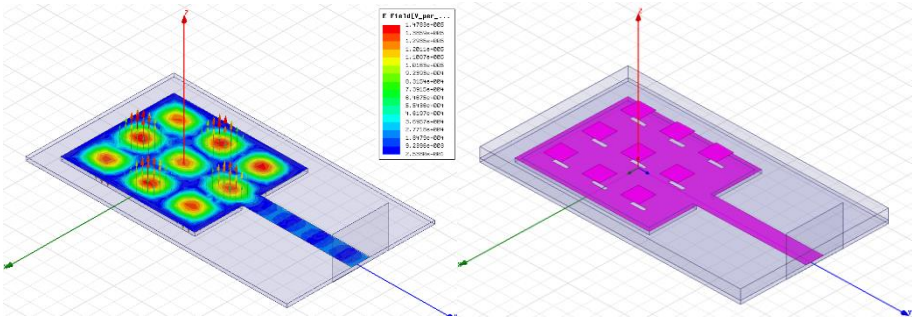

(a) (b)

Figure B1: AC-MPA (a). E-field distribution for TE303, (b). Simulation setup having 3x3 coupling slots and radiating patches on top of each and every E-field maxima and minima

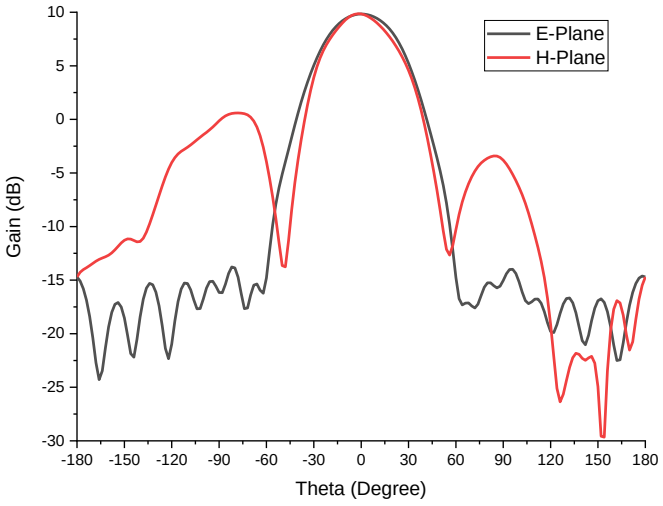

Figure B2: Radiation pattern of AC-MPA array shown in Figure B1.

Parametric analysis on width (*Ws*) and length (*Ls*) of coupling slots

Figure B3 and Figure B4 shows the optimization results of length and width of coupling slots. It can be seen that the length of slots changes the resonant frequency of the antenna and width of slots effects the impedance matching. Figure B4 shows the effects of changing the dimensions of coupling slots on the radiation pattern of antenna arrays.

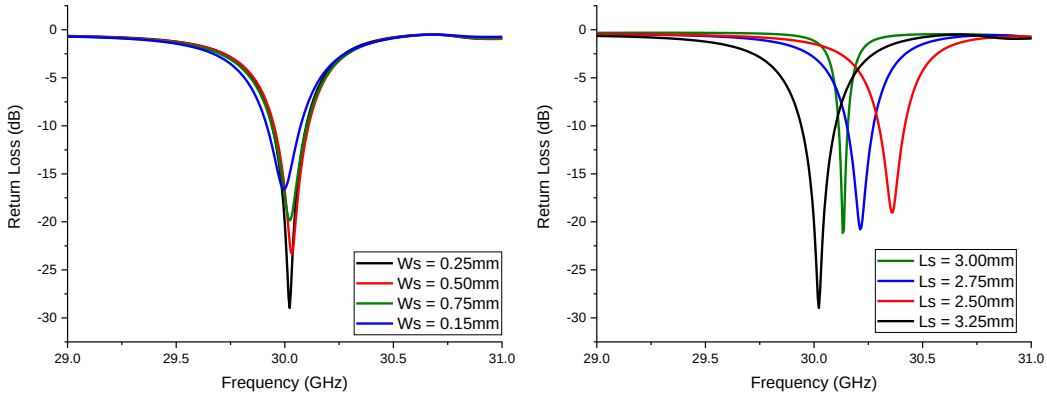

Figure B3: S-parameters of AC-MPA array for different values of length (Ls) and width (Ws) of coupling slots

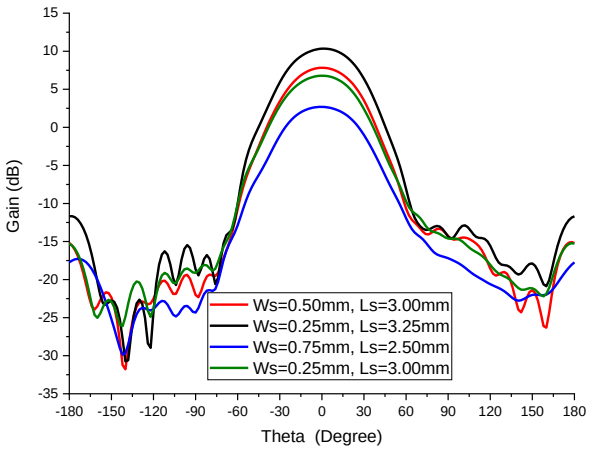

Figure B4: Radiation pattern of AC-MPA array for different values of Ls and Ws of coupling slots

Appendix C

Gated Reflect Line (GRL) calibration for dielectric characterization

Gated Reflect Line (GRL) is two step calibration process. In first step a two port TRL calibration at the coaxial input into the antennas removes errors associated with network analyser and cables and in second step, A thru and a metal plate for reflect to complete the calibration by removing the errors associated with antennas and fixturing as shown in Figure C1 below:

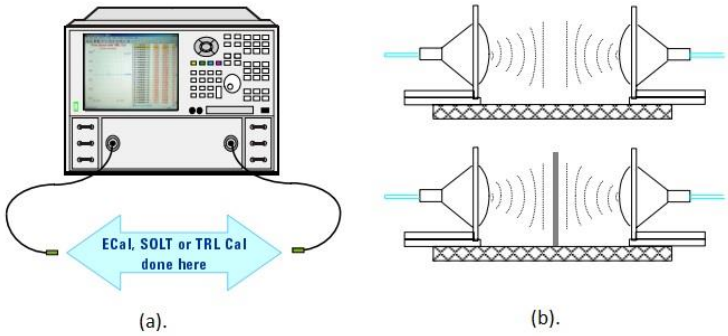

Figure C1: GRL calibration process (a). First step (b). Second step

Parametric Analysis on *R* and *H* of the Dielectric Lens

A comprehensive parametric analysis has been done to analyse the effects of different parameters of dielectric lens on the behaviour of radiation patterns of ILAs. Figure C2-C3 shows the effect of changing the radius R and extended height H of dielectric lens on the E-plane and H-plane radiation patterns of ILAs using SIW slotted array and MPA array as source antennas. By increasing the radius and extended height of dielectric lens the gain of antennas start increasing and at a certain point it reaches a maximum value after than the gain of antenna start decreasing. So we can say for dielectric lens antennas we have to optimize the certain parameters of dielectric lens to get optimum value of gain.

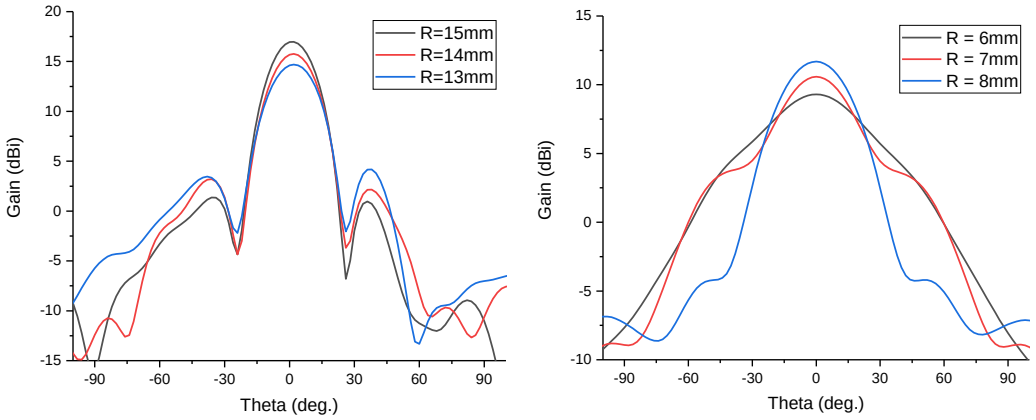

Figure C2: Radiation pattern of ILA at 28 GHz for different values of radius *R* of dielectric lens (a) SIW (b) MPA

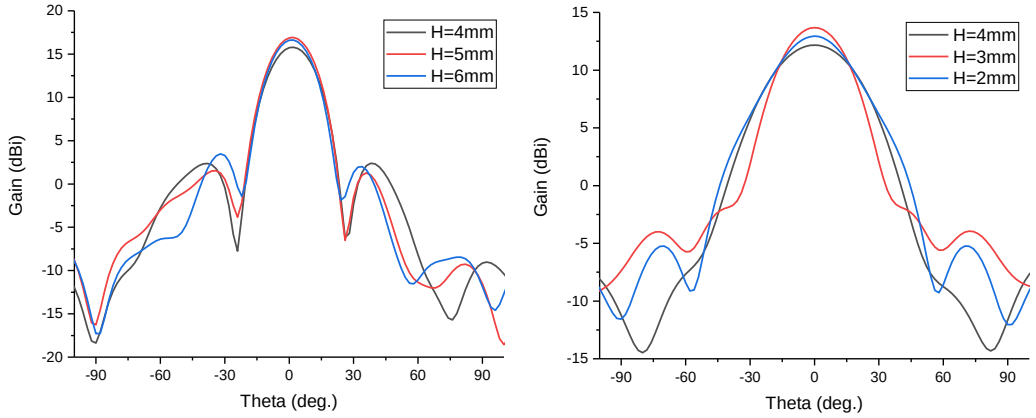

Figure C3: Radiation pattern of ILA at 28 GHz for different values of extended length H of dielectric lens (a) SIW (b) MPA

Probe method for dielectric characterization of PLA samples

Keysight technologies 85070E dielectric probe kit was also used to measure the dielectric properties of PLA samples having different infill densities to validate and compare the results of free space measurements. Figure C4 shows the 3D printing of PLA samples and measurement setup for dielectric characterization (DC) using Keysight probe method. Measured relative permittivity and dielectric loss of different PLA samples are shown in Figure C5. These results validates the free space measurements.

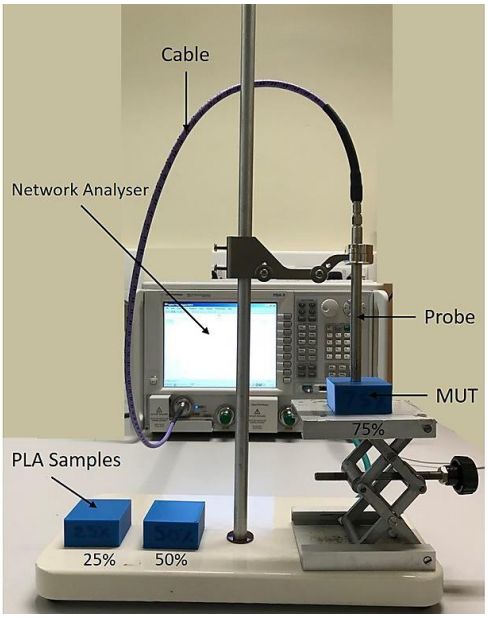

Figure C4: Measurement of dielectric properties of PLA samples

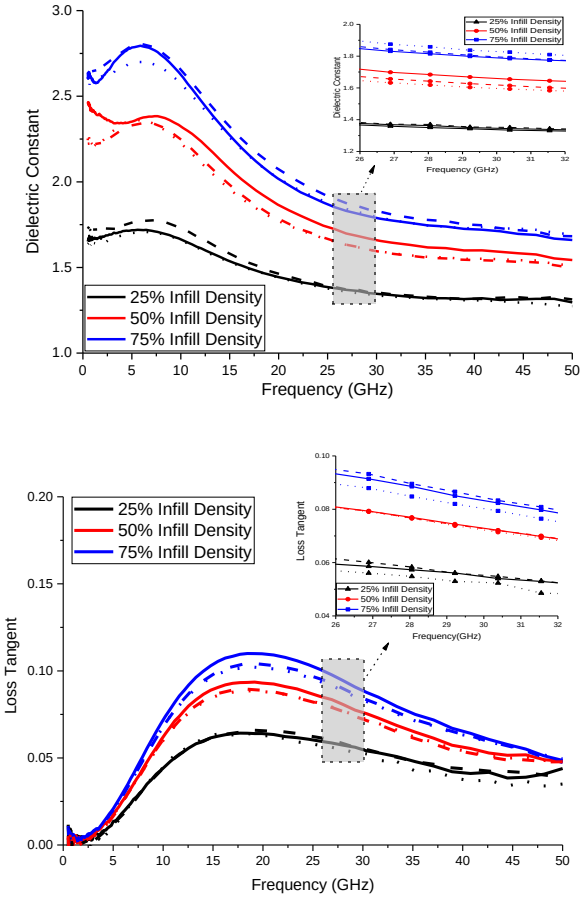

Figure C5: Dielectric characterization of PLA samples having different infill densities (a). Dielectric constant (b). Loss tangent

Measurement setup for radiation pattern of antennas

A Keysight E8361C PNA was used to measure the radiation patterns in a far-field anechoic chamber, using a 20 dBi WR-28 standard gain pyramidal horn antenna as a transmit antenna. The gain at boresight of the proposed antenna was determined using the gain transfer method, with two 20 dBi WR-28 reference pyramidal horns used to establish a baseline. Radiation pattern measurement setup is shown in Figure C6.

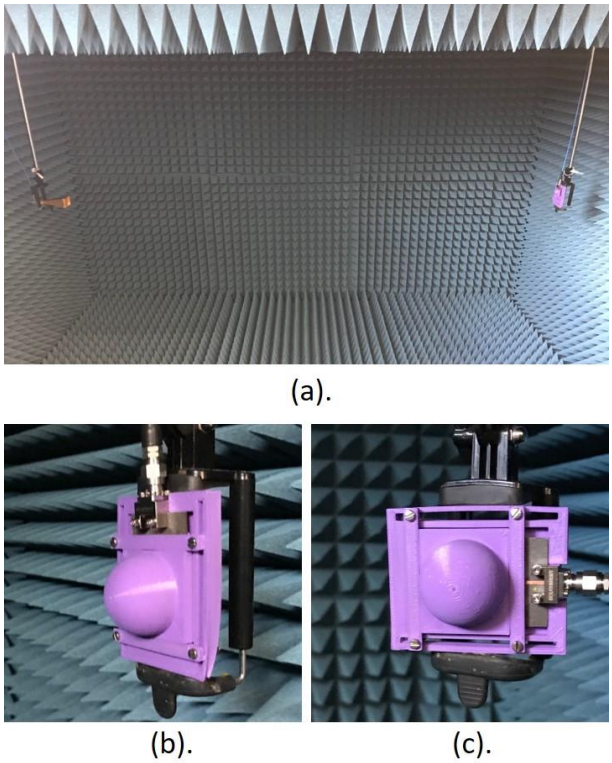

Figure C6: (a). Radiation pattern measurement setup, (b). *E*-plane measurement, (c). *H*-plane measurement

Appendix D

ADS schematic of rectifier circuit in voltage doubler configuration

Figure D1 shows the ADS schematic of proposed rectifier circuit in voltage doubler configuration.

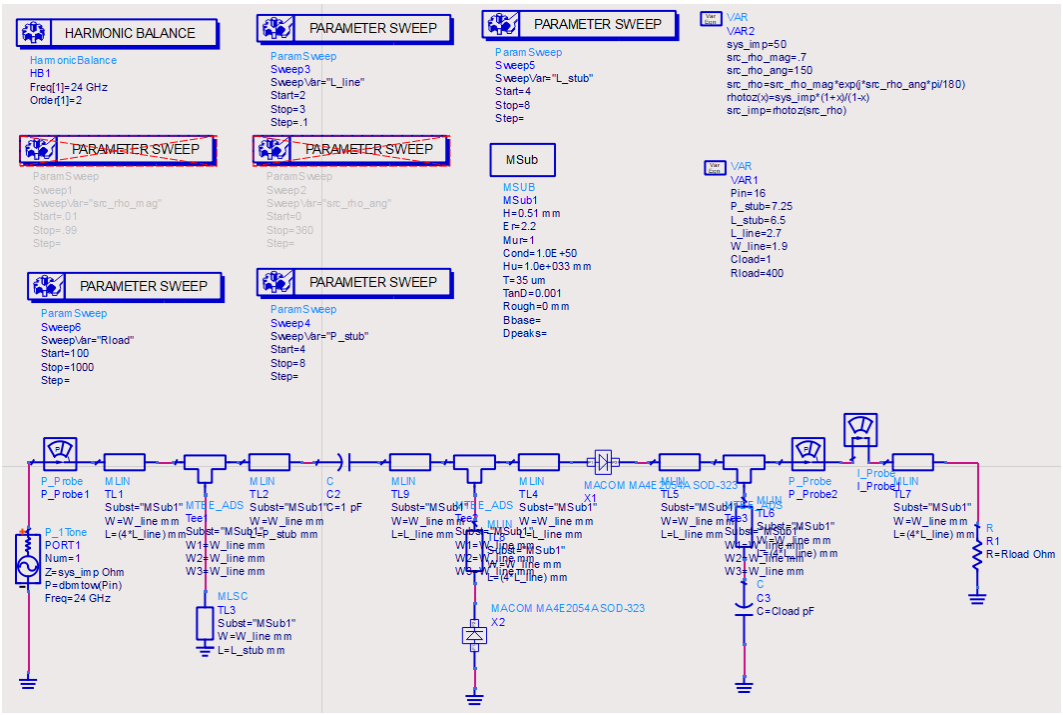

Figure D1: ADS schematic of rectifier circuit in voltage doubler configuration

List of References

1. Yang, Q.-L., et al., *SIW multibeam array for 5G mobile devices.* 2016. **4**: p. 2788-2796.
2. Zhang, J., et al., *5G millimeter-wave antenna array: Design and challenges.* IEEE Wireless Communications, 2016. **24**(2): p. 106-112.
3. Al-samman, A.M., M.H. Azmi, and T.A. Rahman. *A Survey of Millimeter Wave (mm-Wave) Communications for 5G: Channel Measurement Below and Above 6 GHz*. in *International Conference of Reliable Information and Communication Technology*. 2018. Springer.
4. Muirhead, D., M.A. Imran, and K.J.I.A. Arshad, *A survey of the challenges, opportunities and use of multiple antennas in current and future 5G small cell base stations.* 2016. **4**: p. 2952-2964.
5. Mizojiri, S. and K.J.A.S. Shimamura, *Wireless power transfer via Subterahertz-wave.* 2018. **8**(12): p. 2653.
6. Roh, W., et al., *Millimeter-wave beamforming as an enabling technology for 5G cellular communications: Theoretical feasibility and prototype results.* 2014. **52**(2): p. 106-113.
7. Arezoomand, A.S., et al., *Novel techniques in tapered slot antenna for linearity phase center and gain enhancement.* 2016. **16**: p. 270-273.
8. Baranwal, C. *2× 2 microstrip patch antenna array fed by substrate integrated waveguide for radar applications*. in *2017 International Conference on Recent Innovations in Signal processing and Embedded Systems (RISE)*. 2017. IEEE.
9. Erfani, E., et al., *Design and analysis of a millimetre-wave high gain antenna.* 2019.
10. Gonçalves, R., P. Pinho, and N.B. Carvalho. *3D printed lens antenna for wireless power transfer at Ku-band*. in *2017 11th European Conference on Antennas and Propagation (EUCAP)*. 2017. IEEE.
11. Jaschke, T., et al., *Ultrawideband SIW-fed lens antenna.* 2017. **16**: p. 2010-2013.
12. Li, Y., K.-M.J.I.T.o.A. Luk, and Propagation, *Low-cost high-gain and broadband substrate-integrated-waveguide-fed patch antenna array for 60-GHz band.* 2014. **62**(11): p. 5531-5538.
13. Park, J.-S., et al., *A tilted combined beam antenna for 5G communications using a 28-GHz band.* 2016. **15**: p. 1685-1688.
14. Zhang, Y. *Design and Implementation of 28GHz Phased Array Antenna System*. in *2019 IEEE MTT-S International Wireless Symposium (IWS)*. 2019. IEEE.

15. Artemenko, A., et al., *2D electronically beam steerable integrated lens antennas for mmwave applications.* 2012: p. 213--216.

16. Nguyen, N.T., et al., *Size and weight reduction of integrated lens antennas using a cylindrical air cavity.* IEEE Transactions on Antennas and Propagation, 2012. **60**(12): p. 5993--5998.

17. Han, S., et al., *Large-scale antenna systems with hybrid analog and digital beamforming for millimeter wave 5G.* 2015. **53**(1): p. 186-194.

18. Cheng, Y.J., X.Y. Bao, and Y.X. Guo, *LTCC-based substrate integrated image guide and its transition to conductor-backed coplanar waveguide.* IEEE Microwave and Wireless Components Letters, 2013. **23**(9): p. 450-452.

19. Belenguer, A., et al., *Empty SIW Technologies: A Major Step Toward Realizing Low-Cost and Low-Loss Microwave Circuits.* 2019. **20**(3): p. 24-45.

20. Carvalho, N.B., et al., *Wireless power transmission: R&D activities within Europe.* 2014. **62**(4): p. 1031-1045.

21. Saeed, W., et al., *RF energy harvesting for ubiquitous, zero power wireless sensors.* 2018. **2018**.

22. Ejaz, W., et al., *Efficient energy management for the internet of things in smart cities.* 2017. **55**(1): p. 84-91.

23. Park, L., et al., *New Challenges of Wireless Power Transfer and Secured Billing for Internet of Electric Vehicles.* 2018. **57**(3): p. 118-124.

24. Jang, J., et al., *Smart small cell with hybrid beamforming for 5G: Theoretical feasibility and prototype results.* IEEE Wireless Communications, 2016. **23**(6): p. 124-131.

25. A. Ghosh, A.M., M. Baker and D. Chandramouli, *5G Evolution: A View on 5G Cellular Technology Beyond 3GPP Release 15.* Ieee Access, 2019. **7**: p. 127639-127651.

26. Nieto-Chaupis, H. *Modified Friis Equation for Biological Internet*. in *2019 International Workshop on Antenna Technology (iWAT)*. 2019. IEEE.

27. Yadav, P., S. Mukherjee, and A. Biswas. *Design of SIW variable phase shifter for beam steering antenna application*. in *2016 IEEE International Symposium on Antennas and Propagation (APSURSI)*. 2016. IEEE.

28. Lizzi, L., et al. *Design of antennas enabling miniature and energy efficient wireless IoT devices for smart cities*. in *2016 IEEE International Smart Cities Conference (ISC2)*. 2016. IEEE.

29. Zanella, A., et al., *Internet of things for smart cities.* 2014. **1**(1): p. 22-32.

30. https://radiodesign.eu/wp-content/uploads/2019/04/RD_white_paper_smart-cities.pdf.

31. Voigtländer, F., et al. *5G for robotics: Ultra-low latency control of distributed robotic systems*. in *2017 International Symposium on Computer Science and Intelligent Controls (ISCSIC)*. 2017. IEEE.

32. Valenta, C.R. and G.D.J.I.M.M. Durgin, *Harvesting wireless power: Survey of energy-harvester conversion efficiency in far-field, wireless power transfer systems.* 2014. **15**(4): p. 108-120.

33. Fafoutis, X., et al. *On Predicting the Battery Lifetime of IoT Devices: Experiences from the SPHERE Deployments*. in *RealWSN@ SenSys*. 2018.

34. http://www.antenna-theory.com/basics/friis.php.

35. Protection, I.C.o.N.-I.R., *ICNIRP statement on the "guidelines for limiting exposure to time-varying electric, magnetic, and electromagnetic fields (up to 300 ghz)".* Health physics, 2009. **97**(3): p. 257-258.

36. Moradi, M., et al., *Effect of ultra high frequency mobile phone radiation on human health.* Electronic physician, 2016. **8**(5): p. 2452.

37. Bilal T. Malik, V.D., Syed Ali R. Zaidi, Nutapong Somjit, Ian D. Robertson, Charles W. Turner, *Higher-Order Mode Substrate Integrated Waveguide Cavity Excitation for Microstrip Patch Antenna Arrays at 30 GHz.* Journal of Physics Communications, 2019.

38. Malik, B., et al., *Antenna Gain Enhancement by Using Low-Infill 3D-Printed Dielectric Lens Antennas.* IEEE Access, 2019.

39. Malik, B., V. Doychinov, and I. Robertson. *Compact Broadband Electronically Controllable SIW Phase Shifter for 5G Phased Array Antennas*. in *EuCAP*. 2017.

40. Doychinov, V., et al. *Wireless Power Transfer for Gas Pipe Inspection Robots*. in *UK-RAS Conference*. 2017. Bristol, UK: UK-RAS.

41. Moitra, S., A.K. Mukhopadhyay, and A.K. Bhattacharjee, *Ku-band substrate integrated waveguide (SIW) slot array antenna for next generation networks.* Global Journal of Computer Science and Technology, 2013.

42. Yan, L., et al., *Simulation and experiment on SIW slot array antennas.* IEEE Microwave and Wireless Components Letters, 2004. **14**(9): p. 446--448.

43. Yang, Q.L., et al., *SIW Multibeam Array for 5G Mobile Devices.* IEEE Access, 2016. **4**: p. 2788--2796.

44. Abdel-Wahab, W.M. and S. Safavi-Naeini, *Wide-bandwidth 60-GHz aperture-coupled microstrip patch antennas (MPAs) fed by substrate integrated waveguide (SIW).* IEEE Antennas and Wireless Propagation Letters, 2011. **10**: p. 1003-1005.

45. Awida, M.H., S.H. Suleiman, and A.E. Fathy. *Development of a substrate-integrated Ku-band cavity-backed microstrip patch sub-*

array of dual linear/circular polarization for DBS applications. in *Radio and Wireless Symposium (RWS), 2010 IEEE*. 2010. IEEE.

46. Awida, M.H., S.H. Suleiman, and A.E. Fathy, *Substrate-integrated cavity-backed patch arrays: A low-cost approach for bandwidth enhancement.* IEEE Transactions on Antennas and Propagation, 2011. **59**(4): p. 1155-1163.
47. Rossello, J., et al. *Substrate integrated waveguide aperture coupled patch antenna array for 24 GHz wireless backhaul and radar applications*. in *Antenna Measurements & Applications (CAMA), 2014 IEEE Conference on*. 2014. IEEE.
48. Mikulasek, T. and J. Lacik, *Two feeding methods based on substrate integrated waveguide for microstrip patch antennas.* IET microwaves, antennas \& propagation, 2014. **9**(5): p. 423--430.
49. Dong, Y. and T. Itoh, *Metamaterial-based antennas.* Proceedings of the IEEE, 2012. **100**(7): p. 2271-2285.
50. Rani, R., P. Kaur, and N. Verma, *Metamaterials and Their Applications in Patch Antenna: A Review.* International Journal of Hybrid Information Technology, 2015. **8**(11): p. 199-212.
51. Zheludev, N.I. and Y.S. Kivshar, *From metamaterials to metadevices.* Nature materials, 2012. **11**(11): p. 917.
52. Adel, B. and A. Ahmed, *Metamaterial enhances micro strip antenna gain.* Microwaves RF, 2016. **7**: p. 46-50.
53. Azam, S., et al. *Graphene based circular patch terahertz antenna using novel substrate materials*. in *2017 6th International Conference on Informatics, Electronics and Vision & 2017 7th International Symposium in Computational Medical and Health Technology (ICIEV-ISCMHT)*. 2017. IEEE.
54. Jiang, H., et al. *A High Gain 5G Antenna with Near Zero Refractive Index Superstrate*. in *2018 International Conference on Microwave and Millimeter Wave Technology (ICMMT)*. 2018. IEEE.
55. Silveirinha, M.G., et al. *Overview of theory and applications of epsilon-near-zero materials*. in *URSI General Assembly*. 2008. Citeseer.
56. Enoch, S., et al., *A metamaterial for directive emission.* Physical Review Letters, 2002. **89**(21): p. 213902.
57. Naqvi, A.H. and S. Lim, *Microfluidically Polarization-Switchable Metasurfaced Antenna.* IEEE Antennas and Wireless Propagation Letters, 2018. **17**(12): p. 2255-2259.
58. Chana, S. and C. Turner, *Computer aided design of an overmoded cavity-backed helical antenna array.* Electronics Letters, 1993. **29**(15): p. 1378-1380.

59. Asaadi, M. and A. Sebak, *High-gain low-profile circularly polarized slotted SIW cavity antenna for MMW applications.* IEEE Antennas and Wireless Propagation Letters, 2017. **16**: p. 752-755.

60. Han, W., et al., *Single-fed low-profile high-gain circularly polarized slotted cavity antenna using a high-order mode.* IEEE Antennas and Wireless Propagation Letters, 2016. **15**: p. 110-113.

61. Zhang, S., et al., *3D-printed flat lens for microwave applications.* 2015: p. 1--3.

62. Johnson, R.C. and H. Jasik, *Antenna engineering handbook.* New York, McGraw-Hill Book Company, 1984, 1356 p. No individual items are abstracted in this volume., 1984.

63. Mailloux, R.J., *Phased array antenna handbook*. 2005: Artech House. 496.

64. Abdel-Wahab, W.M., D. Busuioc, and S. Safavi-Naeini, *Millimeter-wave high radiation efficiency planar waveguide series-fed dielectric resonator antenna (DRA) array: analysis, design, and measurements.* IEEE Transactions on Antennas and Propagation, 2011. **59**(8): p. 2834-2843.

65. Mehrotra, R., *Cut the cord: wireless power transfer, its applications, and its limits.* cse. wustl. edu, 2014.

66. Massa, A., et al., *Array designs for long-distance wireless power transmission: State-of-the-art and innovative solutions.* Proceedings of the IEEE, 2013. **101**(6): p. 1464-1481.

67. Sihvola, A.H., *Electromagnetic mixing formulas and applications*. 1999: Iet.

68. La Spada, L., R. Tarparelli, and L. Vegni. *Spectral Green's function for SPR meta-structures*. in *Materials Science Forum*. 2014.

69. Padooru, Y.R., et al., *New absorbing boundary conditions and analytical model for multilayered mushroom-type metamaterials: Applications to wideband absorbers.* IEEE Transactions on Antennas and Propagation, 2012. **60**(12): p. 5727-5742.

70. Xu, F., et al., *Finite-difference frequency-domain algorithm for modeling guided-wave properties of substrate integrated waveguide.* IEEE Transactions on Microwave Theory and Techniques, 2003. **51**(11): p. 2221-2227.

71. Kumar, H., et al., *A review on substrate integrated waveguide and its microstrip interconnect.* 2012. **3**(5): p. 36-40.

72. Aftanasar, M. and M. Hafiz. *Fabricated multilayer SIW system using PCB manufacturing process*. in *Applied Electromagnetics (APACE), 2016 IEEE Asia-Pacific Conference on*. 2016. IEEE.

73. Committee, A.S., *IEEE standard test procedures for antennas.* ANSI/IEEE Std, 1979: p. 1949-1979.

74. Komanduri, V.R., et al., *A general method for designing reduced surface wave microstrip antennas.* IEEE Transactions on Antennas and Propagation, 2013. **61**(6): p. 2887-2894.

75. La Spada, L., S. Haq, and Y. Hao, *Modeling and design for electromagnetic surface wave devices.* Radio Science, 2017. **52**(9): p. 1049-1057.

76. Andrews, J.G., et al., *What will 5G be?* IEEE Journal on selected areas in communications, 2014. **32**(6): p. 1065--1082.

77. Rappaport, T.S., et al., *Millimeter wave mobile communications for 5G cellular: It will work!* IEEE access, 2013. **1**: p. 335--349.

78. Muirhead, D., M.A. Imran, and K. Arshad, *A survey of the challenges, opportunities and use of multiple antennas in current and future 5G small cell base stations.* IEEE access, 2016. **4**: p. 2952--2964.

79. Zhang, J., et al., *5G millimeter-wave antenna array: design and challenges.* IEEE Wireless Communications, 2017. **24**(2): p. 106--112.

80. Bayderkhani, R., et al., *Analysis of an integrated lens antenna fed by SIW slot array using a hybrid MoM–PO method.* International Journal of Microwave and Wireless Technologies, 2017. **9**(2): p. 463--468.

81. Jaschke, T., et al., *Ultrawideband SIW-Fed Lens Antenna.* IEEE Antennas and Wireless Propagation Letters, 2017. **16**: p. 2010--2013.

82. Pepino, V.M., et al., *3-D-Printed Dielectric Metasurfaces for Antenna Gain Improvement in the Ka-Band.* 2018. **17**(11): p. 2133-2136.

83. Sauleau, R., C.A. Fernandes, and J.R. Costa, *Review of lens antenna design and technologies for mm-wave shaped-beam applications.* 2005: p. 1--5.

84. Asaadi, M. and A. Sebak, *High gain low profile slotted SIW cavity antenna for 5G applications.* 2016: p. 1227--1228.

85. Konstantinidis, K., et al., *Low-THz dielectric lens antenna with integrated waveguide feed.* 2017. **7**(5): p. 572-581.

86. Wang, K.X., H.J.I.T.o.A. Wong, and Propagation, *Design of a Wideband Circularly Polarized Millimeter-Wave Antenna With an Extended Hemispherical Lens.* 2018. **66**(8): p. 4303-4308.

87. Chudpooti, N., et al., *220-320 GHz Hemispherical Lens Antennas Using Digital Light Processed Photopolymers.* 2019. **7**: p. 12283-12290.

88. Wang, K.X., H.J.I.T.o.A. Wong, and Propagation, *A wideband millimeter-wave circularly polarized antenna with 3-D printed polarizer.* 2017. **65**(3): p. 1038-1046.

89. Ding, C., K.-M.J.I.T.o.A. Luk, and Propagation, *A Wideband High-Gain Circularly-Polarized Antenna Using Artificial Anisotropic Polarizer.* 2019.

90. Artemenko, A., et al., *Millimeter-wave electronically steerable integrated lens antennas for WLAN/WPAN applications.* IEEE Transactions on Antennas and Propagation, 2013. **61**(4): p. 1665--1671.

91. Bisognin, A., et al., *3D printed plastic 60 GHz lens: Enabling innovative millimeter wave antenna solution and system.* 2014: p. 1--4.

92. Gonalves, R., P. Pinho, and N.B. Carvalho, *3D printed lens antenna for wireless power transfer at Ku-band.* 2017: p. 773--775.

93. Elliott, R.S., *An improved design procedure for small arrays of shunt slots.* IEEE Transactions on Antennas and Propagation, 1983. **31**(1): p. 48--53.

94. Xu, J.F., et al., *Design and implementation of low sidelobe substrate integrated waveguide longitudinal slot array antennas.* IET Microwaves, Antennas \& Propagation, 2009. **3**(5): p. 790--797.

95. Volakis, J.L., *Antenna engineering handbook*. 4th ed. 2007: McGraw-Hill. 1818.

96. Yin, H.P. and W.B. Dou, *Analysis of an extended hemi-spherical lens antenna at millimeter wavelengths.* Journal of Electromagnetic Waves and Applications, 2002. **16**(9): p. 1209--1222.

97. *Silicon Radar GmbH. (2019). EvalKits for Radar Front Ends - Silicon Radar GmbH. [online] Available at: https://siliconradar.com/evalkits/ [Accessed 5 Jul. 2019].*

98. Jaschke, T., et al., *K/Ka-band dual-polarized SIW-fed lens antennas for Rx/Tx integration.* 2018. **10**(5-6): p. 627-634.

99. Zhang, Y.-X., et al., *3-D-Printed Comb Mushroom-Like Dielectric Lens for Stable Gain Enhancement of Printed Log-Periodic Dipole Array.* 2018. **17**(11): p. 2099-2103.

100. Farooqui, M.F. and A. Shamim, *A 3D printed helical antenna with integrated lens.* 2015: p. 324--325.

101. Bozzi, M., A. Georgiadis, and K. Wu, *Review of substrate-integrated waveguide circuits and antennas.* IET Microwaves, Antennas & Propagation, 2011. **5**(8): p. 909-920.

102. Kumar, H., R. Jadhav, and S. Ranade, *A review on substrate integrated waveguide and its microstrip interconnect.* Journal of Electronics and Communication Engineering, 2012. **3**(5): p. 36-40.

103. Chen, X.-P. and K. Wu. *Low-loss ultra-wideband transition between conductor-backed coplanar waveguide and substrate integrated waveguide*. in *Microwave Symposium Digest, 2009. MTT'09. IEEE MTT-S International*. 2009. IEEE.

104. Jin, L., R.M. Lee, and I.D. Robertson. *Analysis and design of a slotted waveguide antenna array using hollow substrate integrated*

waveguide. in *Microwave Conference (EuMC), 2015 European*. 2015. IEEE.

105. Jin, L., R.M.A. Lee, and I. Robertson, *Analysis and design of a novel low-loss hollow substrate integrated waveguide.* IEEE Transactions on Microwave Theory and Techniques, 2014. **62**(8): p. 1616-1624.

106. Ali, A., et al. *Analysis and design of a compact SIW-based multi-layer wideband phase shifter for Ku-band applications*. in *2010 IEEE Antennas and Propagation Society International Symposium*. 2010. IEEE.

107. Guntupalli, A.B., et al., *Two-dimensional scanning antenna array driven by integrated waveguide phase shifter.* 2013. **62**(3): p. 1117-1124.

108. Urbanec, T. and J. Lácík. *Compact size substrate integrated waveguide phase shifter*. in *2016 26th International Conference Radioelektronika (RADIOELEKTRONIKA)*. 2016. IEEE.

109. Goswami, L.P., A. Sarkar, and A. Biswas. *Design and implementation of SIW based multiple output X-band phase shifters*. in *2016 Asia-Pacific Microwave Conference (APMC)*. 2016. IEEE.

110. Sellal, K., et al. *A new substrate integrated waveguide phase shifter*. in *2006 European Microwave Conference*. 2006. IEEE.

111. Yadav, P., S. Mukherjee, and A. Biswas. *Design of planar substrate integrated waveguide (SIW) phase shifter using air holes*. in *2015 IEEE Applied Electromagnetics Conference (AEMC)*. 2015. IEEE.

112. Sellal, K., et al., *Design and implementation of a controllable phase shifter using substrate integrated waveguide.* 2012. **6**(9): p. 1090-1094.

113. Muneer, B., et al., *A broadband tunable multilayer substrate integrated waveguide phase shifter.* 2015. **25**(4): p. 220-222.

114. Kramer, O., et al., *Dual-layered substrate-integrated waveguide six-port with wideband double-stub phase shifter.* 2012. **6**(15): p. 1704-1709.

115. Cheng, Y.J., K. Wu, and W. Hong. *Substrate integrated waveguide (SIW) broadband compensating phase shifter*. in *2009 IEEE MTT-S International Microwave Symposium Digest*. 2009. IEEE.

116. Yousef, H., S. Cheng, and H. Kratz, *Substrate integrated waveguides (SIW) in a flexible printed circuit board for millimeter wave applications.* Journal of microelectromechanical systems, 2009. **18**(1): p. 154-162.

117. Díaz-Caballero, E., et al. *Analysis and design of passive microwave components in substrate integrated waveguide technology*. in *Numerical Electromagnetic and Multiphysics Modeling and Optimization (NEMO), 2015 IEEE MTT-S International Conference on*. 2015. IEEE.

118. Bozzi, M., et al. *Additive manufacturing of substrate integrated waveguide components*. in *Advanced Materials and Processes for RF and THz Applications (IMWS-AMP), 2016 IEEE MTT-S International Microwave Workshop Series on*. 2016. IEEE.

119. Parment, F., et al. *Air-filled SIW transmission line and phase shifter for high-performance and low-cost u-band integrated circuits and systems*. in *Millimeter Waves (GSMM), 2015 Global Symposium On*. 2015. IEEE.

120. Parment, F., et al., *Air-filled substrate integrated waveguide for low-loss and high power-handling millimeter-wave substrate integrated circuits.* IEEE Transactions on Microwave Theory and Techniques, 2015. **63**(4): p. 1228-1238.

121. https://www.stratasys.com/-/media/files/printer-spec-sheets/pss_pj_objet1000plus_0917a.pdf.

122. Xu, F. and K. Wu, *Guided-wave and leakage characteristics of substrate integrated waveguide.* IEEE Transactions on microwave theory and techniques, 2005. **53**(1): p. 66-73.

123. Zhu, X.-C., et al., *Accurate characterization of attenuation constants of substrate integrated waveguide using resonator method.* IEEE Microwave and Wireless Components Letters, 2013. **23**(12): p. 677-679.

124. Zhang, Q., et al., *Novel microwave rectifier optimizing method and its application in rectenna designs.* 2018. **6**: p. 53557-53565.

125. Ahmad, W., M.I. Qureshi, and W.T. Khan. *A highly efficient tri band (GSM1800, WiFi2400 and WiFi5000) rectifier for various radio frequency harvesting applications*. in *2017 Progress in Electromagnetics Research Symposium-Fall (PIERS-FALL)*. 2017. IEEE.

126. Matsunaga, T., et al., *5.8-GHz stacked differential rectenna suitable for large-scale rectenna arrays with DC connection.* 2015. **63**(12): p. 5944-5949.

127. Shinohara, N., *Rectennas for microwave power transmission.* IEICE Electronics Express, 2013. **10**(21): p. 1-13.

128. Ladan, S., A.B. Guntupalli, and K. Wu, *A high-efficiency 24 GHz rectenna development towards millimeter-wave energy harvesting and wireless power transmission.* IEEE Transactions on Circuits and Systems I: Regular Papers, 2014. **61**(12): p. 3358-3366.

129. Bito, J., et al. *Millimeter-wave ink-jet printed RF energy harvester for next generation flexible electronics*. in *Wireless Power Transfer Conference (WPTC), 2017 IEEE*. 2017. IEEE.

130. Daskalakis, S., et al. *Inkjet printed 24 GHz rectenna on paper for millimeter wave identification and wireless power transfer applications*. in *Advanced Materials and Processes for RF and THz*

Applications (IMWS-AMP), 2017 IEEE MTT-S International Microwave Workshop Series on. 2017. IEEE.

131. Shinohara, N. and K. Hatano. *Development of 24GHz Rectenna for Receiving and Rectifying Modulated Waves*. in *Journal of Physics: Conference Series*. 2014. IOP Publishing.
132. Collado, A. and A. Georgiadis. *24 GHz substrate integrated waveguide (SIW) rectenna for energy harvesting and wireless power transmission*. in *Microwave Symposium Digest (IMS), 2013 IEEE MTT-S International*. 2013. IEEE.
133. Shinohara, N., et al. *Development of 24 GHz rectennas for fixed wireless access*. in *General Assembly and Scientific Symposium, 2011 XXXth URSI*. 2011. IEEE.
134. Mavaddat, A., S.H.M. Armaki, and A.R. Erfanian, *Millimeter-Wave Energy Harvesting Using $4\times4 $ Microstrip Patch Antenna Array.* IEEE Antennas and wireless propagation letters, 2015. **14**: p. 515-518.
135. Ladan, S., S. Hemour, and K. Wu. *Towards millimeter-wave high-efficiency rectification for wireless energy harvesting*. in *Wireless Symposium (IWS), 2013 IEEE International*. 2013. IEEE.
136. Hamzi, I., et al. *Analysis of Series and Shunt Rectifier Circuits Topologies*. in *2019 International Conference on Wireless Technologies, Embedded and Intelligent Systems (WITS)*. 2019. IEEE.
137. https://www.mouser.com/ds/2/249/MA4E2054_Series-475823.pdf.
138. http://www.skyworksinc.com/Product/509/SMS7621-060.
139. Yang, Z., et al., *Flexible substrate technology for millimeter wave wireless power transmission.* 2016. **3**(1): p. 24-33.
140. Bito, J., et al. *Millimeter-wave ink-jet printed RF energy harvester for next generation flexible electronics*. in *2017 IEEE Wireless Power Transfer Conference (WPTC)*. 2017. IEEE.
141. Daskalakis, S., et al. *Inkjet printed 24 GHz rectenna on paper for millimeter wave identification and wireless power transfer applications*. in *2017 IEEE MTT-S International Microwave Workshop Series on Advanced Materials and Processes for RF and THz Applications (IMWS-AMP)*. 2017. IEEE.
142. Kim, S., et al. *A flexible hybrid printed RF energy harvester utilizing catalyst-based copper printing technologies for far-field RF energy harvesting applications*. in *2015 IEEE MTT-S International Microwave Symposium*. 2015. IEEE.
143. Wagih, M., A.S. Weddell, and S. Beeby, *Millimeter-wave textile antenna for on-body RF energy harvesting in future 5G networks.* 2019.

144. Hafeez, M.T. and S.F. Jilani. *Novel millimeter-wave flexible antenna for RF energy harvesting*. in *2017 IEEE International Symposium on Antennas and Propagation & USNC/URSI National Radio Science Meeting*. 2017. IEEE.

145. Mitani, T., et al., *Analysis of voltage doubler behavior of 2.45-GHz voltage doubler-type rectenna.* 2017. **65**(4): p. 1051-1057.

146. Perdana, M., T. Hariyadi, and Y. Wahyu. *Design of Vivaldi Microstrip Antenna for Ultra-Wideband Radar Applications*. in *IOP Conference Series: Materials Science and Engineering*. 2017. IOP Publishing.